

REPUBLIQUE DU CAMEROUN

Paix-Travail-Patrie



DEPARTMENT OF CIVIL ENGINEERING
DEPARTEMENT DE GENIE CIVIL

REPUBLIC OF CAMEROON

Peace-Work-Fatherland



UNIVERSITÀ
DEGLI STUDI
DI PADOVA

DEPARTMENT OF CIVIL,
ARCHITECTURAL AND
ENVIRONMENTAL ENGINEERING

**FINITE ELEMENT METHOD ANALYSIS OF UNDERGROUND STRUCTURES:
TUNNELLING – SUPERSTRUCTURE INTERACTION.**

CASE OF THE STEINHALDENFELD TRAMWAY TUNNEL IN STUTTGART, GERMANY

*A thesis submitted in partial fulfilment of the requirements for the degree of Master of
Engineering (MEng) in Civil Engineering
Curriculum: Structural Engineering*

Presented by:

FONYUY ETIENNE WIRDZELEE

Student number: **16TP21210**

Supervised by:

Prof. Carmelo MAJORANA

Co-supervised by:

Dr. Eng. Guillaume Hervé POH'SIE

Eng. Giuseppe CARDILLO

Academic year: 2020/2021

DEDICATION

I dedicate this thesis to my loving parents: MR/MRS TATA ERNEST and the entire family.

ACKNOWLEDGEMENTS.

Firstly, I thank the Almighty God for giving me the strength, knowledge and endurance throughout the accomplishment of this work. The achievement of this work would not have been possible without the support and assistance of numerous people, all of whom I would want to express my gratitude to:

- The President of Jury Prof. **NKENG George ELAMBO** for the honour of accepting to preside this jury;
- The Examiner Dr. **BWEMBA Charles** of this jury for accepting to examine this work and bring forth his suggestions and observations to improve this work;
- My supervisors Prof. Eng. **Carmelo MAJORANA**, Dr Eng. **Guillaume POH'SIE** and Eng. **Giuseppe CARDILLO** for their guidance, advices and assistance during the period of this work;
- The Director of the National Advanced School of Public Works Yaoundé Prof. **NKENG George ELAMBO**, for his efforts in running and maintaining this great institution;
- The head of department of civil engineering Prof. **MBESSA Michel**, for the excellent counselling and encouragements;
- All the **teachers** and **staff** of NASPW and the university of Padova for their collaborations, quality teaching and advices given to us throughout our studies;
- All **my classmates** for all their assistance through out these years;
- My **friends** for making my time at NASPW such a delight;
- To my **parents** Mr and Mrs **Tata Ernest** and **my sisters and brothers** for their sacrifices, continuous love and support throughout my entire studies. Without them, this wouldn't have been possible.

LIST OF ABBREVIATIONS AND SYMBOLS

FEM	Finite Element Method
FEA	Finite Element Analysis
FE	Finite Element
NATM	New Austrian Tunnelling Method
RC	Reinforced Concrete
CSSI	Coupled Soil- Structure Interaction
GF	Greenfield
CS or S	Construction Stage
OCR	Over-Consolidation Ratio
HS	Hardening Soil
MC	Mohr Coulomb
D	Tunnel Diameter
φ'	Effective friction angle
c'	effective cohesion
K_o	coefficient of at rest lateral earth pressure
γ	Specific Weight
ν	Poison's ratio
E_{ur}^{ref}	Triaxial unloading stiffness
E_{50}^{ref}	Triaxial loading stiffness
E_{oed}^{ref}	Oedometer loading stiffness
G_o^{ref}	Shear modulus at small strain
m	Stress level dependency of stiffness
$\gamma_{0.7}$	Threshold Shear Strain
S_V	Vertical settlement

S_h	Horizontal surface displacement
V_s	Volume of settlement trough
V_L	Ground or volume loss
V_0	excavated tunnel volume per unit length
VLR	Volume loss ratio
K	trough width parameter
Δ	Relative deflection
DR	Deflection ratio
ε_h	Horizontal surface strain
β	Angular distortion
H	Building height
L	Building width
ϵ_{bmax}	Maximal extreme fibre strain
ϵ_{dmax}	Maximum diagonal strain
ϵ_{lim}	Limiting tensile strain
ϵ_{br}	Resultant extreme fibre strain
ϵ_{dr}	Resultant diagonal tensile strain
ρ^*	Relative bending stiffness
α^*	Relative axial stiffness

ABSTRACT

The main objective of this work was to investigate using finite element analysis the interactive effects of tunneling induced ground movements on an existing superstructure (reinforced concrete building) with a case reference: the conventionally constructed Steinhaldenfeld subway tunnel. The methodology used consisted in simulating the sequential tunnel excavation using a step by step method in MIDAS GTS NX software. The soil behaviour was modelled using the Hardening Soil small strain stiffness constitutive model. The accuracy of the finite element model was validated using available field measurements and numerical solutions. The validated numerical model was used to carry out a 3D fully coupled soil-structure interaction analysis to investigate the tunnelling induced settlements. In addition, the effect of tunnel advancement on the internal forces and the potential damage are studied. It was observed that, as the tunnel progresses towards the structure, the settlement increases rapidly compared to the greenfield case. The presence of the building reduces both the deflection ratio and the maximum settlement induced by tunnelling. From the results, the maximum induced settlement on the building's foundation was 12.45 mm compared to the greenfield maximum settlement of 19 mm. This shows the importance of incorporating soil structure interaction in assessing tunneling induced building damage. It was also found that tunneling induced settlements cause redistribution of internal forces on structural elements. For example, a column with a distance of 4 m from the tunnel axis undergoes a maximum settlement of 12.2 mm which caused its axial force to decrease by 55 KN while a column located at a distance of 8 m from the tunnel axis undergoing a maximum settlement of 11.7 mm, had its axial force increase by 42 KN. The shorter the distance of the column from the tunnel axis, the greater its settlement. In addition, the results of this study showed that with soil structure interaction considered, the building's risk of damage was category level zero (negligible), whereas damage category level of three was obtained when the interaction is not considered. The interpretation of the results gave us a better understanding of the tunneling superstructure interaction and the need to incorporate it when assessing the potential damage induced on a structure.

Keywords: soil structure interaction, finite element analysis, tunnel, settlement, building damage.

RESUME

L'objectif principal de ce travail était d'étudier à l'aide d'une analyse par éléments finis les effets interactifs des mouvements de terrain induits par le creusement d'un tunnel sur une superstructure existante (bâtiment en béton armé) avec un cas de référence : le tunnel de métro Steinhaldenfeld de construction conventionnelle. La méthodologie utilisée a consisté à simuler le creusement séquentiel du tunnel à l'aide d'une méthode pas à pas dans le logiciel MIDAS GTS NX. Le comportement du sol a été modélisé à l'aide du modèle constitutif de rigidité des petites déformations de Hardening Soil. La précision du modèle d'éléments finis a été validée à l'aide des mesures de terrain disponibles et des solutions numériques. Le modèle numérique validé a été utilisé pour effectuer une analyse 3D entièrement couplée de l'interaction sol-structure afin d'étudier les tassements induits par le creusement. En outre, l'effet de l'avancement du tunnel sur les efforts internes et les dommages potentiels sont étudiés. Il a été observé qu'au fur et à mesure que le tunnel progresse vers la structure, le tassement augmente rapidement par rapport au cas du terrain vierge. La présence du bâtiment réduit à la fois le taux de déflection et le tassement maximal induit par le creusement. D'après les résultats, le tassement maximal induit sur la fondation du bâtiment était $12,45 \text{ mm}$ par rapport au tassement maximal du terrain vierge de 19 mm . Cela montre l'importance d'intégrer l'interaction sol-structure dans l'évaluation des dommages aux bâtiments induits par le creusement de tunnels. Il a également été constaté que les tassements induits par le tunnelage entraînent une redistribution des efforts internes sur les éléments structuraux. Par exemple, un poteau avec une distance de 4 m de l'axe du tunnel subit un tassement maximal de $12,2 \text{ mm}$, ce qui a fait diminuer sa force axiale de 55 KN tandis qu'un poteau situé à une distance de 8 m de l'axe du tunnel subissant un tassement maximal de $11,7 \text{ mm}$, a vu sa force axiale augmenter de 42 KN . Plus la distance entre un poteau et l'axe du tunnel diminue, plus son tassement augmente. De plus, les résultats de cette étude ont montré qu'en tenant compte de l'interaction sol-structure, le risque de dommage du bâtiment était de niveau de catégorie zéro (négligeable), alors que le niveau de catégorie de dommage de trois était obtenu lorsque l'interaction n'est pas prise en compte. L'interprétation des résultats nous a permis de mieux comprendre l'interaction tunnel-superstructure et la nécessité de l'intégrer dans l'évaluation des dommages potentiels induits sur un ouvrage.

Mots clés : interaction sol-structure, analyse par éléments finis, tunnel, tassement, dommages aux bâtiments.

LIST OF FIGURES

Figure 1.1. Egg-shaped cross-section of a tunnel.....	4
Figure 1.2. Horse shoe shaped section.....	5
Figure 1.3. D-shaped tunnel cross-section.....	5
Figure 1.4. Excavation sequencing types in conventional tunneling (Lunardi et al., 2019).	7
Figure 1.5. Example of NATM tunnel excavated in 6 partial cross-sections(Masosonore & Boumediene, 2019).....	8
Figure 1.6. Shield tunneling construction phases(Möller, 2006a).....	9
Figure 1.7. Schematic view of EPB TBM and Slurry TBM(Yang Ng, 2021).	11
Figure 1.8. Primary components of ground deformation related to closed shield tunneling(after Mair & Taylor, 1997).	13
Figure 1.9. Components of ground deformation associated with open face tunneling(Möller, 2006).....	14
Figure 1.10. Settlement trough above an advancing tunnel(Attewell et al, 1986).	15
Figure 1.11. The Gaussian curve for transverse settlement trough and volume loss VL	16
Figure 1.12. Distribution of horizontal surface displacement and strain in the transverse direction together with settlement trough(Franza, 2016).	18
Figure 1.13. Longitudinal settlement trough above tunnel centre line(Hajjar et al., 2015)....	19
Figure 1.14. Variation of trough width with depth for tunnels in clay(Mair & Taylor, 1993).	21
Figure 1.15. Simulation phases of the Progressive softening method.....	23
Figure 1.16. Principle of convergence confinement method.(González-Nicieza et al., 2008).	23
Figure 1.17. Gap method for modelling tunnel excavation(Rowe et al., 1983).	24
Figure 1.18. Volume loss control method by ADDENBROKE et al. (1997).....	25
Figure 1.19. Step by step simulation of conventional tunnelling(Möller, 2006).....	26
Figure 1.20. Shield tunnelling using a step-by-step pressure approach.	27

Figure 1.21. Definition of building deformation(J. B. Burland, 1995).	28
Figure 1.22. The equivalent beam approach (J. B. Burland & Wroth, 1974). (a) Actual building. (b) Beam: simple idealisation of building. (c) Deflected shape of soffit of beam. (d) Bending deformation with cracking due to direct tensile strain. (e) Shear deformation with cracking due to diagonal tensile strain.....	32
Figure 1.23. Relationship between $\Delta/(L\epsilon_{lim})$ and L/H for rectangular beams deflecting due to combined bending and shear. Neutral axis in the middle (sagging mode).....	33
Figure 1.24. Relationship between $\Delta/(L\epsilon_{lim})$ and L/H for rectangular isotropic beams (hogging mode)(J. B. Burland & Wroth, 1974).	34
Figure 1.25. Damage interaction diagram for hogging ($L/H=1$), after Burland 1995(Zhang & Zhan, 2021).....	35
Figure 1.26. Relation of damage to angular distortion and horizontal strain(Boscardin & Cording, 1989).....	36
Figure 1.27. Definition of greenfield deflection ratio (Farrell & Mair, 2012).	37
Figure 1.28. Transverse geometry of the interaction problem(Franzius et al., 2006).	38
Figure 1.29. Design curves for modification factors of (a) deflection ratio and (b) maximum horizontal strain(Addenbrooke et al., 1997).	40
Figure 1.30. Schematic diagram of the relative stiffness approach within the three-stage risk assessment(Franzius, 2003).	42
Figure 2.1. (a) 4-node Tetrahedron element, (b) 5-Node Pyramid element, (c) 8-Node Rectangular solid element, (c) 8-Node Hexahedral isoparametric element.	45
Figure 2.2. Stress-strain relationship for linear elastic-perfectly plastic behaviour.	48
Figure 2.3. Linear elastic stress-strain relationship.	50
Figure 2.4. Third excavation stage plus shotcrete and rock bolt installation in the preceding excavation.....	52
Figure 3.1. Satellite map showing the location and the course route (red line) of the Steinhaldenfeld tunnel.	58
Figure 3.2. Site plan of the Steinhaldenfeld Tunnel(Möller, 2006).....	59
Figure 3.3. Geological longitudinal profile of Steinhaldenfeld tunnel(Moayed et al., 2011). 59	

Figure 3.4. Top heading drive with subsequent bench and base support.....	61
Figure 3.5. Construction of the Steinhaldenfeld Tunnel(Möller et al., 2004).....	61
Figure 3.6. Numerical model of greenfield situation: (a.) Front view (b.) 3D view.....	63
Figure 3.7. Model of a shotcrete lining segment and rock bolts of the top heading section ..	63
Figure 3.8. Sequential construction stages plus shotcrete and rock bolts installation in the preceding phase: (a.) Construction stage 20 (b.) Construction stage 56.....	64
Figure 3.9. Comparison between the transverse settlement trough of normally consolidated ground (OCR=1) in this study with field measurements and other numerical studies.....	65
Figure 3.10. Comparison between the transverse settlement profile of an over consolidated ground in this study with field measurements.....	65
Figure 3.11. Structural plan of first floor to fifth floor.....	67
Figure 3.12. Structural plan of sixth floor to the roof.....	67
Figure 3.13. Front elevation of building.....	68
Figure 3.14. Finite element model of 3D structure.....	68
Figure 3.15. Front view of the fully coupled soil structure numerical model.	69
Figure 3.16. FE model of 3D fully coupled structure interaction.....	70
Figure 3.17. Position of the building in top of the tunnel.....	70
Figure 3.18. Simulation of tunnel excavation sequence at construction stage 32.	71
Figure 3.19. Transverse settlement profile at Y=90 m from tunnel opening.	72
Figure 3.20. Longitudinal tunneling induced settlement profiles at different positions of tunnel face.....	73
Figure 3.21. Vertical displacement contours at construction stage 60 (Y=72 m).	74
Figure 3.22. Maximum compressive and tensile surface horizontal strains.....	74
Figure 3.23. Surface horizontal strain contours at last excavation stage (transverse section at Y = 90 m).	75
Figure 3.24. 3D view of vertical displacement contours of the global model at construction stage 50.....	76

Figure 3.25. Plan view: vertical displacement of the global model.....	76
Figure 3.26. Comparison between longitudinal settlement profiles of the greenfield and coupled structure interaction situations with regard to the tunnel advancement.....	77
Figure 3.27. Comparison between transverse settlement profiles of the greenfield and coupled structure interaction situations ($Y = 32\text{ m}$) with regards to the tunnel advancement.....	78
Figure 3.28. Tunnel-induced foundation settlement.....	79
Figure 3.29. Foundation settlement contours with tunnel heading at $Y = 79.2\text{ m}$	80
Figure 3.30. Induced Transverse horizontal strains on the foundation.....	80
Figure 3.31. horizontal strain contours in the X direction at the end of the excavation sequence.	81
Figure 3.32. Vertical displacements of the tunnel crown.	82
Figure 3.33. Deformations of shotcrete segments after 70 excavations steps.	82
Figure 3.34. Major principal strains on the shotcrete segments at the end of excavation.	83
Figure 3.35. Axial forces on rock bolts at the end of excavation.	84
Figure 3.36. Vertical displacement of the structure under normal conditions.....	85
Figure 3.37. Axial forces on structure under normal conditions.	85
Figure 3.38. location of the examined structural elements on the base floor.	86
Figure 3.39. Variation of the vertical displacement of columns (C1, C2, C3) with tunnel advancement.	87
Figure 3.40. Variation of the vertical displacement of columns (C4, C5) with tunnel advancement.	87
Figure 3.41. Variation of axial force of column 1.	88
Figure 3.42. Variation of axial force of column 2.	88
Figure 3.43. Variation of axial force of column 3.	89
Figure 3.44. Variation of axial force of column 4.	89
Figure 3.45. Variation of axial force of column 5.	89
Figure 3.46. Axial forces in members at the end of construction.....	90

Figure 3.47. Variation of the bending moment of beam B1 as the tunnel advances	91
Figure 3.48. Variation of the bending moment of beam B2 as tunnel advances.....	91
Figure 3.49. Variation of the bending moment of beam B3 as tunnel advances.....	92
Figure 3.50. Building damage interaction diagram for sagging ($L/H=1.53$).....	93
Figure 3.51. Determination of the deflection ratio of the structure.....	94
Figure 3.52. Evaluation of the damage along the foundation of the building.....	94
Figure 3.53. Determination of the greenfield deflection ratios.	95
Figure 3.54. Greenfield damage interaction diagram for sagging ($L/H=0.75$).....	96
Figure 3.55. Greenfield damage interaction diagram for hogging ($L/H=0.49$).	96
Figure 3.56. Evaluation of building damage in the sagging zone.	97
Figure 3.57. Evaluation of building damage in the hogging zone.....	97

LIST OF TABLES

Table 1.1. Classification of visible damage to walls with particular reference to ease of repair of plaster and brickwork or masonry after Burland (1995)(Franzius, 2003).....	30
Table 1.2. Relation between category of damage and limiting tensile strain(Boscardin & Cording, 1989; J. B. Burland, 1995).	31
Table 2.1. Summary of parameters for the Hardening Soil (soil strain stiffness) model.	49
Table 2.2. Element types used for mesh generation of the model.	50
Table 3.1. Steinhaldenfeld ground parameters of the MC-Model from site investigation(Möller et al., 2004).....	60
Table 3.2. Additional Parameters for the Hardening Soil (Small strains stiffness) Model(Möller, 2006a).	60
Table 3.3. Properties of shotcrete lining and rock bolts (Moayed et al., 2011; Möller, 2006b).	62
Table 3.4. Mechanical properties of the reinforced concrete.....	66
Table 3.5. Geometrical properties of the reinforced concrete elements.	66
Table 3.6. Characteristic value of loads acting on building.....	69
Table 3.7. Deformation parameters of the greenfield section.....	96
Table A.0.1. Imposed loads on floors, balconies and stairs in buildings.....	106

TABLE OF CONTENTS

DEDICATION	i
ACKNOWLEDGEMENTS	ii
LIST OF ABBREVIATIONS AND SYMBOLS	iii
ABSTRACT	v
RESUME	vi
LIST OF FIGURES	vii
LIST OF TABLES	xii
TABLE OF CONTENTS	xiii
GENERAL INTRODUCTION.	1
CHAPTER 1. LITERATURE REVIEW.....	3
Introduction	3
1.1. Tunnel.....	3
1.1.1. Tunnel Linings.....	3
1.1.2. Shape of Tunnels	3
1.2. Common tunnel excavation methods.	5
1.2.1. Underground construction methods.....	6
1.2.2. Cut and cover construction method.	12
1.3. Ground response to tunneling.....	12
1.3.1. Components of ground deformation.....	12
1.3.2. Prediction of tunneling induced ground movements.....	14
1.4. Building damage induced by ground movements.	28
1.4.1. Definitions of building damage parameters.....	28
1.4.2. Damage assessment criteria.....	29
1.4.3. Building strains assessment to evaluate building damage.....	31

1.4.4. Soil structure interaction.....	36
1.4.5. Methodology for assessing the risk of damage.	41
Conclusion	43
CHAPTER 2. METHODOLOGY.....	44
Introduction.	44
2.1. Site recognition.....	44
2.2. Data collection.....	44
2.3. The Finite Element Method.....	44
2.3.1. Element discretization (Meshing).....	44
2.3.2. Primary Variable Approximation.	45
2.3.3. Element equations formulation.....	46
2.3.4. Global Equations Formulation and boundary conditions.	46
2.3.5. Solution of global equations.	46
2.4. Finite Element Simulation of Tunnel Construction in Greenfield Conditions.....	47
2.4.1. Three-Dimensional Finite Element Model.	47
2.4.2. Tunnel Installation Simulation Method.	51
2.4.3. Validation of the 3D Finite Element Model.	52
2.5. Simulation of Coupled Soil Structure Interaction.	53
2.5.1. Loads	53
2.5.2. Load Combination	53
2.5.3. Numerical Modelling of Superstructure.....	54
2.5.4. Coupled Soil Structure Model.	54
2.6. Building Damage Evaluation.....	55
2.6.1. Choice of Appropriate Damage Criteria.....	55
2.6.2. Damage Interaction Diagram.....	55
Conclusion.....	56

CHAPTER 3. RESULTS INTERPRETATION AND DISCUSSIONS	57
Introduction	57
3.1. Site Description	57
3.1.1. Location	57
3.1.2. Geological Condition.....	59
3.2. Data Presentation.....	59
3.2.1. Geotechnical Characterisation.....	59
3.2.2. Geometrical Information	61
3.2.3. Tunnel Support Details.....	62
3.3. FE Model of The Greenfield Situation.....	62
3.3.1. Tunnel Construction Stages.....	64
3.3.2. Finite Element Model Validation	64
3.4. Numerical Model of The Coupled Soil Structure Interaction	66
3.4.1. Numerical Model of Superstructure	66
3.4.2. Fully Coupled Soil Structure Model.....	69
3.4.3. Tunnel Construction Stages.....	71
3.5. Finite Element Analysis Results.....	72
3.5.1. Greenfield Analysis.....	72
3.5.2. Coupled Soil Structure Interaction Analysis.	75
3.6. Structural Response	84
3.6.1. Response of The Structure Under Ordinary Conditions.....	84
3.6.2. Structural Response of The Structure Due to Tunnelling.....	86
3.7. Evaluation of Building Damage Category	93
3.7.1. Building damage with soil structure interaction considered	93
3.7.2. Building damage with soil structure interaction not considered (greenfield case).95	
Conclusion.....	98

GENERAL CONCLUSION AND RECOMMENDATIONS	99
REFERENCES	101
APPENDIX	106
APPENDIX A: Characteristic values of imposed loads(EN1991-1-1, 2002)	106
APPENDIX B: SOIL CONSTITUTIVE MODEL.....	107
APPENDIX B.1: The Hardening Soil Model.....	107
APPENDIX B.2: The HS-Small Model.	111
APPENDIX C: Construction Stages for Greenfield Analysis.....	115
APPENDIX D: Construction Stages for Fully Coupled Soil Structure Interaction Analysis.	117

GENERAL INTRODUCTION.

Rapid urban growth has led to the increased need of infrastructure. Due to the limited amount of space in urban cities, underground structures such as tunnels become more effective in providing the necessary infrastructure. Most of these tunnels are constructed at shallow depths. The construction of tunnels in soft ground often results in surface ground movements, which in urban areas affects existing surface structures in terms of displacements, drifts and excess internal forces leading to structural damage. Therefore, it is essential for both engineering design, planning and consultation to estimate the possible damage on existing superstructures. Existing design techniques are conservative and result in unnecessary expenditure in the design and provision of protective measures. A better knowledge of the mechanics that govern the tunneling-induced deformations could help reduce expenditure. Engineering design of deep excavations is acceptable only if the ground movements and risk of damage are within levels of engineering safety.

In recent years, evaluation of tunneling induced ground deformations has been carried out using empirical methods, analytical solutions and numerical methods. Although empirical and analytical approaches are often straightforward and useful techniques, the potential of their application are limited. In order to obtain an accurate assessment of ground deformations, the computational method should be able to consider a number of variables such as: the construction method and parameters, the tunnel's depth and diameter, the initial stress condition, and the stress strain behaviour of the soil surrounding the tunnel. This can be achieved using the Finite Element Method. 2D and 3D numerical approaches both exist. In many circumstances, a detailed investigation of the soil-tunnel-structure interaction can only be obtained using three-dimensional modelling, which considers simultaneously the effects of tunnelling and existing structures and also accounts for the three-dimensional nature of tunnel excavation. With this accurate assessment of tunnel induced ground deformations and thus associated building damage, the design and planning process can be optimised.

This thesis utilizes a three-dimensional finite element analysis using MIDAS GTS NX software to investigate the interaction between a reinforced concrete building and the sequentially constructed Steinhaldenfeld tunnel subway. Settlement profiles of the ground as the tunnel advances is developed. Besides, the effect of sequential tunnel excavation on the structural elements is investigated and the potential level of damage of the building determined. In order to achieve this, the thesis is divided into the following three chapters:

Chapter 1: A literature review is given which presents the common computational methods used in evaluating tunnel induced settlements. Firstly, an overview of the most common tunnel excavation techniques is presented, then a review of empirical and numerical methods used in predicting tunnel induced ground movements is presented. Finally, building damage induced by tunnelling is studied.

Chapter 2: This chapter deals with the finite element modelling of the tunnel. It starts by giving an overview of the finite element method. The methodology adopted in creating the finite element model to simulate the tunnel construction process in both greenfield conditions and coupled interaction case is presented. The building damage evaluation procedure is also discussed.

Chapter 3: In this chapter, the results obtained from the methodology carried out are presented, interpreted and discussed.

Afterwards, the general conclusion and suggestions are provided.

CHAPTER 1. LITERATURE REVIEW.

Introduction

This chapter is ordered into three parts. The first part presents review of the most common tunnel excavation techniques. The response of the ground to tunnelling is presented in the second part, besides which the empirical and numerical methods used to predict these tunnelling induced ground movements are also illustrated. Finally, the study of building damage induced by ground movements is presented, under which the soil structure interaction problem and the methodology used in assessing potential building are discussed.

1.1. Underground tunnel

A tunnel is defined as an underground or underwater passageway, dug through the surrounding soil/rock. A tunnel maybe for vehicular road traffic, for rail traffic, foot or for a canal. Allow the road or railway to pass under, for example buildings, highlands or water.

1.1.1. Tunnel linings

These are the temporary or permanent support that keeps the tunnel from collapsing during the excavation process and operational phase of the tunnel respectively.

1.1.1.1. Temporary support or primary lining

It can be defined as any system installed to support the perimeter of an underground opening from the time it is first excavated up to the time that a permanent lining is in place. Typical temporary supports are shotcrete (pneumatically applied mortar and concrete), rock bolts and/or steel ribs.

1.1.1.2. Permanent support or secondary lining

It can be defined as a support that is designed and installed to ensure the long-term stability of the underground structure. Furthermore, the support also minimises tunnel turbulence and insulates the tunnel from moisture infiltration and humidity. Cast in-situ concrete lining, precast concrete segments, cast iron, coated steel segments, shotcrete, and steel ribs are examples of common permanent supports.

1.1.2. Shape of tunnels

There exist different shapes of tunnel cross-sections. The shape of tunnel used depends on the nature of soil, pressure of ground and the purpose of the tunnel.

1.1.2.1. Circular section

This type of section offers greater resistance to external pressure caused by water, water bearing soils or soft grounds. It is essential to use circular section for highly unstable ground, such as soft clay or sand. Circular tunnels are mostly suitable sewers and water conveying, and are not preferred for traffic tunnels as filling would be required for flat base.

1.1.2.2. Egg-shaped section

They are best suited for carrying sewage. In egg shaped tunnels, self-cleansing velocity of flow of sewage maintains in dry and rainy seasons(Pattekar, 2020). They can resist external as well as internal pressure due to their circular walls. Figure 1.1 shows an egg-shaped tunnel section

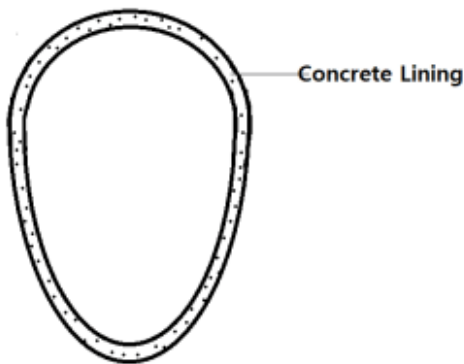


Figure 1.1. Egg-shaped cross-section of a tunnel.

1.1.2.3. Horse shoe section

This form has semi-circular roof with arches sides and curved invert. Horse shoe section tunnels commonly used for highway and railways, also suitable for carrying water and sewage. These tunnels suitable in soft rock. When lined, section gives good resistance to external pressure. Figure 1.2 shows the transverse section of a horse shoe shaped tunnel.

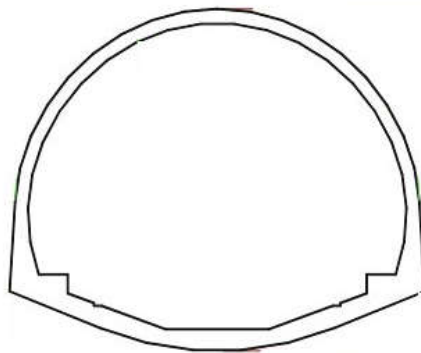


Figure 1.2. Horse shoe shaped section.

1.1.2.4. Rectangular section

It is in the form of a reinforced concrete box. They are generally adopted for pedestrian traffic. Rectangular sections are costly and difficult to construct. These types of tunnels are not suitable to resist external pressure due to their rectangular shape and therefore are most suitable for hard rocks.

1.1.2.5. Segmental or D-shaped section

It is section with an arched roof with straight sides. The external load is transferred from the arched roof onto the vertical side walls. The D-shaped are generally used for subway or navigation tunnels. A representation of a D-shaped section is illustrated in Figure 1.3.

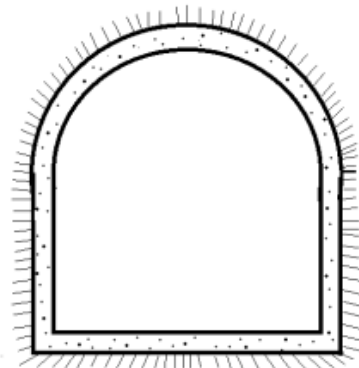


Figure 1.3. D-shaped tunnel cross-section

1.2. Common tunnel excavation methods

Tunnel construction techniques in soft ground have advanced significantly in recent years. The choice of which technique to employ is influenced by various factors such as:

- the site's geologic conditions;

- the tunnel's geometry, diameter, and length;
- the ground movement tolerance of adjacent structures;
- the cost of tunneling and tunnel worker safety.

In this section, there will be a distinction between underground construction methods and the cut and cover construction method.

1.2.1. Underground construction methods

These are trenchless tunneling methods without removing the overburden ground. Some of these can be addressed in terms of open face and closed face tunneling.

1.2.1.1. Open face tunneling

Open face tunneling involves tunneling methods that do not apply permanent support to the excavated tunnel heading i.e. all cases where the tunnel face is easily accessible(Möller, 2006a). This makes it easier to treat weak and unstable ground from within tunnels to control ground movements (with the use of anchors or rock bolts). The methods of open face tunneling will be briefly discussed in the following sections.

a. Conventional tunneling method

The conventional tunneling method is also known as the NATM (New Austrian Tunneling Method) or the sprayed concrete method. This method is used for large non-circular tunnels in poor ground where rapid ground support is required. Initial ground support is often provided by a combination of shotcrete, steel sets, or lattice girders and the installation of rock bolts, which are installed immediately after each excavation sequence. The use of flexible supporting measures to improve the stability of softer grounds reduces ground deformations which is important in preventing tunnel-induced deformations from affecting neighboring structures.

The flexibility of this method means different excavation means can be employed depending on the quality of the ground. In softer ground, specialized tunnel excavators can be used to remove the material, while in jointed rock, road header machines can be used, and for weak to strong rock, the drill and blast method can be utilized(Möller, 2006a). The construction of large tunnel sections is made easier by subdividing the tunnel into multiple arched smaller sections for easier control and safer support during excavation, with the newly formed surfaces

supported temporally often by using shotcrete and bolts. Horizontal and vertical face subdivision are the two most common face subdivision schemes as shown in figure 1.4 below.

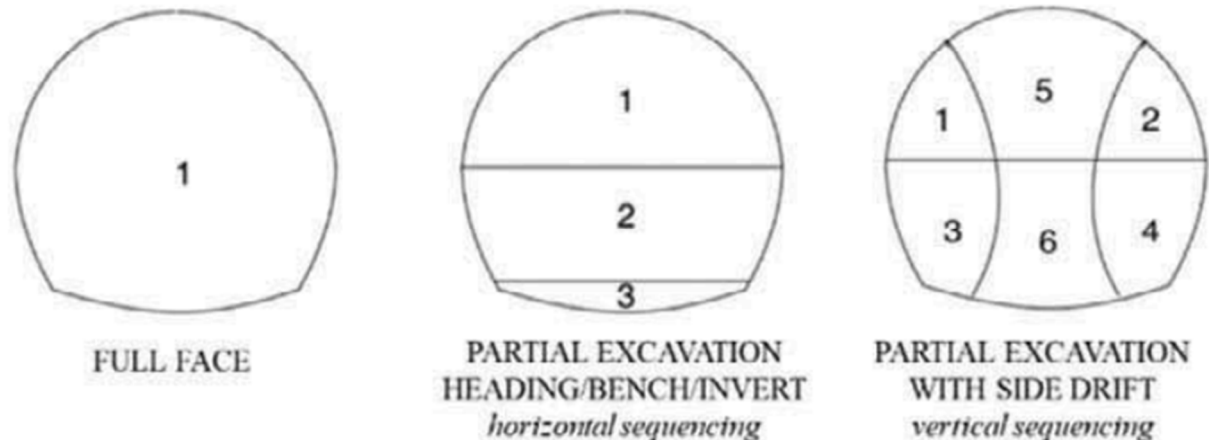


Figure 1.4. Excavation sequencing types in conventional tunneling (Lunardi et al., 2019).

The distance of a heading that is excavated in a single construction stage is called the round length or advance length. Surface settlements are greatly reduced when the round length is reduced. The round length is usually between 0.5m and 1.5m(KOLYMBAS, 1998, as cited in Möller, 2006).

The initial shotcrete lining must provide the support required for a significant period before the final lining is installed. The final lining usually consists of reinforced cast-in-place concrete which assures the structure's stability throughout its life. To protect the final lining from an outer aggressive environment, a waterproofing membrane is placed between the cast-in-place concrete and the initial ground support. An example of NATM tunnel excavated in 6 partial cross-sections is illustrated in Figure 1.5.

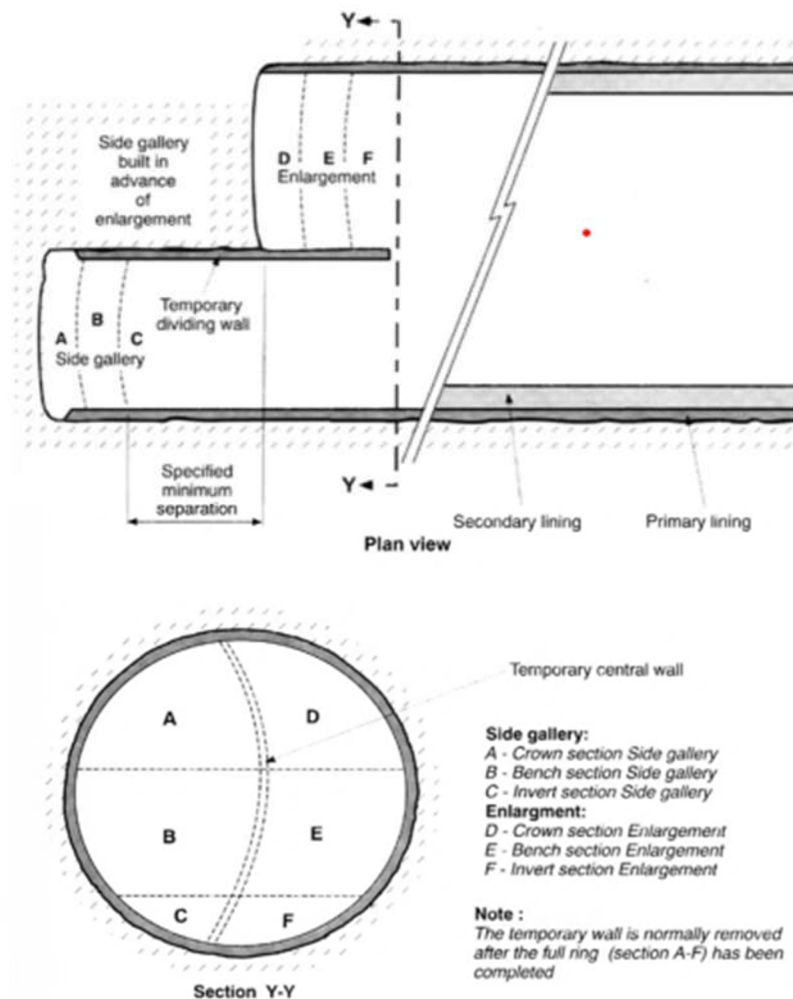


Figure 1.5. Example of NATM tunnel excavated in 6 partial cross-sections(Masosonore & Boumediene, 2019).

b. Open face shield tunneling

Marc Brunel in the early 19th century invented the concept of shield tunneling when he constructed a tunnel under the Thames in London (1825). Brunel's shield was 22 feet tall and 38 feet broad, allowing 36 miners to work the face at once(Eberhardt, 2014) and the tunnel was built with masonry right behind the shield. James Greathead 1869 later built a tunnel under the Thames using a circular shield and Cast iron segments made up the tunnel lining(Eberhardt, 2014; Möller, 2006a). The circular shield later became the model for later open face shields because of its statically favourable shape compared with the rectangular shield.

The shield is generally made of steel and is cylindrical, designed to support all construction and ground loads. The inner shield diameter is bigger than the lining's outer diameter, allowing tubbings (precast concrete lining segments) to be installed. The shield is

pushed away from the installed lining into the soil by jacks fitted in the shield. The jacks are released after each successive advance length (0.8 m-2.0 m), allowing for the construction of a new tubing ring. Tubings are inserted inside the shield's tail to prevent the ground from deforming or falling into the tunnel that has been excavated. (Möller, 2006a). In case the tunnel face is unstable, steel plates connected to hydraulic jacks can be used which applies a certain face pressure. When tunnelling under the groundwater table, open face tunneling becomes an issue. To overcome such conditions, closed face tunneling techniques become more efficient. Figure 1.6 some construction phases of shield tunnelling.

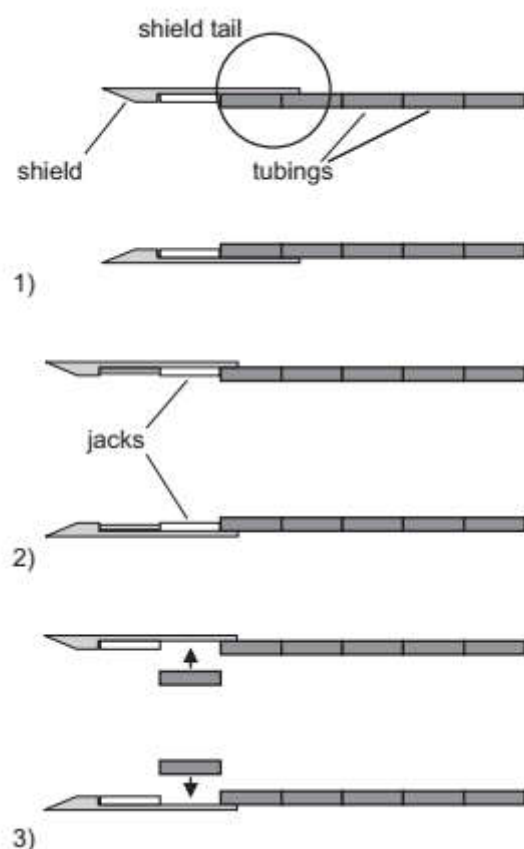


Figure 1.6. Shield tunneling construction phases(Möller, 2006a).

1.2.1.2. Closed face tunneling

In close face tunneling, face support is continuously applied to the tunnel face. Advances in technology have led to the development of tunnel boring machines (TBM) which provide face support by applying a confining counter-pressure. These machines are employed in unstable ground conditions where the face requires constant support. The high reduction of ground deformation means this method is highly suitable for shallow urban tunneling where controlling settlements is of high priority. In mechanized tunneling, face support can be

provided in different ways depending on the geotechnical conditions. The most commonly used tunnel boring machines are;

a. Mechanical TBM

The face support is provided by the cutting wheels themselves, while steel plates can also be provided between the free areas of the cutting arms to slide over the tunnel face while the boring machine is spinning. This method is only suitable for predominantly stable cohesive grounds above the groundwater table, despite the continuous pressure applied on the face(Möller, 2006a).

b. Compressed air TBM

The concept of pressurized air was first developed during the construction of the London Underground in 1886, where James Greathead combined shield tunneling with the use of compressed air to overcome the difficulty of confining groundwater during the construction of subaqueous tunnels in loose soil(Eberhardt, 2014). The compressed air TBM is a boring machine that uses compressed air to counteract the hydrostatic pressure exerted against the cutting head. These machines are mainly suited for tunneling in unstable soils under the water table with a medium to low permeability. The higher permeability of soils can be decreased by injecting bentonite slurry onto the excavation face.

c. Slurry shield TBM

The tunnel face is supported by bentonite slurry which is mixed and pumped into a closed excavation chamber. The slurry then enters the ground forming a filter cake (impermeable mud layer) that seals the tunnel face allowing the creation of a particular face pressure that balances the earth and water pressures. The excavated ground is mixed with slurry in the excavation chamber (Larger stones must be broken first in a specific stone crusher before entering the slurry chamber) and the suspension is pumped to a separation plant on the surface where the bentonite slurry is separated from the ground(soil). As needed, more bentonite is added, and the fluid is pumped back to the excavation chamber. Slurry shields were traditionally used for coarse-grained soils and larger diameters mainly because fine soils are more difficult to separate in surface plants for bentonite recovery(Conditioning et al., 2022).

d. Earth Pressure Balance (EPB) TBM

In the EPB method, the ground excavated by the cutter head is mixed and collected under pressure in an excavation chamber to counteract the ground's pressure, ensuring face

stability while the shield proceeds as shown in Figure 1.7. The muck is subsequently extracted at atmospheric pressure using the screw conveyor. The screw conveyor maintains the pressure at the tunnel face as the TBM advances by having its extraction speed controlled. Earth pressure balance machines (EPB) are mostly utilized in soft, clayey, and silty soils with lower diameters mainly because fine soils are better at creating a plastic mass for pressure transmission (Conditioning et al., 2022). To extend the application of EPB towards coarser soils, the injection of additives such as foam, polymers, and bentonite slurry during the excavation can be used to ensure appropriate properties of the excavated soil and facilitate pressure control in the chamber.

Schematic views of an earth pressure balance machine and a slurry shield machine are illustrated in Figure 1.7 below.

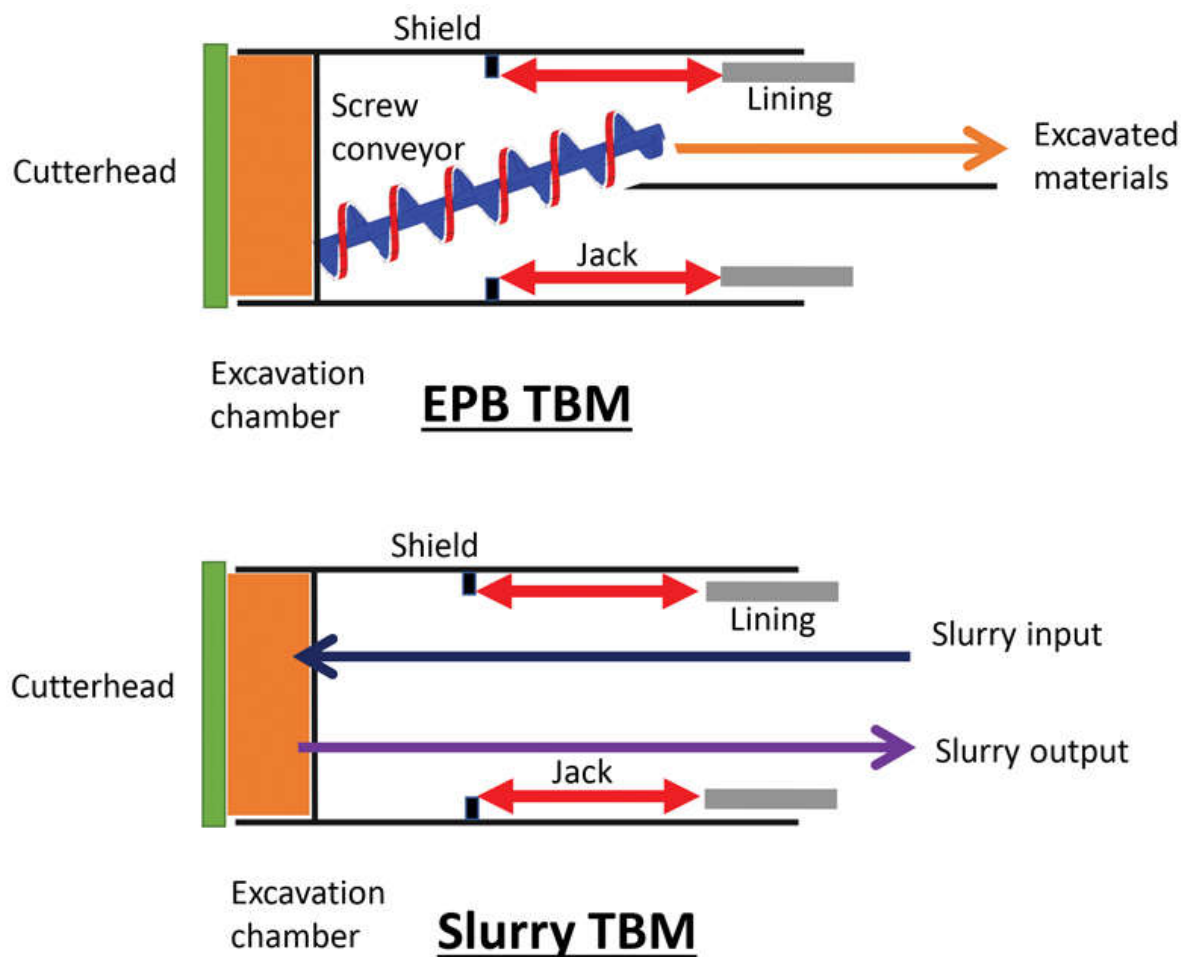


Figure 1.7. Schematic view of EPB TBM and Slurry TBM(Yang Ng, 2021).

1.2.2. Cut and cover construction method

This method is the oldest method of tunneling. Cut and cover tunnels are defined as "a tunnel constructed by excavating a trench from the surface, constructing the structure within the trench, and then backfilling to restore the surface," according to the International Tunneling and Underground Space Association. This technique is used for the construction of shallow depth tunnels such as large sewer tunnels, vehicular tunnels(highway tunnels), and rapid transit tunnels(Mouratidis, 2008; Wilton, 1996).

The basic concept consists of excavating a trench that is roofed over, building a tunnel, and then restoring the surface to its original state. In the cut and cover method, the structure is constructed inside an excavation and then covered with backfill material once it is complete. The excavation walls are supported by sheet piles or Berliner walls. The final lining is made of precast concrete segments or cast-in-place concrete.

1.3. Ground response to tunnelling

The construction of tunnels or surface excavations brings about significant ground movements. The main causes of ground movements associated with excavation are related to stress changes (reduction in vertical and horizontal stresses) which lead to the release of elastic strain, and in the case of weak materials, plastic deformation(Bell et al., 1988). Because of the influence of ground movements on existing buildings, tunnels, and services, these may be of particular significance in the urban environment. Ground movement prediction and assessment of potential effects on existing structures is a crucial factor in construction works involving tunneling or excavations. In this section, we look at the main components of ground deformation(movement) due to closed face shield tunneling as well as open-face conventional tunneling and the methods of prediction of these ground movements.

1.3.1. Components of ground deformation

The following primary components of ground deformation related to closed shield tunneling as illustrated in Figure 1.8 were outlined by Mair & Taylor, (1997):

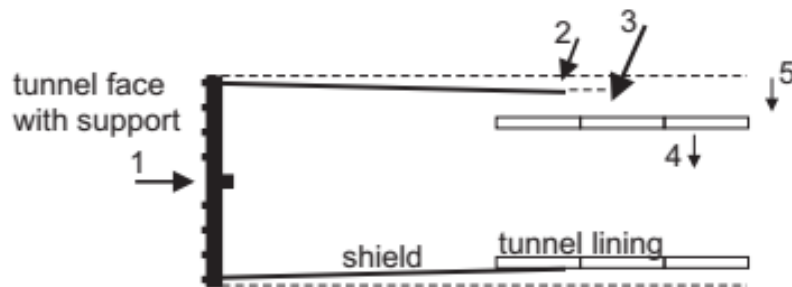


Figure 1.8. Primary components of ground deformation related to closed shield tunneling(after Mair & Taylor, 1997).

1. Ground deformation towards the face as a result of stress reduction.
2. Shield passage: radial ground movements are caused by the presence of an over-cutting edge coupled with any tendency of the machine to plough.
3. Tail void: Radial ground movement into the gap between shield and lining.
4. Deformation of the lining as ground loading increases.
5. Consolidation: changes in effective stress as pore water pressures in the ground adjust to their equilibrium values lead to radial movements.

When sufficient face support is available, for example with a slurry shield or EPB tunneling machine, the first component can be almost negligible. The second component can be effective, especially if the over-cutting edge (intended to produce a slightly larger diameter than that of the shield and thus reduce skin friction) is thick and there are steering issues in keeping the shield aligned. The third component of ground movement is usually the main cause of settlement and can be minimized by immediate grouting of the tail void. Component four tends to be very small compared to other components once the lining is completed. Component five can be of importance particularly in soft clays due to their low permeabilities.

For open face tunneling (Figure 1.9), the main causes of the settlement are specified by Möller (2006) as follows:

- A Ground movement in the direction of the unsupported tunnel.
- B Deformation of the lining as ground loading increases.
- C Consolidation: causes radial ground movement towards the lining.

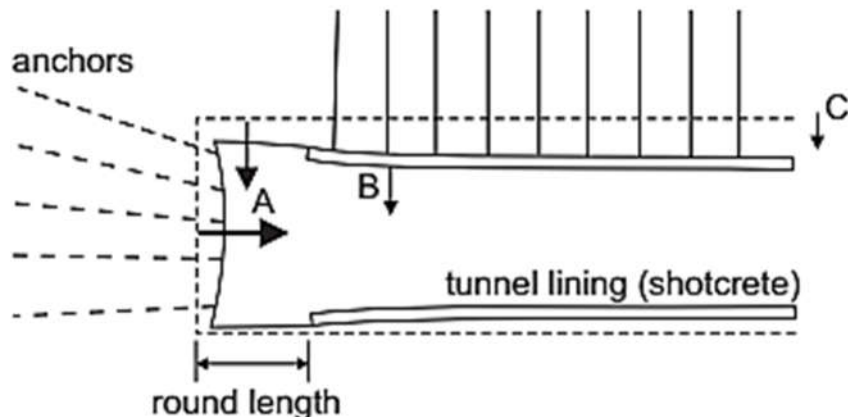


Figure 1.9. Components of ground deformation associated with open face tunneling(Möller, 2006)

Ground movement (A) can be reduced by using face anchors or by the reduction of round length. Due to the use of an initially ductile shotcrete lining as temporary support, the deflection (B) of the lining is significant. The concrete hardening process is accelerated by the use of various additives. On grounds with low permeability, consolidation (C) may take place after tunnel construction whereas, on grounds with high permeabilities, the dissipation/consolidation of pore water pressure occurs often in front of the tunnel face, and earth movements can occur rapidly during construction.

1.3.2. Prediction of tunneling induced ground movements

To analyse the consequences of tunneling on structures, a precise prediction of ground movements due to tunneling is required. There exist different approaches for evaluating the ground movements induced by tunneling. The approaches include empirical and analytical relations, centrifuge tests, and numerical analyses. The numerical analyses must consider the construction sequence and the soil-structure interaction.

1.3.2.1. Empirical evaluation

These simplified approaches involve predicting surface settlements using a limited number of parameters, which allows the consideration of the size and depth of the excavation, the ground conditions, and the volume of ground loss(Leca et al., 2007). At the ground surface, a “settlement trough” is the result of tunnel-induced movement. The development of the surface settlement trough above and ahead of the advancing heading in the case of a single tunnel in "greenfield" conditions is shown in Figure 1.10.

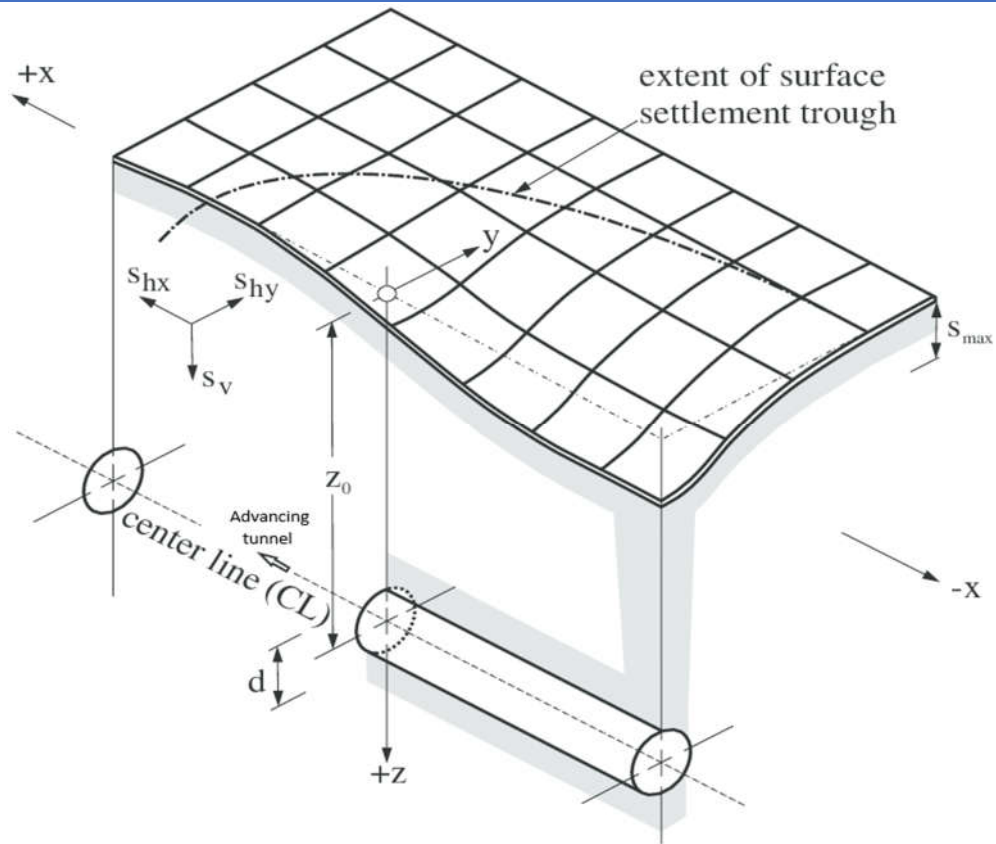


Figure 1.10. Settlement trough above an advancing tunnel(Attewell et al, 1986).

a. Transverse surface settlement

Peck (1969) and subsequently many authors ((Attewell, P B; Yeates, J; Selby, 1986; Mair & Taylor, 1997; O'REILLY & NEW, 1982b), found that the ground surface settlement induced by tunneling may be expressed as a Gaussian distribution. The vertical transverse settlement is given by Equation 1.1:

$$S_V(y) = S_{Vmax} \cdot e^{-\frac{y^2}{2i^2}} \quad (1.1)$$

Where, S_{Vmax} is the maximum ground settlement above the tunnel centreline,

y is the horizontal distance from the tunnel centreline,

i is the horizontal distance from the tunnel axis to the point of inflection of the surface settlement trough as shown in Figure 1.11.

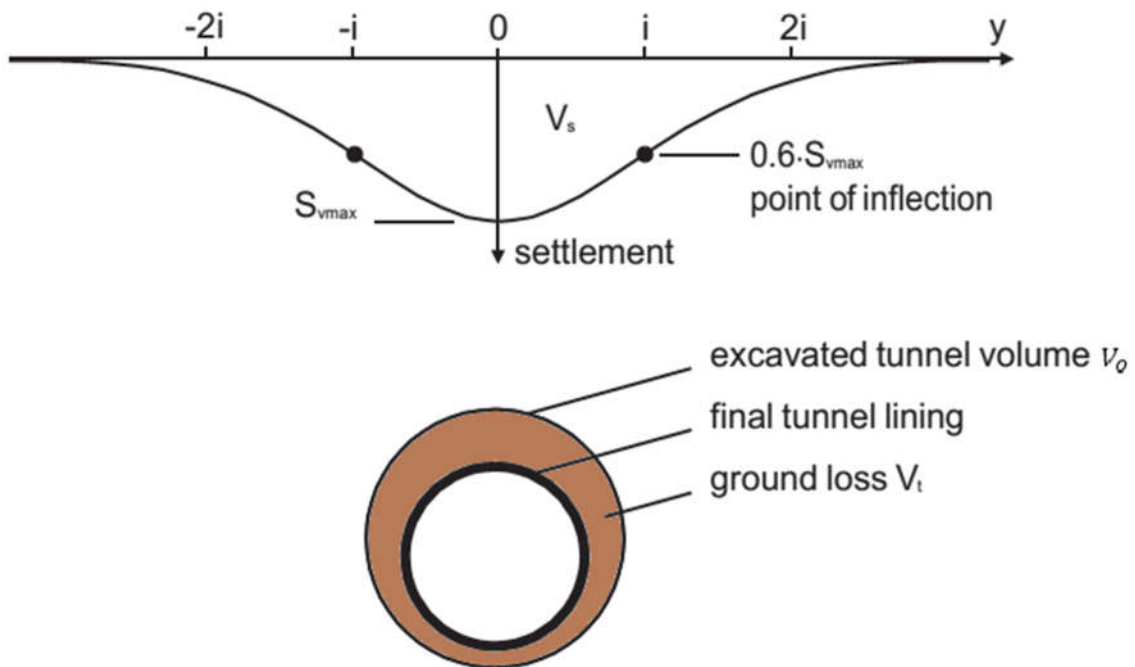


Figure 1.11. The Gaussian curve for transverse settlement trough and volume loss V_L .

The volume of the settlement trough per unit length of the tunnel is obtained by integrating Equation 1.1. However, this equation cannot be integrated directly to obtain such a volume (Addenbrooke, 1996). The volume of settlement trough (per unit length of the tunnel) was derived by Attewell & Farmer, (1974) to give Equation 1.2:

$$V_s = \int S_V(y) \cdot dy = \sqrt{2\pi} \cdot i \cdot S_{Vmax} \quad (1.2)$$

Where, V_s is the volume of settlement trough

The ground or volume loss V_L which is the volume of the ground that settles into the tunnel after it has been constructed also has to be considered. The volume of settlement trough V_s equals the volume loss V_L if there is no volume change (characteristic of stiff clays under undrained conditions) while V_s is usually less than V_L in dense sands because of dilation (Leca, 2019). Differences, on the other hand, tend to be minor and $V_s \approx V_L$ can be assumed. Immediate tunneling-induced settlements are frequently characterized by the volume loss ratio VLR defined as the volume of the surface settlement trough per unit length V_s expressed as a percentage of the excavated tunnel volume. This expression is given in Equation 1.3.

$$VLR = \frac{V_L}{V_o} \cong \frac{V_s}{V_o} \quad (1.3)$$

where, V_o is the excavated tunnel volume per unit length.

The transverse settlement can be expressed in terms of volume loss by combining Equations 1.1 to 1.3 to give Equation 1.4 expressing the maximum vertical settlement and Equation 1.5.

$$S_{Vmax} = \frac{V_o}{i\sqrt{2\pi}} \cdot VLR \quad (1.4)$$

and

$$S_V(y) = \frac{V_o}{i\sqrt{2\pi}} \cdot VLR \cdot \exp\left(-\frac{y^2}{2i^2}\right) \quad (1.5)$$

The settlement trough is determined by two parameters, volume loss ratio VLR and the distance to the point of inflection i for the width of the settlement trough. The first derivative of Equation 1.5 gives the slope of the Gaussian curve, and the second derivative gives the curvature(Marshall, 2009).

b. Transverse horizontal surface displacement

Tunneling-induced vertical displacements are larger than horizontal displacements and offer a greater risk of structural damage. However, horizontal displacements may increase the damage level to buildings(Franza, 2016). O'REILLY & NEW (1982) demonstrated that the above equations for surface settlement can be used to calculate the horizontal surface displacement in the transverse direction by supposing that resultant ground displacement vectors are directed towards the centre of the tunnel. As a result of this supposition, the horizontal surface ground displacements in the transverse direction is then given by Equation 1.6.

$$S_h(y) = \frac{y}{z_o} \cdot S_V(y) \quad (1.6)$$

As illustrated in Figure 1.12 below, the maximum horizontal displacement S_{hmax} occurs at the point of inflection of the settlement trough, and this is in agreement with field data observed by Cording & Hansmire (1975).

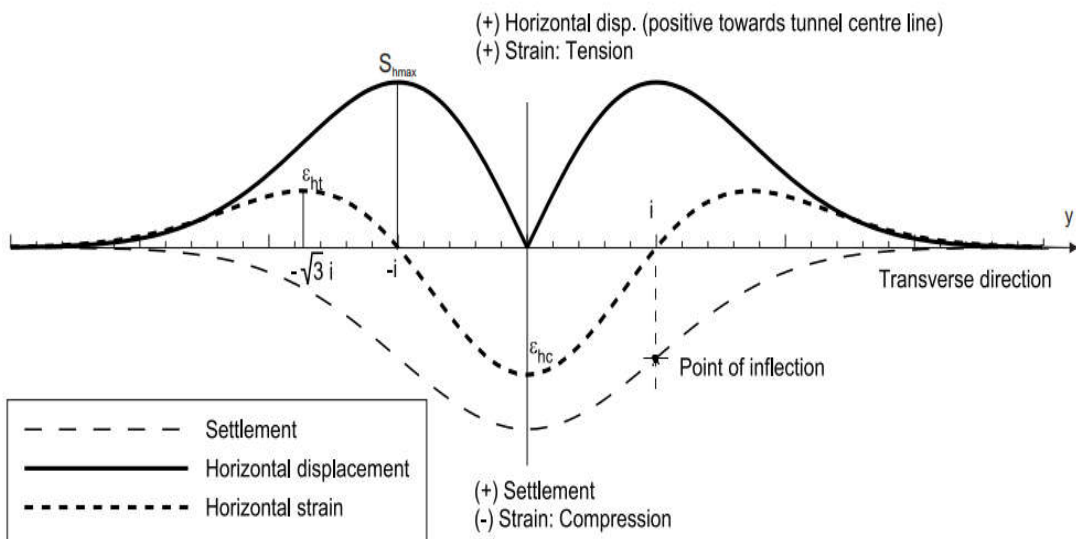


Figure 1.12. Distribution of horizontal surface displacement and strain in the transverse direction together with settlement trough(Franza, 2016).

At the point of inflection, $S_V(y) = 0.6 \cdot S_{Vmax}$. Hence Equation 1.6 can be written as

$$S_{hmax} = \frac{i}{z_o} \cdot 0.6 \cdot S_{vmax} \quad (1.7)$$

The horizontal strains are very important when describing deformations of buildings. By differentiating the horizontal displacement with respect to y , we can obtain the horizontal strain ϵ_{hy} at any location on the ground surface as expressed in Equation 1.8.

$$\epsilon_h(y) = \frac{S_v(y)}{z_o} \left(\frac{y^2}{i^2} - 1 \right) \quad (1.8)$$

As shown in Figure 1.12, in the zone $-i < y < i$ (the sagging zone), the horizontal strains are compressive. In the hogging zone $y < -i \cup y > i$, the horizontal strains are tensile. The maximum values of strains occur at $y = 0$ (compression) and $y = \sqrt{3}i$ (tension).

c. Longitudinal surface settlement

By treating a tunnel as a series of point sources in the longitudinal direction and superimposing the settlement craters created by each point source, the longitudinal settlement profile can be estimated(Attewell & Woodman, 1982). If a Gaussian settlement profile is adopted for the settlement crater, the longitudinal settlement profile follows the shape of a

cumulative probability curve. The settlement above the tunnel center line in the longitudinal direction can be obtained from Equation 1.9 below.

$$S_v(x) = S_{vmax} \cdot \frac{1}{i\sqrt{2\pi}} \cdot \int_{-\infty}^x e^{-\frac{x^2}{2i^2}} \quad (1.9)$$

Where, x is the distance from the tunnel face in the longitudinal direction of the settlement trough, as shown below in Figure 1.13.

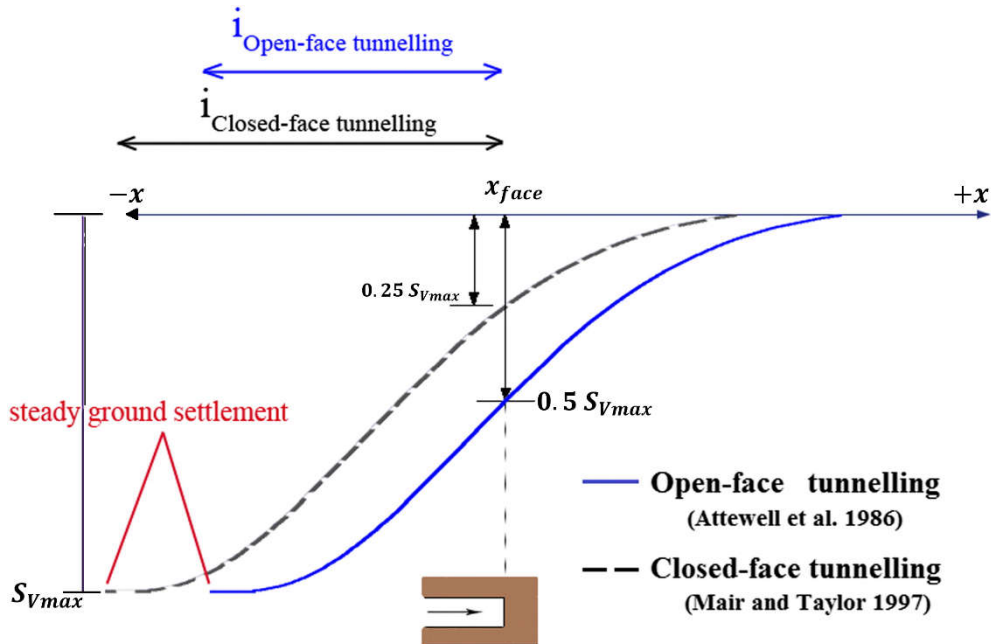


Figure 1.13. Longitudinal settlement trough above tunnel centre line(Hajjar et al., 2015).

Attewell & Woodman, 1982 showed that in stiff clay 30% to 50% of S_{vmax} occurs directly above the tunnel face with an average value of about 40%. The tunnel face is frequently considered to be at $x = 0$ where 50% of S_{vmax} is assumed for convenience. In the case of open face tunneling, this assumption is more relevant. For closed-face tunneling, much lower values of about 25% to 30% are obtained, resulting in a translation of the longitudinal settlement profile(Mair & Taylor, 1997) as seen in Figure 1.13.

By assuming that the resultant displacement vectors point towards the centre point of the tunnel face, Attewell & Woodman (1982) demonstrated that the horizontal surface displacement in the longitudinal direction can be given by Equation 1.10 below:

$$S_{hx}(x)_{y=0} = \frac{VLR \cdot D^2}{8z_o} e^{-\frac{x^2}{2i^2}} \quad (1.10)$$

Where, $S_{hx}(x)_{y=0}$ is the horizontal displacement in the longitudinal direction.

The derivative of S_{hx} with respect to x gives the longitudinal horizontal strain above the tunnel axis (Equation 1.11).

$$\epsilon_{hx}(x)_{y=0} = -x \frac{VLR \cdot D^2}{8i^2 z_o} e^{-\frac{x^2}{2i^2}} \quad (1.11)$$

Where, $\epsilon_{hx}(x)_{y=0}$ represents the horizontal strain above the tunnel axis.

Tension occurs ahead of the tunnel face and compression behind the tunnel face.

d. Settlement trough width

The distance between the tunnel centre line and the inflection point i of the settlement trough is commonly used to calculate the trough width.

i. Surface trough width

O'REILLY & NEW (1982) proposed the most commonly used relationship between surface trough width and tunnel depth. The authors performed multiple linear regression analyses based on 19 case studies using field data to state that there is an approximately linear relationship between the trough width and tunnel depth. They showed there is no substantial relationship between i and tunnel diameter (unless in very shallow tunnels with a cover to diameter ratio of less than one, where this relationship is not valid) or construction method. Its formulation is given by Equation 1.12.

$$i = K \cdot z_o \quad (1.12)$$

Where, K is the trough width parameter, with K approximately 0.4-0.5 for stiff fissured clay, 0.6-0.7 for soft clay, and 0.2-0.3 for sands above the water table.

According to Mair and Taylor [1997], K should be 0.5 for clay and 0.25-0.45 for coarse-grain soils. Rankin (1988) who presented a range of tunnel case histories on clayey, sandy, residual, and mixed grounds, validated the methodology of Equation 1.12.

According to (New & O'Reilly, 1991), the trough width for layered ground can be calculated using K_i for the soil type in each layer of thickness z_i as shown by Equation 1.13:

$$i = K_1 \cdot z_1 + K_2 \cdot z_2 + \dots \quad (1.13)$$

This formula agrees well with field observations of tunnels in sands overlain by clay layers(Mair & Taylor, 1997).

ii. Subsurface trough width

Estimating subsurface displacements is necessary for assessing the possible interaction of tunnels with existing subsurface structures such as piles and existing tunnels. Using a centrifuge experiment, Mair & Taylor (1993) demonstrated that subsurface settlement troughs in undrained clays can also be effectively fitted with a Gaussian curve. They suggested calculating i using Equation 1.14 as:

$$i(z) = K \cdot (z_0 - z), \quad (1.14)$$

Where, z is the depth considered.

The value of K was found to vary with depth. For tunnels in clay, Mair et al. (1993) provided Equation 1.15, which shows that K varies non-linearly with depth, z .

$$K = \frac{0.175 + 0.325 \cdot (1 - z/z_0)}{1 - z/z_0} \quad (1.15)$$

The values of i from subsurface settlement measurements have been plotted against depth, z , in Figure 1.14, and both i and z have been normalized by the tunnel axis depth, z_0 . The dashed line corresponds to Equation 1.14 with constant $K = 0.5$, while the solid line corresponds to Equation 1.14 with the value of K gotten from Equation 1.15. MAIR et al. (1993) found that the value of i for subsurface settlement profiles is much higher than would be predicted by a constant K . The prediction with the solid line better fits data from the field and centrifuge tests as seen in Figure 1.14 below.

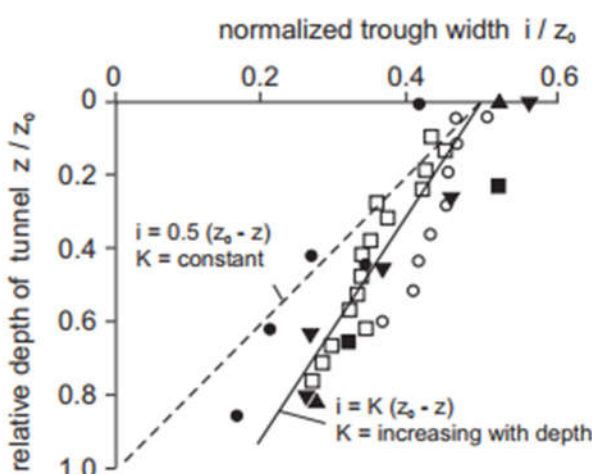


Figure 1.14. Variation of trough width with depth for tunnels in clay(Mair & Taylor, 1993).

1.3.2.2. Numerical analysis of tunnels

The empirical methods presented in the above section predict tunneling-induced ground settlements in greenfield conditions. Tunnel construction often involves interaction between tunnels with other structures such as buildings or other existing tunnels. The empirical methods presented cannot predict these interactions. Numerical modelling, on the other hand, allows for the integration of several aspects of the interaction problem into a single analysis. This section presents an overview of how numerical methods mainly Finite Element Modelling can be used to simulate tunnel excavation.

a. Two-dimensional simulation of tunnel construction

Tunnel construction does, without a doubt, include a three-dimensional stress-strain condition, and while three-dimensional FE analyses have been implemented in engineering practice, they are still time-consuming (Möller, 2006a; Swoboda, 1979). As a result, tunnel excavation is frequently represented in two dimensions (2D). When using plane strain analysis to model tunnel excavation, various methods have been presented to account for stress and strain variations (3D arching effect) ahead of the tunnel face, for example by involving an artificial support pressure or displacement. A brief description of 2D tunnel simulation methods for conventional and closed face shield tunneling is given below.

i. Simulation methods for conventional tunneling

Different 2D approximations are commonly used in engineering practice to simulate the excavation and support sequence of conventional tunneling.

- **Progressive softening method**

It can also be referred to as the core support method. This method was developed by Swoboda (1979) for modelling NATM tunneling as a 2D problem. It involves reducing the stiffness of the soil within the core (tunnel heading) by a factor of β , to create volume loss. Figure 1.15 shows the different simulation phases of this method. In the first simulation phase, initial stresses are computed with a gravity loading but with a reduced core stiffness which leads to a reduced support pressure inside the tunnel. The second simulation phase involves removing the soil inside the tunnel and activating the lining when the reduced soil stiffness reaches the desired value.

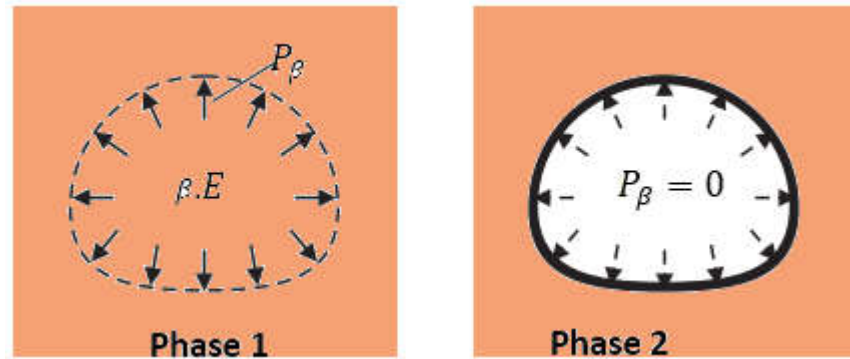


Figure 1.15. Simulation phases of the Progressive softening method.

- **Stress reduction method (λ -method)**

This method which is also known as the λ -method or the convergence confinement method was proposed by Panet & Guenot (1983). The ground elements inside the tunnel are switched off and the boundary is subjected to a force vector that is equal to the initial radial soil stresses σ_o acting on the inside of the tunnel minus $\lambda \cdot \sigma_o$.

$$\sigma_r = (1 - \lambda)\sigma_o \quad (1.16)$$

Where: σ_r is the radial stresses applied to the tunnel boundary, and λ is an unloading parameter ($0 < \lambda < 1$).

The lining is installed when the reduced tunnel stress reaches the desired value and the corresponding stress $(1 - \lambda)\sigma_o$ is shared between the ground and lining. Figure 1.16 below illustrates convergence confinement method.

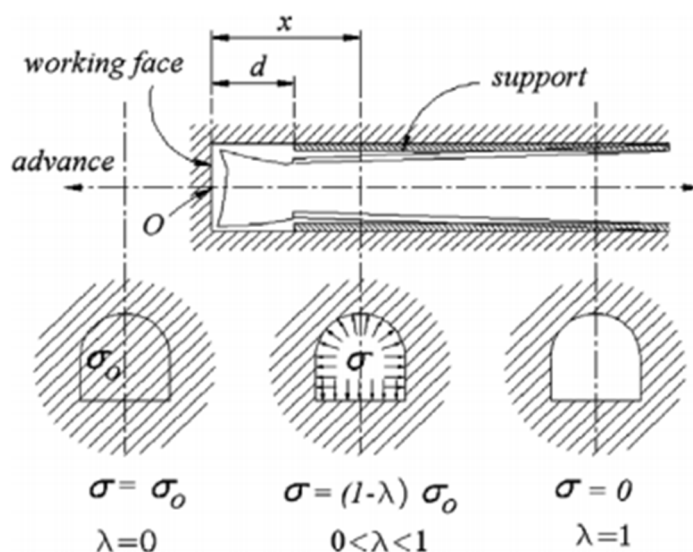


Figure 1.16. Principle of convergence confinement method.(González-Nicieza et al., 2008).

ii. Simulation methods for closed face tunnelling

When adopting numerical analysis to simulate shield tunnel excavation, the ground in front of the shield machine, which will move radially and axially towards the tunnel face, must be properly considered. A volume loss occurs due to deformation and also if the gap between the diameter of the cut surface and the exterior diameter of the tunnel lining is not filled with grout. Different methods such as the gap method and the volume loss control method have been proposed to simulate volume loss in 2D finite element analysis.

- **The gap method**

The gap approach was suggested by Rowe et al., (1983) to simulate tunnels as a 2D problem. He considered volume loss in terms of a vertical gap between the tunnel lining and the initial excavation boundary, as illustrated in Figure 1.17.

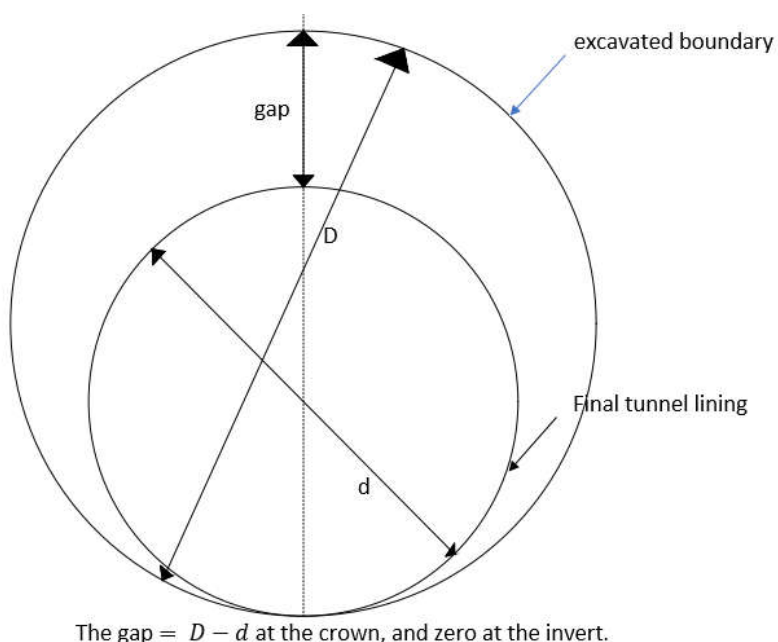


Figure 1.17. Gap method for modelling tunnel excavation(Rowe et al., 1983).

The tunnel's invert is supported on the underlying soil, and a gap is prescribed at the crown. The final shape of the tunnel is defined by a lining. The ground is unsupported and free to move until the void is closed and the ground makes contact with the lining, the ground-lining interaction is then activated.

- **Volume loss control method**

This is a stress reduction method that has been proposed to simulate the 2D installation of shield tunneling. Unloading factors have been replaced with control of ground loss since the value of unloading factors is unclear and shield tunneling is controlled by the

amount of ground loss(Addenbrooke et al., 1997). As shown in Figure 1.18, in the first calculation phase, the stresses inside the tunnel are decreased step by step, and the corresponding ground loss is determined after each step.

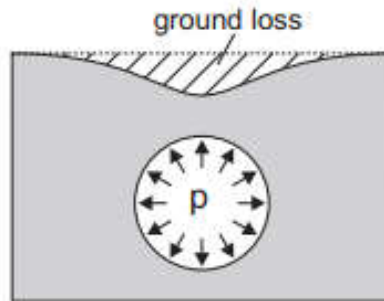


Figure 1.18. Volume loss control method by ADDENBROOKE et al. (1997).

The lining is activated when the prescribed ground loss is attained at corresponding pressure P . This is accomplished by dividing the volume of soil moving into the tunnel by the tunnel's original volume per unit length(Haji, 2017). If the analysis is only concerned with ground displacement (and no results of lining stresses and moments are required), it can be stopped after the required volume loss has been obtained.

b. Three-dimensional simulation of tunnel construction

To simulate tunnel construction of conventional driven tunnels and shield tunnels, numerous installation approaches have been developed. Several writers use a "step-by-step" technique(KATZENBACH & Breth, 1981), in which tunnel excavation is modelled by removing tunnel face elements one at a time while installing a lining at a distance behind the tunnel face. This distance is referred to as the excavation length.

i. Step-by-step simulation for conventional tunnelling

The so-called step-by-step method is used to model the open face tunnelling excavation process. Ground elements inside the tunnel are eliminated to simulate an unsupported excavation with a specific advanced length d in all calculation steps. Each computing phase i begins with an excavation in which one strip of the soil elements is turned off. A ring of new lining elements is turned on during the same phase to support the preceding excavation $i - 1$. In steps $i + 1$ through $i + n$, these computation phases are repeated until a representative steady-state solution (solution with a constant horizontal shape of the centreline settlements) is produced. The excavation sequence is shown in Figure 1.19, starting with initial geostatic stresses.

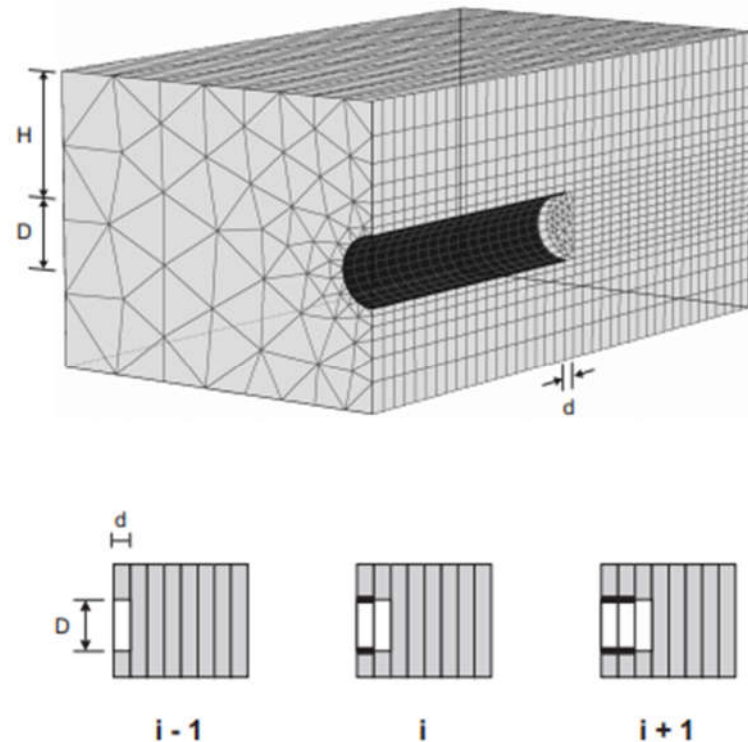


Figure 1.19. Step by step simulation of conventional tunnelling(Möller, 2006).

ii. Step by step pressure method for closed shield tunnelling

Closed shield tunnelling is a continuous process involving the installation of lining segments and continual support pressure. However, a step-by-step technique is required for numerical discretization.

A detailed explanation of the pressure method for both slurry shield and EPB shield is provided in Möller, (2006). A somewhat high axial pressure simulates the slurry at the tunnel's face, a slightly lower radial pressure simulates the shield, and a radial pressure simulates the fresh grout in the tail void behind the shield. The grout pressure is assumed to be the same as the radial shield pressure, with both pressures increasing hydrostatically with depth. It is applied on the shield and two lining rings behind it. A ground lining gap is modelled by deactivating ground elements with a thickness of around 8cm -20cm and a length of around $l = 1.5m$. Ground displacements are kept to a minimum so that the ground lining gap is not exceeded. The grout is considered to be hardened for consecutive lining rings, and the radial pressure is turned off while activating volume elements to fill up the gap.

For numerical purposes, the step-by-step pressure approach shown in Figure 1.20 is used to model excavation for slurry shields.

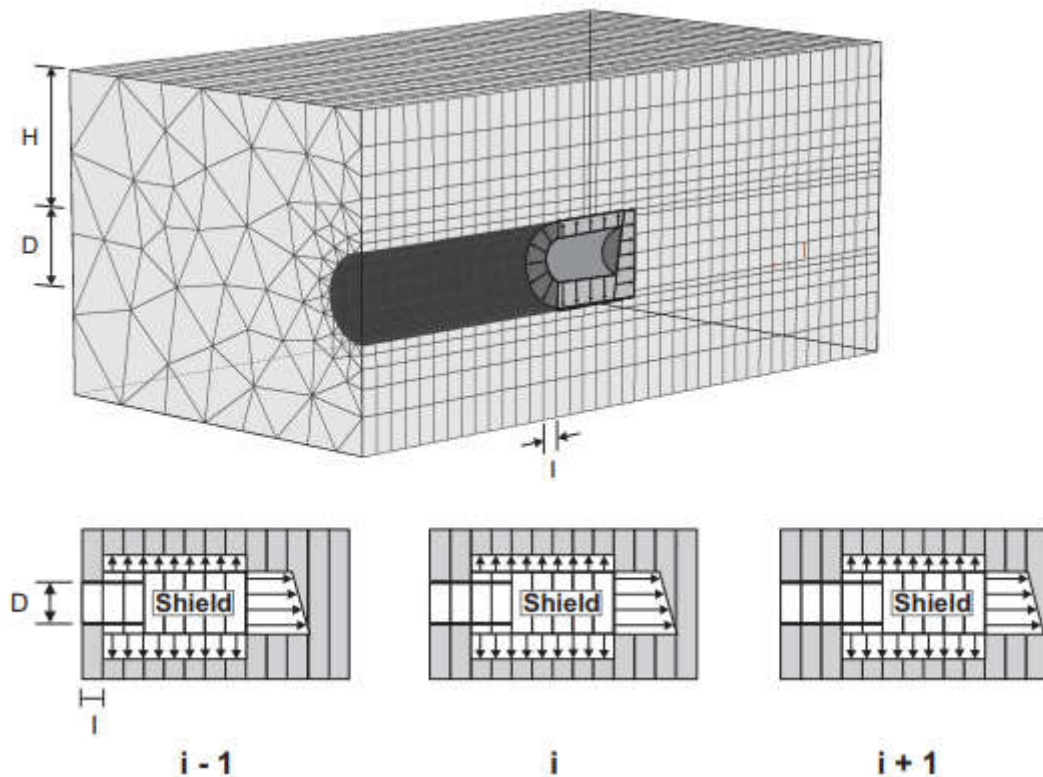


Figure 1.20. Shield tunnelling using a step-by-step pressure approach.

For the sake of convenience, this same approach can be used to model EPB shields. A tunnel advance of one segment length l is simulated in each computing phase i with one slice of ground elements turned off. Pressure is exerted in the new tunnel slice and five following shield slices at the same time. Shell elements model the entire lining behind the shield. As previously stated, the first two rings of shell elements are surrounded by a pressurized gap. In steps $i + 1$ through $i + n$, the calculation phases are repeated until a steady-state solution is produced.

1.4. Building damage induced by ground movements

The construction of tunnels is known to cause movements at the ground surface in the form of a settlement trough as explained in previous chapters. In urban areas, these ground movements may cause damage to existing surface structures. Tunnel-induced deformation of such structures must be predicted and the risk of damage assessed as part of the planning, design, and construction of tunnels in an urban environment(Mair et al., 1996).

1.4.1. Definitions of building damage parameters

To define building deformation, Burland & Wroth (1974) provided a consistent set of definitions based on the displacements (either measured or estimated) of several discrete points on the foundations of a building. These deformation parameters shown in Figure 1.21 are widely accepted.

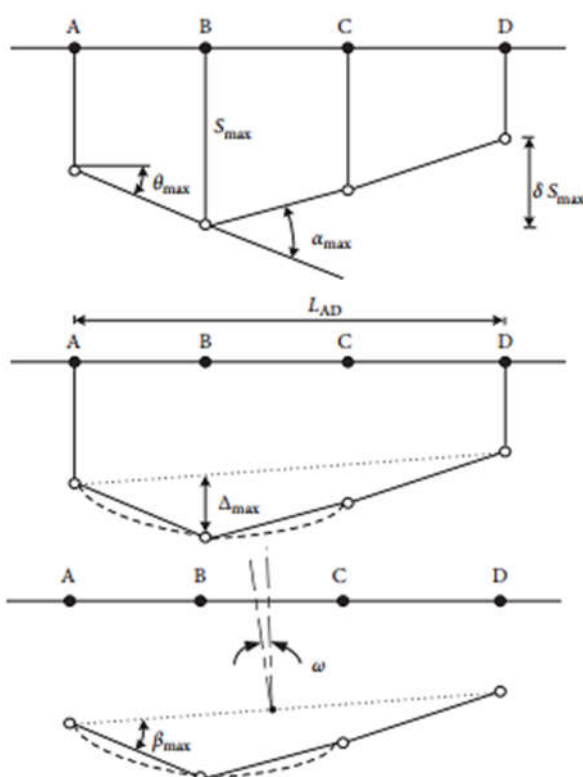


Figure 1.21. Definition of building deformation(J. B. Burland, 1995).

These deformation parameters are defined as follows:

- **Settlement** defines the vertical movement of a point. Positive values indicate downwards movement. It is denoted by S .

- **Relative settlement (differential settlement)** δS_V is the difference between two settlement values.
- **Rotation or slope θ** is the change in gradient of a line joining two reference points (e.g., AB in Figure 1.21). Rotation is typically used to describe the slope of the settlement trough.
- **Angular strain α** is shown in Figure 1.21. It produces sagging or upward concavity when positive while hogging or downward concavity is described by a negative value.
- **Relative deflection Δ** is the displacement of a point relative to the straight line connecting two reference points with a distance L. The sign convention is the same as for angular strain, positive values for sagging.
- **Deflection ratio DR** is defined as the quotient of relative deflection and the corresponding length: $DR = \Delta/L$.
- **Tilt ω** describes the rigid body rotation of the whole superstructure or a well-defined part of it.
- **Relative rotation or angular distortion β** is defined as the rotation of the straight line joining two reference points, relative to the tilt.
- **Average horizontal strain ϵ_h** is defined as a change in length δL over the corresponding length L. It is a term used to describe the direct movement of building structures in a lateral direction.

The definitions above only apply to 'in-plane' deformation. Twisting and other three-dimensional behaviours are not included.

1.4.2. Damage assessment criteria

Several ways to quantifying building damage were summarised by Burland et al. (1977). When it came to assessing building damage, they divided it into categories, following those employed by Skempton and MacDonald (1956), who examined records of nearly 100 buildings and correlated damage with angular distortion β , concluding that cracking occurs when $\beta > 1/300$ and structural damage occurs when $\beta > 1/150$.

Burland et al., (1977) distinguished between three criteria: visual appearance, serviceability or function, and stability. They noted that visual damage is difficult to quantify because it is based on subjective criteria. They proposed the damage classification scheme shown in Table 1.1 based on ease of repair. Because the emphasis is on the ease of repair, crack width is used as an additional indicator rather than a direct measure in this list. The descriptions in Table 1.1 only

relate to standard domestic or office buildings and may not be applicable for a structure with valuable or sensitive finishes(J. B. Burland, 2008).

Table 1.1. Classification of visible damage to walls with particular reference to ease of repair of plaster and brickwork or masonry after Burland (1995)(Franzius, 2003).

Category of damage	Normal degree of severity	Description of typical damage	Approximate crack width (mm)
0	Negligible	Hairline cracks	0-0.1
1	Very slight	Fine cracks, which can easily be treated during normal decoration. Perhaps isolated slight fracturing in the building. Cracks in external brickwork are visible on close inspection.	0.1-1
2	slight	Cracks are easily filled. Re-decoration is probably required. Recurrent cracks can be masked by suitable linings. Cracks may be visible externally and some repainting may be required to ensure water tightness. Doors and windows may stick slightly.	1-5
3	Moderate	The cracks require some opening up and can be patched by mason. Repainting of external brickwork and possibly a small amount of brickwork to be replaced. Doors and windows sticking. Service pipes may fracture. Weathertightness is often impaired.	5-15(or several up to 3mm)
4	Severe	Extensive repair work involving breaking out and replacing sections of walls, especially over doors and windows. Windows and door frames distorted, floors sloping noticeably. Walls leaning or bulging noticeably, some loss of bearing in beams. Service pipes disrupted.	15-25 (but also depends on the number of cracks.)
5	Very severe	This requires a major repair job involving partial or complete rebuilding. Beams lose bearing, walls lean badly and require shoring. Windows broken with distortion. Danger of instability.	>25 (but also depends on the number of cracks.)

Note: Local deviation of slope, from the horizontal or vertical, of more than 1/100 will normally be clearly visible. Overall deviations above 1/150 are undesirable.

The six categories in this classification can be further broken into the three damage level groups indicated above. Aesthetical damage is represented by categories 0 to 2. Damage to the structure's serviceability happens in categories 3 and 4, whereas damage to the structure's stability occurs in category 5. Damage of categories 0 to 2 can be caused by a variety of internal factors, such as heat effects while damage of category 3 or higher, on the other hand, is typically related to ground displacement(J. B. Burland, 1995).

1.4.3. Building strains assessment to evaluate building damage

Tensile strain is often, but not always, the cause of cracking in masonry walls and finishes. Burland & Wroth, 1974 initially described the critical tensile strain ϵ_{crit} measured over a length of 1m which is linked to the onset of visible cracking in structures. They found that $\epsilon_{crit} = 0.05\% - 0.1\%$ for brick work and $\epsilon_{crit} = 0.03\% - 0.05\%$ for concrete. These values, according to Burland & Wroth (1974), are greater than the local tensile strain associated with tensile failure. Burland et al., (1977) introduced the concept of limiting tensile strain ϵ_{lim} to replace critical tensile strain ϵ_{crit} as a serviceability parameter which can be varied to take account of differing material and serviceability limit states.

Boscardin & Cording, (1989) developed the concept of limiting tensile strain by relating strain values to building damage seen in 17 case studies of excavation-induced subsidence. They related the values of limiting strain to the likely severity of damage. Table 1.2 summarises this relationship, establishing a link between building deformation and possible structural damage.

Table 1.2. Relation between category of damage and limiting tensile strain(Boscardin & Cording, 1989; J. B. Burland, 1995).

Category of damage	Normal degree of severity	Limiting tensile strain [%]
0	Negligible	0-0.05
1	Very slight	0.05-0.075
2	Slight	0.075-0.15
3	Moderate*	0.15-0.3
4 to 5	Severe to very severe	>0.3

In the evaluation of damage to buildings owing to ground movements, Burland et al. (1977) and Burland & Wroth (1974) devised the equivalent beam approach, in which the

building is represented by an elastic rectangular deep beam of length L and height H . (Figure 1.22). The goal of this approach is to determine the tensile strains in the beam for a certain deflected shape of the building foundations, and hence the deflection ratio Δ/L at which cracking begins.

Burland & Wroth considered two extreme modes of deformation: flexure only about a neutral axis at the center and shearing only. In bending only (Figure 1.22d), cracking is caused by direct tensile strain while in shear (Figure 1.22e) diagonal cracks appear, caused by diagonal tensile strains. The equivalent beam approach is presented in Figure 1.22 below.

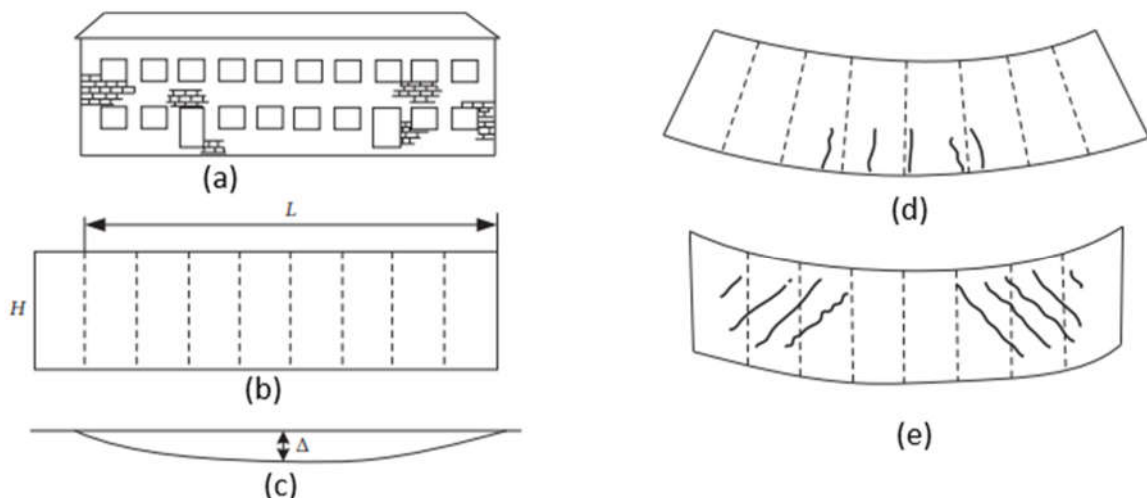


Figure 1.22. The equivalent beam approach (J. B. Burland & Wroth, 1974). (a) Actual building. (b) Beam: simple idealisation of building. (c) Deflected shape of soffit of beam. (d) Bending deformation with cracking due to direct tensile strain. (e) Shear deformation with cracking due to diagonal tensile strain.

In most cases, both forms of deformation will occur at the same time, so you'll need to compute both bending and shear strains to figure out which is limiting. Timoshenko (1955) provided the expression to calculate the total central deflection of a centrally loaded beam subjected to combined shear and bending deformation as given by Equation 1.17:

$$\Delta = \frac{PL^3}{48EI} \left(1 + \frac{18EI}{HGL^2} \right), \quad (1.17)$$

Where, Δ is the total central deflection,

E is the Young's modulus,

G is the shear modulus,

P is the point load which is applied at the centre of the beam, and

I is the second moment of area about the neutral axis.

For an isotropic elastic material $E/G = 2(1 + \nu)$. The value $E/G = 2.6$ is obtained by assuming a Poisson's ratio of $\nu = 0.3$. Burland & Wroth (1974) expressed deflection ratio Δ/L in terms of maximal extreme fibre strain ϵ_{bmax} when the neutral axis is in the middle of the beam (beam undergoing sagging) as given by Equation 1.18:

$$\frac{\Delta}{L} = \left(0.167 \frac{L}{H} + 0.65 \frac{H}{L} \right) \epsilon_{bmax} \quad (1.18)$$

Where, $\frac{\Delta}{L}$ is the deflection ratio, and

ϵ_{bmax} is maximal extreme fibre strain.

and in terms of the maximum diagonal strain ϵ_{dmax} :

$$\frac{\Delta}{L} = \left(0.25 \frac{L^2}{H^2} + 1 \right) \epsilon_{dmax} \quad (1.19)$$

By setting $\epsilon_{max} = \epsilon_{lim}$, Equations 1.18 and 1.19 define the limiting values of Δ/L for the deflection of simple beams. The maximum of the values of ϵ_{bmax} and ϵ_{dmax} generated by Equations 1.18 and 1.19 can be used to estimate the maximum tensile strain in the building for a given deflection ratio Δ/L . Equations 1.18 and 1.19 are represented below in Figure 1.23, with Δ/L normalised by ϵ_{lim} .

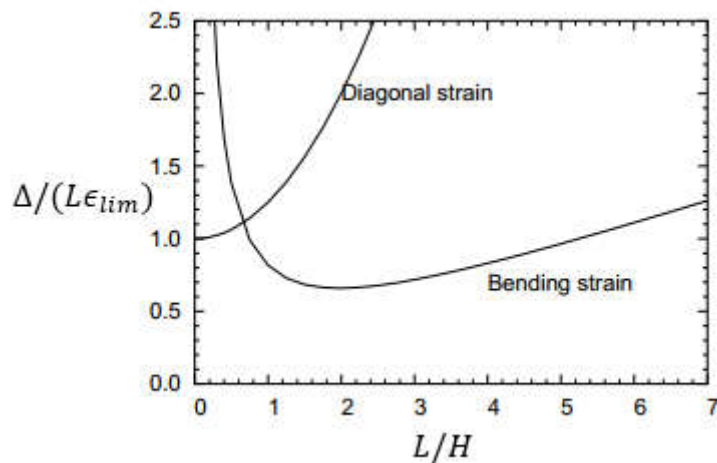


Figure 1.23. Relationship between $\Delta/(L\epsilon_{lim})$ and L/H for rectangular beams deflecting due to combined bending and shear. Neutral axis in the middle (sagging mode).

It can be seen that for $L/H < 0.5$, the diagonal strain is critical and as L/H increases above this value, the bending strains become the critical mode of deformation.

Burland and Wroth demonstrated that hogging deformation mode is generally more damaging than sagging mode. As a result, it may be more reasonable to place the neutral axis towards the bottom extreme fibres. This led to Equations 1.20 and 1.21 as follows:

$$\frac{\Delta}{L} = \left(0.083 \frac{L}{H} + 1.3 \frac{H}{L} \right) \epsilon_{bmax} \quad (1.20)$$

$$\frac{\Delta}{L} = \left(0.064 \frac{L^2}{H^2} + 1 \right) \epsilon_{dmax} \quad (1.21)$$

Equation 1.20 only applies to a hogging deformation mode because the neutral axis is at the lower extreme fibre. There are no tensile strains in the case of sagging. Equations 1.20 and 1.21 have been illustrated in Figure 1.24. It can be seen that diagonal strains (shear strains) become critical if $L/H < 1.3$, while for $L/H > 1.3$, the bending strains dominate.

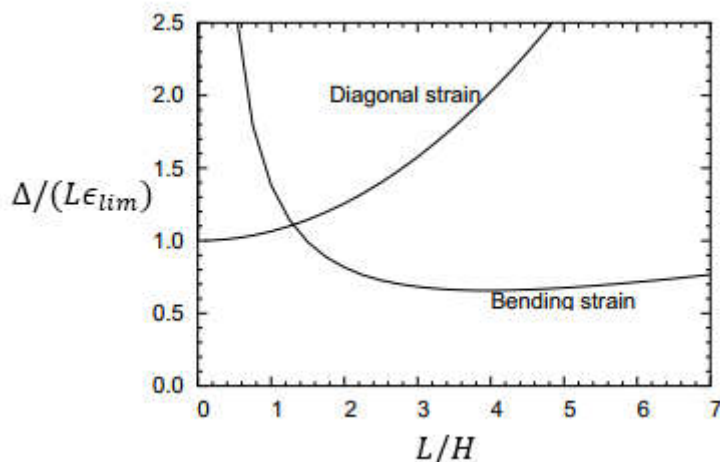


Figure 1.24. Relationship between $\Delta/(L\epsilon_{lim})$ and L/H for rectangular isotropic beams (hogging mode)(J. B. Burland & Wroth, 1974).

Tunneling induced ground movements do not only involve hogging and sagging, but horizontal displacements or strains also develop as was shown in section 1.3.2. Boscardin & Cording (1989) included horizontal strain ϵ_h which excavations can induce, in the above analysis by superposition of horizontal strain with the strain developed due to deflection deformation (Burland and Wroth's bending and shear strains). In the case of bending, the resultant extreme fibre strain ϵ_{br} is given by Equation 1.22.

$$\epsilon_{br} = \epsilon_{bmax} + \epsilon_h. \quad (1.22)$$

In the shearing region, the resultant diagonal tensile strain can be expressed using Mohr's circle of strain and is given by Equation 1.23.

$$\epsilon_{dr} = \epsilon_h \frac{1-v}{2} + \sqrt{\epsilon_h^2 \left(\frac{1-v}{2}\right)^2 + \epsilon_{dmax}^2}, \quad (1.23)$$

Where, ϵ_{dr} is resultant diagonal strain, and

v is the Poisson's ratio of the equivalent beam.

A building damage interaction diagram can be developed using the values of ϵ_{lim} associated with the various categories of damage listed in Table 1.2 and Equations 1.20 to 1.23 to show the relationship between Δ/L and ϵ_h for an isotropic beam undergoing hogging for a particular value of L/H (J. B. Burland, 1995). For the bending case, combining Equations 1.20 and 1.22 imposing $\epsilon_{br} = \epsilon_{lim}$ yields Equation 1.24.

$$\frac{(\Delta/L)}{\epsilon_{lim}} = \left(0.083 \frac{L}{H} + 1.3 \frac{H}{L}\right) \left(1 - \frac{\epsilon_h}{\epsilon_{lim}}\right). \quad (1.24)$$

For the shearing case, with $\epsilon_{dr} = \epsilon_{lim}$, Equations 1.21 and 1.23 gives Equation 1.25 below.

$$\frac{(\Delta/L)}{\epsilon_{lim}} = \left(0.064 \frac{L^2}{H^2} + 1\right) \sqrt{1 - 0.7 \frac{\epsilon_h}{\epsilon_{lim}} - 0.3 \left(\frac{\epsilon_h}{\epsilon_{lim}}\right)^2}. \quad (1.25)$$

The damage interaction diagram corresponding to $L/H = 1$ plotted according to Equations 1.24 and 1.25 is presented in Figure 1.25. In this figure, each contour line represents a limiting strain value from Table 1.2.

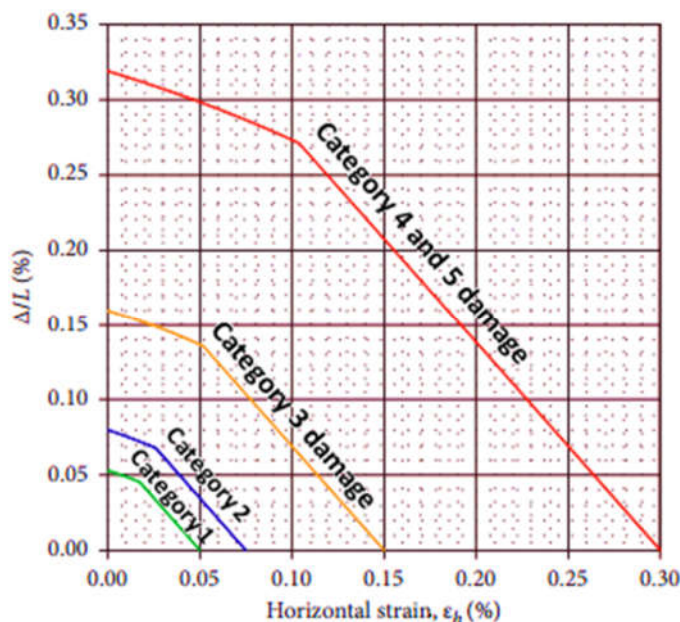


Figure 1.25. Damage interaction diagram for hogging ($L/H=1$), after Burland 1995(Zhang & Zhan, 2021).

Boscardin & Cording (1989) presented similar plots relating category of damage to horizontal strain ϵ_h and angular distortion β instead of deflection ratio as shown in Figure 1.26 for $L/H = 1$. Each contour line represents a value of limiting strain as in Table 1.2. Case studies of tunnel construction, shallow mines, and braced cuttings are also included in Figure 1.26.

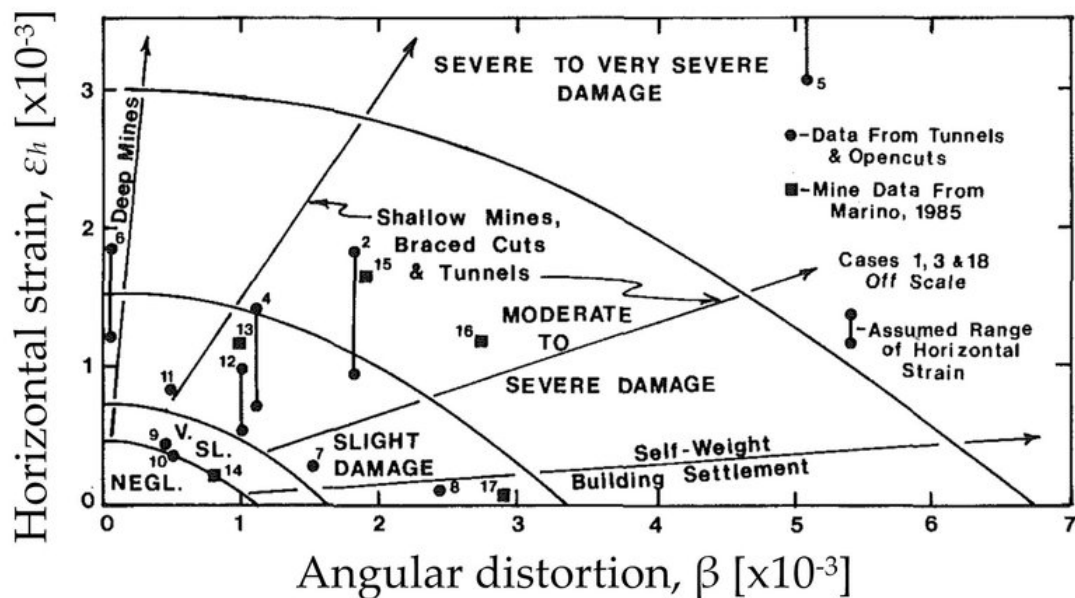


Figure 1.26. Relation of damage to angular distortion and horizontal strain(Boscardin & Cording, 1989).

1.4.4. Soil structure interaction

When estimating the risk of building damage caused by tunnel construction in the above section, it's common to assume that the structure will deform according to the greenfield settlement profile. The deformation parameters such as deflection ratio (shown in Figure 1.27) and horizontal strain are used to quantify the greenfield deformation predicted at the location of an existing structure. These deformation parameters are then related to the category of damage using for example the interaction diagram in section 1.4.3. This approach can be highly conservative as it assumes that the structure is infinitely flexible and follows the greenfield settlement profile(Franzius et al., 2006). The definition of deflection ratio of a highly flexible building is illustrated in Figure 1.27 below.

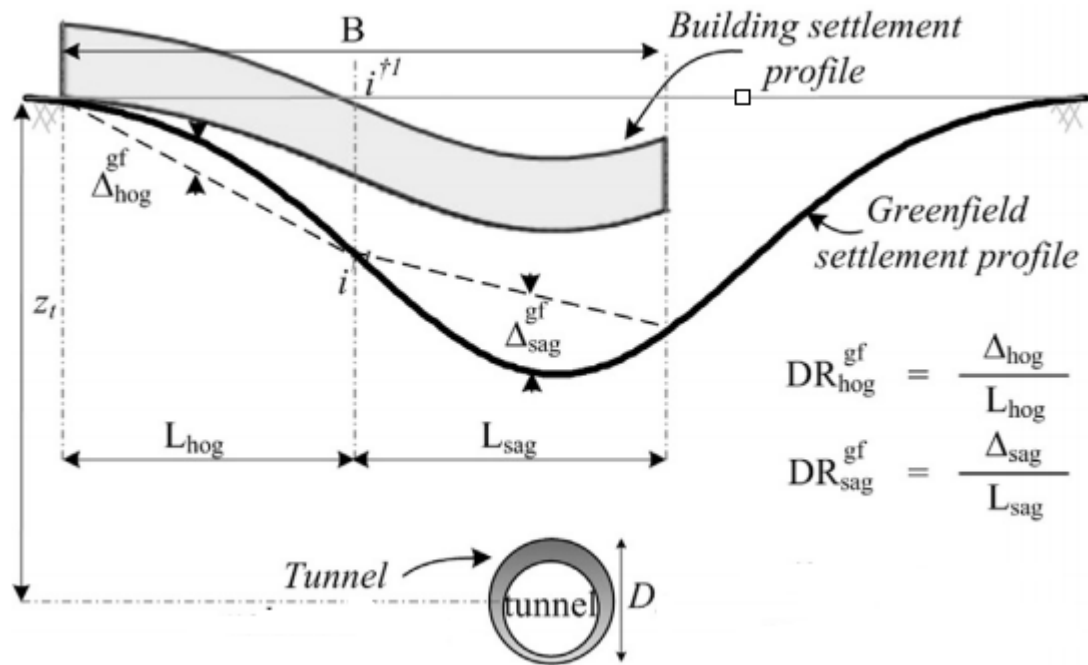


Figure 1.27. Definition of greenfield deflection ratio (Farrell & Mair, 2012).

However, the presence of a structure is likely to alter ground induced soil movement in what is termed the soil structure interaction. The modification of the ground movements may lead to smaller building deformations and levels of damage than may have been predicted by considering the greenfield settlement profile.

Potts & Addenbrooke (1997) devised a method of relating the building's stiffness to that of the soil. The stiffness of the structure was related to that of the soil by defining relative stiffness expressions:

$$\rho^* = \frac{EI}{E_s \left(\frac{B}{2}\right)^4}; \quad \alpha^* = \frac{EA}{E_s \left(\frac{B}{2}\right)} \quad (1.26)$$

Where, ρ^* and α^* are the relative bending and axial stiffness respectively,

EI is the bending stiffness of the structure, EA the axial stiffness of structure, and

E_s is the soil's secant stiffness.

The soil's secant stiffness E_s is obtained at 0.01% axial strain in a triaxial compression test performed on a sample retrieved from half of the tunnel depth. In their analyses, E_s was 103 Mpa and 163 Mpa for tunnel depths of 20 m and 34 m respectively. The geometry of their model is given by the building width B , the tunnel depth z_0 , and the eccentricity e , which is the distance between the building and tunnel centre lines as illustrated in Figure 1.28.

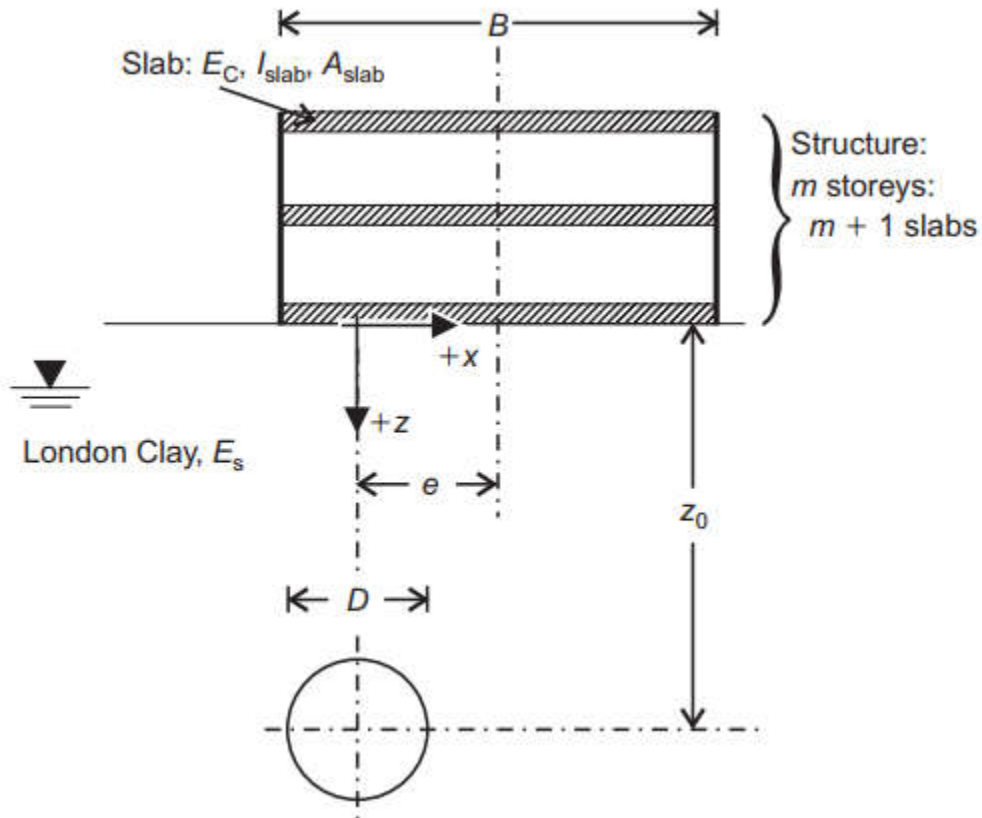


Figure 1.28. Transverse geometry of the interaction problem(Franzius et al., 2006).

Addenbrooke & Potts (1997) applied these relative stiffness expressions to plane strain parametric FE analyses in which buildings were represented by elastic beams. In such a situation, ρ^* has dimension [1/length] while α^* is dimensionless.

The tunnel-induced building deformation was estimated using deflection ratio DR and maximum horizontal strain ϵ_h . The following modification factors were then used to link these deformations to analogous FE greenfield situations as given in Equation 1.27:

$$M^{DR_{sag}} = \frac{DR_{sag}}{DR_{GF}} \quad M^{DR_{hog}} = \frac{DR_{hog}}{DR_{GF}} \quad (1.27)$$

Where, $M^{DR_{sag}}$ and $M^{DR_{hog}}$ are the modification factors for deflection in sagging and hogging respectively,

DR is the deflection ratio displayed by the building, and

DR_{GF} is the greenfield deflection ratio, both defined for sagging and hogging.

Similarly, modification factors are defined for compressive and tensile maximum horizontal strain:

$$M^{\epsilon_{hc}} = \frac{\epsilon_{hc}}{\epsilon_{hc}^{GF}} \quad M^{\epsilon_{ht}} = \frac{\epsilon_{ht}}{\epsilon_{ht}^{GF}} \quad (1.28)$$

Where:

$M^{\epsilon_{hc}}$ and $M^{\epsilon_{ht}}$ are the horizontal strain modification factors for compression and tension respectively.

ϵ_{hc}^{GF} and ϵ_{ht}^{GF} represent the maximum horizontal compressive and tensile strain over the part of the greenfield settlement trough below the building, and

ϵ_{hc} and ϵ_{ht} are the same measure for the building.

Addenbrooke & Potts (1997) demonstrated that the modification variables $M^{DR_{sag}}$ and $M^{DR_{hog}}$ determined from their parametric investigation correlated with relative bending stiffness ρ^* , whilst $M^{\epsilon_{hc}}$ and $M^{\epsilon_{ht}}$ correlated with relative axial stiffness α^* . These data were then given upper bounds to produce a conservative estimate of the variation of the modification factors in relation to the relative stiffness of the structure. Design charts that resulted from these curves are shown in Figure 1.29. The authors proposed to include these design charts into design approach to estimate probable damage caused by tunnel-induced building deformation. This design approach's essential steps are as follows:

- Equations 1.5 and 1.8 are used to predict greenfield settlements and horizontal strains for the geometrical section of the building.
- The structure's bending and axial stiffness must be assessed. Both relative bending and axial stiffness can be calculated using Equations 1.26.
- The modification factors are estimated using the design curves in Figure 1.29a and b.
- These factors are multiplied by the greenfield deformation criterion to obtain modified values that account for the stiffness of the structure.
- Using combinations of DR_{sag} and ϵ_{hc} , and DR_{hog} and ϵ_{ht} in the damage interaction diagrams such as that illustrated in Figure 1.25, the building damage category can be assessed.

The design curves are presented below in Figure 1.29.

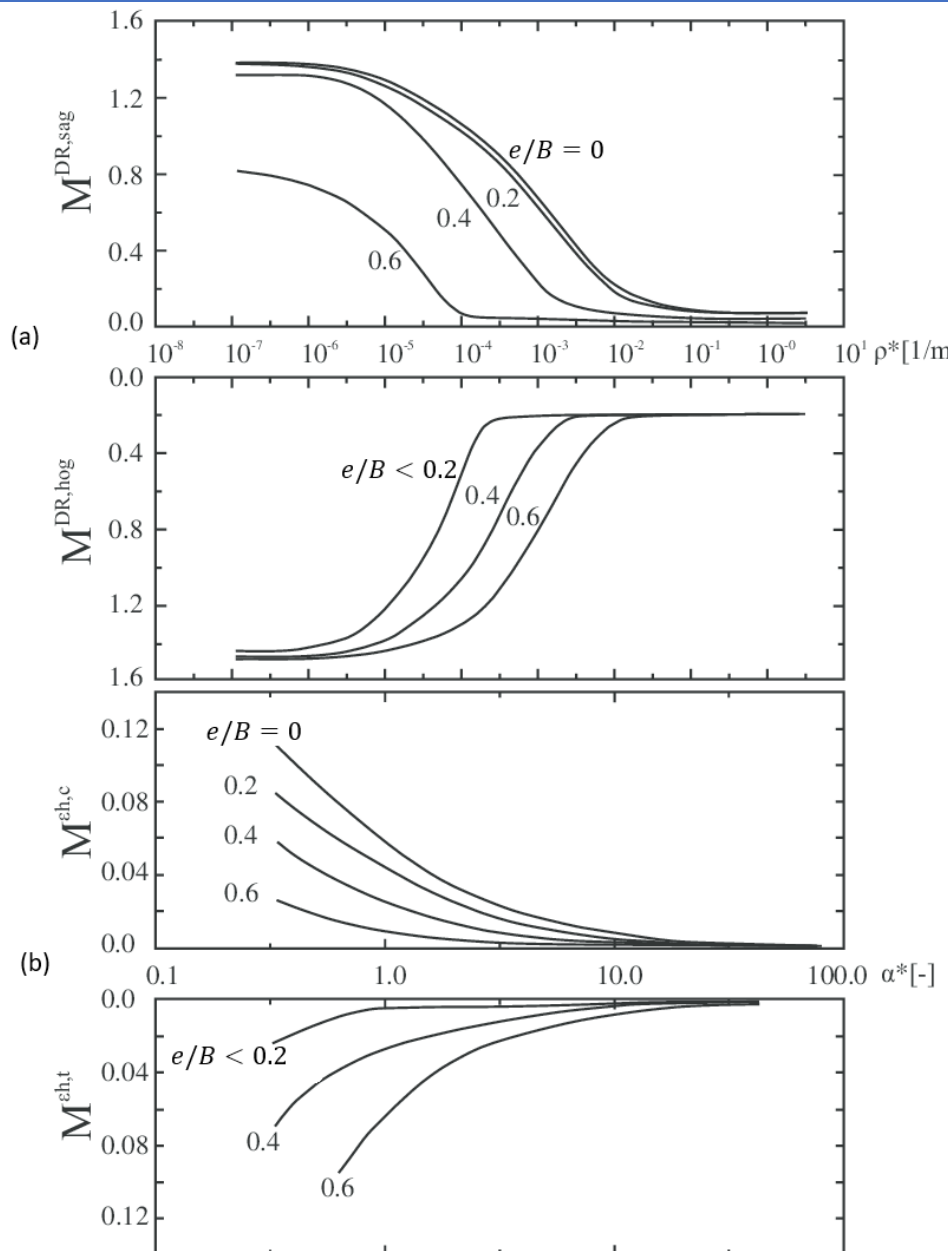


Figure 1.29. Design curves for modification factors of (a) deflection ratio and (b) maximum horizontal strain(Addenbrooke et al., 1997).

Expressions for ρ^* and α^* were later modified by Franzius et al., (2006), the former to be dimensionless as well as the latter when adopted in both 2D and 3D analyses. They presented a larger number of analyses in which additional building features, such as building weight, a smooth interface between the soil and the foundation, and the longitudinal building dimension parallel to the tunnel axis, were modelled. They redefined the following expressions in Equations 1.29 and 1.30 for the modified relative bending and axial stiffness respectively.

$$\rho_{mod}^* = \frac{EI}{E_S z_0 B^2 L} \quad (1.29)$$

$$\alpha_{mod}^* = \frac{EA}{E_s BL} \quad (1.30)$$

Where, ρ_{mod}^* is the modified relative bending stiffness,

α_{mod}^* is the modified relative axial stiffness, and

L is the length of the building in the longitudinal tunnel direction.

1.4.5. Methodology for assessing the risk of damage.

The term "risk" refers to the possible or potential level of damage in terms of the six categories of damage. Typically buildings are considered to be at 'low risk' if the expected category of damage falls within categories 0 to 2(J. Burland, n.d.). Maintaining the level of risk below this threshold is a primary goal of design and construction. Given the concepts described in the above sections on the predictions of tunneling induced ground and building deformations, a rational approach to assess the risk of damage due tunnelling may be developed. J. B. Burland, (1995) suggested a three stage approach for assessing the risk of damage to buildings:

1.4.5.1. Preliminary assessment (First phase).

In this stage the presence of the building is not considered, instead the greenfield settlement profile is evaluated. A considerable number of buildings are frequently located within the settlement trough of a tunnel in an urban area. The risk of damage to a building with a maximum slope θ of 1/500 and a settlement S_{vmax} of less than 10 mm is negligible(Rankin, 1988). By drawing ground surface contours of settlement along the route it is possible to eliminate all buildings having negligible risk. For such buildings, investigation may finish at this step. Highly sensitive buildings may be retained for the next stage of assessment. If the greenfield settlement associated with a building exceeds the maximum slope and settlement, a second stage assessment has to be carried out.

1.4.5.2. Second stage assessment.

In this stage of risk assessment, the building façade is represented by a simple elastic beam whose foundation follow the greenfield settlement profile caused by tunnelling or excavation. In this greenfield condition, the part of the settlement trough beneath the building is utilised to compute the deflection ratios DR^{GF} (both sagging and hogging) and the maximum horizontal strains ϵ_h^{GF} (both compressive and tensile). The appropriate category of damage is then obtained from Figure 1.25.

Despite being far more detailed than the preliminary assessment, this method is nonetheless conservative in that it ignores the building's stiffness. Sometimes the approach of Potts and Addenbrooke is included at this stage (as illustrated in Figure 1.30) considering soil structure interaction to reduce the number of buildings for which a detailed evaluation has to be carried out. For building damage categories which exceed category 2 (i.e. damage potentially affects serviceability) a detailed evaluation must be carried out.

1.4.5.3. Detailed evaluation (final phase).

Buildings that are still considered to be at risk of category 3 or higher damage are subjected to a detail evaluation. Also, any buildings with a high level of sensitivity are included. In this stage details of the building, tunnel construction process, structural continuity, foundations, building orientation, previous movements and existing cracking should be considered. Following a detail evaluation, which usually results in a lower category of damage than obtained from stage 2, it is necessary to decide whether preventative measures are required. Protective measures will only be necessary for buildings that remain in damage category 3 or higher. The interaction between soil and structure is important because the stiffness of the structure is likely to limit deformation.

The incorporation of the relative stiffness approach into the three-stage risk assessment approach is illustrated in the flow diagram in Figure 1.30 below.

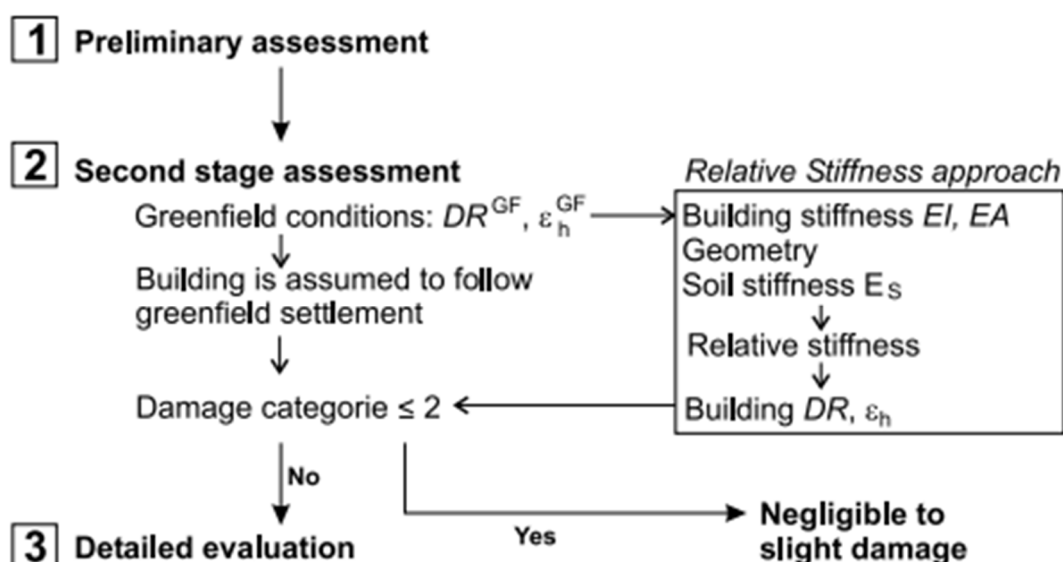


Figure 1.30. Schematic diagram of the relative stiffness approach within the three-stage risk assessment(Franzius, 2003).

Conclusion.

This chapter presented a review of empirical and numerical methods adopted in predicting tunnelling induced ground movements in greenfield conditions. It was seen that transverse surface settlement trough can be well described by a Gaussian curve. The building damage induced by tunnelling was also presented and it can be concluded that incorporating soil structure interaction into the assessment of potential building damage, reduces the expected category of damage obtained by using the highly conservative greenfield situation.

CHAPTER 2. METHODOLOGY.

Introduction.

In this chapter, the method used to realize the research work will be discussed. The greenfield analysis is a preliminary step for the study of the soil tunnel structure interaction. This chapter presents an overview of the finite element method and demonstrates the finite element modelling and excavation simulation procedure of the tunnel in greenfield conditions. The behaviour of the model together with the hypotheses are well defined. This chapter also presents the numerical modelling of a reinforced concrete frame structure used to study tunnelling structure interaction.

2.1. Site recognition

The site recognition is carried out from a documentary research whose essential goal is to know the location of the site and its geological condition.

2.2. Data collection

The data necessary for this project are the geometrical, geotechnical data and the data concerning the structural materials. The Geometrical data gives information about the tunnel geometry (length, width and height). The geotechnical parameters of the ground gotten from in-situ and laboratory tests is obtained from publications.

2.3. The finite element method

The Finite Element Method was developed during the 1960s as a method of stress analysis in the design of aircrafts. It is receiving much attention in engineering due to its flexibility and diversity. The method is based on the idea of discretisation of the geometry of a problem into several smaller parts called elements and by expressing the unknowable field variables in terms of each element's interpolating or shape functions, which are believed to be approximation functions(Bhavikatti, 2005). The shape functions are defined in terms of field variables of specified points called nodes or nodal points (selected finite points at which basic unknowns e.g. displacements are to be determined in the finite element analysis). The finite element method involves the following steps:

2.3.1. Element discretization (Meshing)

The problem domain is subdivided into several small regions called finite elements. These elements have nodes that are specified on their edges or inside of them. Based on the

shapes, they are one dimensional(1D), two dimensional(2D), three-dimensional(3D) and axisymmetric types of elements.

1D elements or line elements are suitable for the analysis of one-dimensional problem. These elements include bar and beam elements. Bar elements are suitable for modelling trusses because their load bearing capabilities are limited in the axial directions while beam elements are suitable for modelling frames because they can resist bending, twisting, as well as axial forces(Sun, 2022).

Two dimensional problems are solved using 2D elements. The most common 2D problems in stress analysis are plane stress, plane strain and shell problems. 2D elements can include triangular, rectangular and quadrilateral elements, each with varying number of nodes. The most commonly used is the three-node triangular element.

Similar to the triangle for two dimensional problems, tetrahedron having 4 nodes, one at each corner is the basic element for three dimensional problems. Other elements include: the five-node pyramid (pentahedral element), 8 node rectangular solid element and hexahedral element. The different types of three-dimensional finite elements are represented in Figure 2.1.

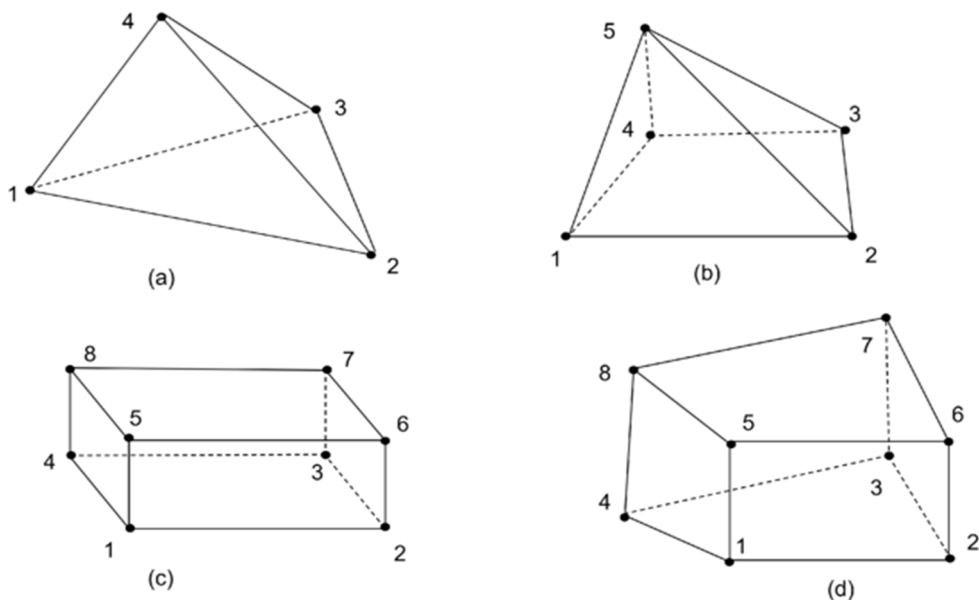


Figure 2.1. (a) 4-node Tetrahedron element, (b) 5-Node Pyramid element, (c) 8-Node Rectangular solid element, (c) 8-Node Hexahedral isoparametric element.

2.3.2. Primary variable approximation

It is necessary to choose a primary variable (such as displacements, stresses, etc.) and create criteria for how it should vary over a finite element. In geotechnical engineering,

displacement is typically the main variable used in the FE formulation. The variation of displacement over each element is expressed in terms of nodal values using shape functions.

2.3.3. Element equations formulation

Using the appropriate principle, for example the principle of minimum potential energy, the element equations can be derived as in Equation 2.1.

$$[K_E]\{\Delta u_E\} = \{R_E\} \quad (2.1)$$

Where, $[K_E]$ is element stiffness matrix, $\{\Delta u_E\}$ the nodal displacements of element nodes, and $\{R_E\}$ is the load vector. $[K_E]$ is formed by integrating the product $B^T D B$, where B is the strain displacement matrix obtained by differentiating the shape functions. D is the constitutive matrix.

2.3.4. global equations formulation and boundary conditions

The element equations are combined using the direct stiffness assembly method to form the global equations, which can be expressed as in Equation 2.2:

$$[K_G]\{\Delta u_G\} = \{R_G\} \quad (2.2)$$

where, subscript G indicates the corresponding global component.

Boundary conditions are formulated to modify the global equations. Prescribed nodal forces are included in $\{R_G\}$ while prescribed nodal displacements are included in $\{\Delta u_G\}$.

2.3.5. Solution of global equations.

The simultaneous equations that make up the global equations are complex. To acquire the displacements at each node, they are solved. Secondary quantities, including strains and stresses, are evaluated from these nodal displacements using Equations 2.3 and 2.4 respectively(M. Potts & Zdravkovic, 1999).

$$\{\Delta \varepsilon\} = [B]\{\Delta u\}_n \quad (2.3)$$

where, $\{\Delta \varepsilon\}$ is the strain vector and $\{\Delta u\}_n$ contains the nodal displacements for a single element.

$$\{\Delta \sigma\} = [D]\{\Delta \varepsilon\}, \quad (2.4)$$

where, $\{\Delta \sigma\}$ is the stress vector.

2.4. Finite element simulation of tunnel construction in greenfield conditions

The finite element simulations presented in this thesis were performed by means of the finite element software MIDAS GTS NX which is a finite element analysis software for advanced geotechnical analysis of soil and rock deformation and stability, as well as groundwater flow, dynamic vibrations and soil-structure interaction in 2D and 3D. GTS NX is used for analysis, testing, and design by geotechnical, civil, and mining engineers. The software enables the design and modelling of various materials and can simulate interactions between various elements and parts. The software provides a variety of element types and meshing options. With different constitutive laws, different material behaviour can be simulated. Furthermore, the software carries out a complete analysis in three stages: pre-processing or modelling, which involves the creation of an input file, processing (FE analysis), and post-processing, which provides reports, images, and animations.

2.4.1. Three-dimensional finite element model

It is crucial to consider partial stress relief, or deformations of the excavation surface at the tunnel working face, which happened prior to the installation of the lining, for an adequate evaluation of stress-strain states in the tunnel lining and soil. This can be achieved using three-dimensional finite element modelling which simulates the progress of tunnel construction and stress-strain changes that take place at the temporary working face.

2.4.1.1. Soil behaviour (soil constitutive model)

Midas GTX NX provides a variety of soil models to simulate the ground deformations. Among these models is the Mohr-Coulomb Model (MC) and the Hardening Soil (small strain stiffness) model [HS-Small Model] which will be used in the project in this thesis. The soil behaviour can be drained if no excess pore water pressure is formed and undrained behaviour if there is excess pore water pressure.

a. Mohr-Coulomb constitutive model

The Mohr-Coulomb model is defined by a linear elastic-perfectly plastic behaviour. This behavioural assumption shows reliable results for general nonlinear analysis of the ground and is widely used in simulating most terrain. The linear elasto-plastic behaviour is represented in Figure 2.2 below, where ε^e and ε^p represent the elastic and plastic strain respectively.

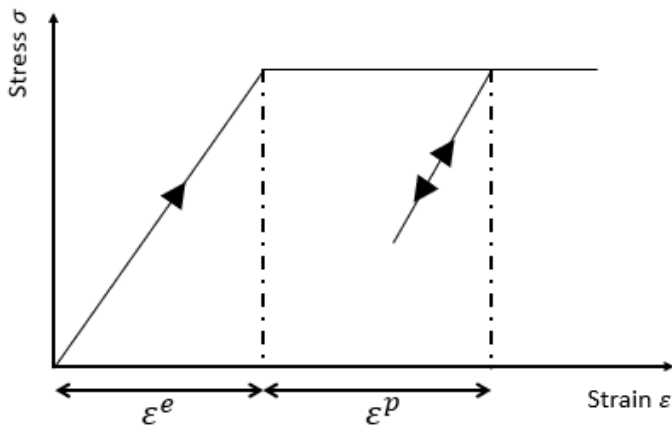


Figure 2.2. Stress-strain relationship for linear elastic-perfectly plastic behaviour.

This criterion is accurate within a limited range of confining pressure but as the range difference increases, the accuracy decreases. The major nonlinear parameters used to define the Mohr-Coulomb yield criterion are as follows:

i. Cohesion (C), Friction angle (φ)

Soils have different cohesion and friction angle depending on their type and these values are applied to the shear strength equation. According to Coulomb, the shear strength of soil can be expressed as shown in Equation 2.5.

$$\tau = c + \sigma \tan \varphi \quad (2.5)$$

Where, τ is the shear strength of soil, σ is the normal stress and φ is the internal friction angle.

Cohesion is the shear strength when the interior friction angle is zero according to the yield criterion. It can be defined as an undrained shear strength of cohesive soils. Sandy soils with no cohesion can be defined as cohesion equal to zero.

ii. Dilatancy angle (ψ)

The dilatancy angle can be viewed as the volume increase rate according to shear strain. It is a type of strength parameter for roughness and is generally defined as dilatancy angle equal to interior friction angle minus 30°. If the interior friction angle is less than 30°, the dilatancy angle is close to '0(zero)'. In real tests, a negative dilatancy angle can be defined for very loose sandy soil but numerically, the dilatancy angle has a value between 0 and the interior friction angle.

b. Hardening soil (small strain stiffness) model [HS-Small Model].

The Hardening Soil model is an improvement on the Mohr-Coulomb model, generated by combining nonlinear elastic models and elasto-plastic models to make a suitable model for the behavioural characteristics of silt or sand-based ground. The model can simulate the Double stiffening behaviour, which is not affected by the shear failure or compressive yield. Shear hardening and compression hardening are the two basic types of hardening that can be distinguished.

The Hardening Soil with small strain stiffness model is implemented by using the Hardening soil model and Small strain overlay model, and needs two additional parameters (initial small-strain shear modulus and the shear strain at which the shear modulus is about 70% of the initial small-strain shear modulus). With increasing strain, soil stiffness decreases nonlinearly. The hardening soil-small model considers the small strain stiffness of soil, i.e. the high stiffness of soil at very small strain. The basic input parameters for the Hardening Soil (soil strain stiffness) model are summarised in Table 2.1.

Table 2.1. Summary of parameters for the Hardening Soil (soil strain stiffness) model.

Parameter	unit	Description
E_{ur}^{ref}	[MPa]	Triaxial unloading/reloading stiffness
E_{50}^{ref}	[MPa]	Triaxial loading stiffness
E_{Oed}^{ref}	[MPa]	Oedometer loading stiffness
m	[-]	Power for stress level dependency of stiffness
c'	[MPa]	Effective cohesion
ϕ'	[°]	Effective friction angle
ν_{ur}	[-]	Poisson's ratio for unloading/reloading
K_O	[-]	Coefficient of earth pressure
G_O^{ref}	[MPa]	Shear modulus at small strain
$\gamma_{0.7}$	[%]	Shear strain at which shear modulus has decayed to 70% of initial shear stiffness (G_O^{ref})

The different stiffnesses (the triaxial unloading stiffness E_{ur}^{ref} , triaxial loading stiffness E_{50}^{ref} and the oedometer loading stiffness E_{Oed}^{ref}) are related by $E_{ur}^{ref} = 3E_{Oed}^{ref}$ and $E_{Oed}^{ref} = E_{50}^{ref}$, as recommended by the MIDAS GTS NX manual 2019.

2.4.1.2. Behaviour of structural members

The main supporting system in the New Austrian Tunneling Method (NATM) are shotcrete and rock bolts with measurement of deformations in the tunnel to evaluate whether it is stable or not. The isotropic linear elastic constitutive model is adopted for the shotcrete lining and the rock bolts. In the linear elastic model, the stress is directly proportional to strain. The proportionality constants are the Elasticity modulus (E) and Poisson's ratio (ν). In this linear elastic model, the yield value is not defined, so the calculated stress and strain can be highly unrealistic. However, this model is appropriate in modelling concrete or structural steel structures, which have a much higher strength than the ground. The linear stress-strain behaviour is shown in Figure 2.3.

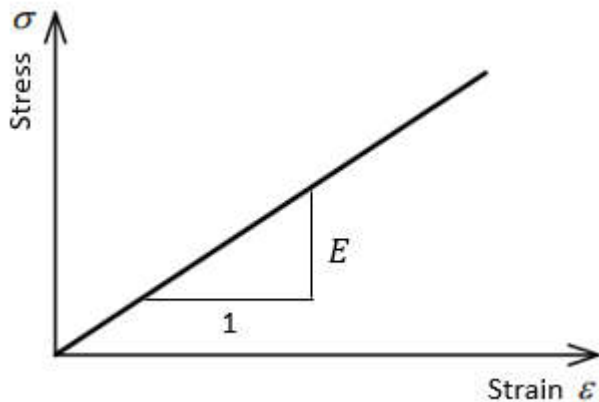


Figure 2.3. Linear elastic stress-strain relationship.

2.4.1.3. Finite element mesh generation

After the geometry of the problem is created, it is necessary to discretize the geometry. GTS NX provides a variety of 1D, 2D and 3D finite elements. It also provides options to control the size of the elements in the model, for example, by defining edge or global seeds to restrict the element size at areas of stress concentration. The different element types used for the soil and the structural members of the tunnel in this study are listed in Table 2.2 below.

Table 2.2. Element types used for mesh generation of the model.

	Geometry	Element type
Soil Layers	3D	Tetrahedron element
Shotcrete	2D	Triangular shell element
Rock Bolt	1D	Embedded truss element

2.4.1.4. Boundary conditions

The 3D mesh block used to carry out the finite element simulation of the tunnel construction was 90 m long, 120 m wide and 28 m in height. The size of the model was chosen so that the boundaries are sufficiently far from the tunnel to minimize the effect of boundary conditions on the results, that is, where there is nearly no change in stress or displacement due to the tunnel construction. The bottom boundary of the model is constrained in both the horizontal and vertical directions, while vertical side boundaries are fixed only in the horizontal direction. No degrees of freedom are constrained for the top boundary (ground surface).

2.4.2. Tunnel installation simulation method

Construction stage analysis can be used to simulate the construction process. Construction stage analysis consists of multiple stages and loading/boundary conditions, as well as elements, can be added or removed at each stage. This loading/boundary or element change is applied at the start of each stage. During construction step analysis, the ground material properties can change to model time dependent ground disturbance, soil improvement or hardening. There are also cases where the structural material properties need to be changed in the middle of the stage, such as hardening of concrete lining (shotcrete) or changes in lining thickness.

The 3D FEM simulation of the excavation of the Horse shoe shaped top heading is done using the step by step simulation procedure for conventional tunnelling described in section 1.3.2.2. The simulation phases are carried out in drained conditions starting from an in-situ stage concerned with determining the initial geostatic stresses. These initial stresses are calculated using the K_O procedure. The K_O method computes the horizontal stress σ_h from the vertical stress σ_v and sets it as the in-situ stress using the constant K_O defined by Equation 2.6:

$$K_O = \sigma_h / \sigma_v \quad (2.6)$$

In order to calculate the horizontal stress using this method, the vertical stress must first be determined using self-weight analysis. In this case, the shear stress maintains the value determined by the analysis's results (*MIDAS GTS NX User Manual*, 2019). At the end of this in-situ stage, the displacement reset condition is used to reset the in-situ displacements and strains due to the self-weight to zero, since only the displacements due to the tunnel construction are of interest.

The excavation of the tunnel heading is carried out full face with an unsupported round length of 1.2m. Using the step by step excavation simulation, a strip of soil elements is deactivated in

each excavation stage, while at the same time the rock bolts and a segment of shotcrete elements are activated to support the preceding excavation stage as shown in Figure 2.4.

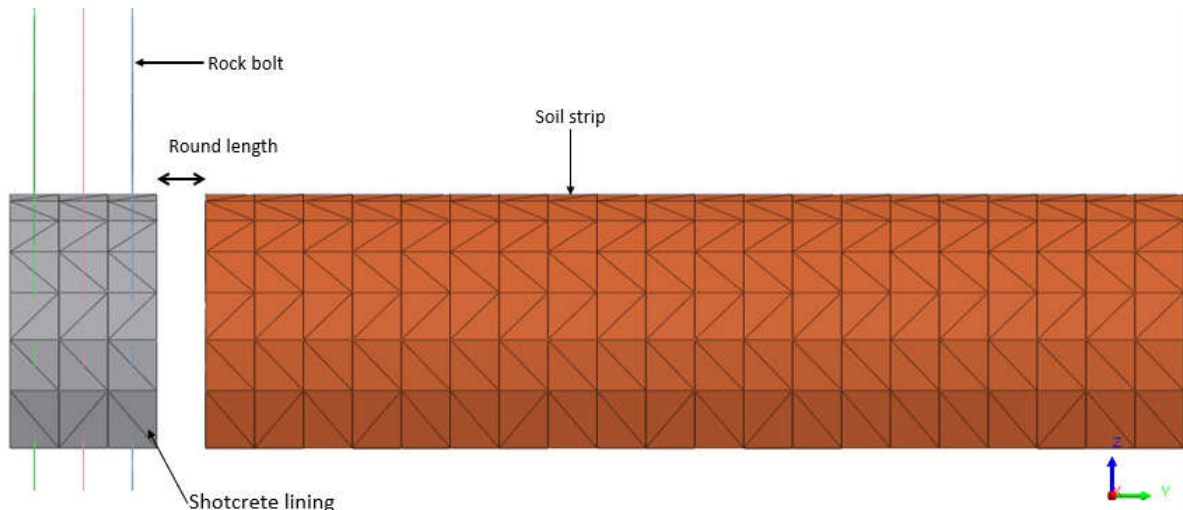


Figure 2.4. Third excavation stage plus shotcrete and rock bolt installation in the preceding excavation.

To account for the hardening of the lining, the stiffness was increased stepwise, using a different Young's Modulus for soft and hardened shotcrete. Young's modulus for soft shotcrete was used for the first three lining rings behind the tunnel face and the older shotcretes were considered hardened.

The construction stages can be summarised as follows:

- Stage 1: Initial stress state determination
- Stage 2: 1st tunnel face excavation
- Stage 3: 1st reinforcement (shotcrete lining and rock bolts) + 2nd face excavation
- Stage 4: 2nd reinforcement + 3rd face excavation
- Stage 5: 3rd reinforcement + 4th face excavation
-
- Stage N: (N-2)th reinforcement + (N-1)th face excavation.

2.4.3. Validation of the 3D finite element model

The 3D finite element model of the tunnel built is analysed for a normally consolidated and also for an over consolidated soil layers with over consolidation ratio (OCR) of 2. To validate the accuracy of the numerical model in predicting realistic tunnelling-induced deformations, the computed settlements are compared with the available measured data and with available numerical results obtained by other authors in greenfield analysis. This validated

numerical model is therefore used in the next section for the coupled soil structure interaction analysis.

2.5. Simulation of coupled soil structure interaction

A detailed three-dimensional model of the superstructure is created and coupled with the soil and tunnel to carry out the tunnelling superstructure interaction analysis. The model of the reinforced concrete frame of the building is carried out using MIDAS GEN, a structural program for the analysis of buildings and structures. The good integration between MIDAS Gen and MIDAS GTS NX facilitates the importation of the structure into GTS NX.

2.5.1. Loads

Permanent loads and Variable loads would be considered:

2.5.1.1. Permanent loads (G)

They are also referred to as dead loads. These are those actions that do not change over time or for which their variation in magnitude with time is negligible, for example, self-weight

2.5.1.2. Variable loads (Q)

They can also be referred to as live loads. These actions can change over time, for example, imposed floor loads, furniture loads, snow and wind loads. In this study, only imposed loads would be used. The values of imposed loads are defined in Eurocode EN 1991-1-1:2002 according to the building category as shown in appendix A.

2.5.2. Load combination

The serviceability limit state combination presented in Equation 2.7 would be used for this analysis.

$$\sum_{j \geq 1} G_{K,j} + Q_{K,1} + \sum_{i \geq 1} \varphi_{0,i} Q_{k,i} \quad (2.7)$$

Where, $G_{K,j}$ Characteristic value of permanent action j

$Q_{K,1}$ Characteristic value of the leading variable action 1

$Q_{k,i}$ Characteristic value of the accompanying variable action i

2.5.3. Numerical modelling of superstructure

The superstructure considered is a reinforced concrete multi storey building. A Three-dimensional model of the superstructure is built using structural beam elements to model the beams and columns (with the beam to column connections considered rigid), and plate elements to model the shear walls. The floors are modelled as rigid diaphragms. Permanent and imposed loads are applied to the structure, with only floor loads considered for this analysis.

The raft foundation is modelled as plate elements supported on linear Winkler springs. The modulus of subgrade reaction or Winkler spring constant K is obtained by modelling the loaded foundation in MIDAS GTS NX, after which the results of settlements are exported to MS Excel to calculate linear springs constant K as defined by Equation 2.8.

$$K = \frac{\text{Pressure or Reaction}}{\text{Settlement}} \quad (2.8)$$

The linear spring stiffnesses are applied to the raft foundation (plate element) in MIDAS GEN to obtain the structural response of the building in ordinary conditions.

2.5.4. Coupled soil structure modelling

The well validated Finite element model obtained from section 2.4.3 is coupled with the numerical model of the building to study the interaction between the tunnel construction process and the reinforced concrete framed building. As common features, the same model dimensions and boundary conditions that were adopted for the greenfield analysis case are also adopted in the coupled soil structure interaction case. The analysis is also carried out in drained conditions.

The simulation of the tunnel excavation process follows the same procedure presented in section 2.4.2. Following the in-situ stage, a subsequent construction stage is introduced that involves the activation of the structure mesh set, raft, and structural static loads before the excavation begins. Two analysis are carried out which are given as follows:

- Construction stage analysis in which the displacements due to the structure loads and tunnel construction are studied, and
- Construction stage analysis, where only the displacements caused by the tunnel construction are of interest, that is, displacements cleared after the activation of the building and its loads.

2.6. Building damage evaluation

An appropriate building damage criterion is chosen to evaluate the potential level of damage to the building.

2.6.1. Choice of appropriate damage criteria

Both the damage criteria proposed by Burland et al. (1977) and Boscardin & Cording (1989) are the most commonly used and their selection is based on the convenience to obtain the relevant parameters. It is not always easy to identify the tilt which makes the evaluation of angular distortion difficult. For this reason, the damage criterion proposed by Burland et al. (1977) would be adopted in this study since it only uses deflection ratio as a measure of building deformation.

2.6.2. Damage interaction diagram

The parts of the building under sagging and hogging are treated as separated segments by calculating the respective deflection ratio (Δ/L) and horizontal strain (ϵ_h). The interaction diagram is plotted for both sagging and hogging.

2.6.2.1. Interaction diagram for sagging

For a building undergoing Sagging, the neutral axis is assumed to be at the middle. For the structure's Poisson's ratio of $\nu = 0.2$, the bending strain limit and the shearing strain limit for sagging are given by the formulated Equation 2.9 and Equation 2.10 respectively.

$$\frac{(\Delta/L)}{\varepsilon_{lim}} = \left(0.167 \frac{L}{H} + 0.6 \frac{H}{L} \right) \left(1 - \frac{\varepsilon_h}{\varepsilon_{lim}} \right) \quad (2.9)$$

$$\frac{(\Delta/L)}{\varepsilon_{lim}} = (1 + 0.278 \left(\frac{L}{H} \right)^2) \cdot \sqrt{\left(1 + \frac{\nu \varepsilon_h}{\varepsilon_{lim}} \right) \left(1 - \frac{\varepsilon_h}{\varepsilon_{lim}} \right)} \quad (2.10)$$

Where, Δ/L = Deflection ratio

ε_{lim} = Limiting strain

ε_h = horizontal strain

ν = Poisson's ratio

L = Width of building transverse to tunnel axis.

H = Height of building

The limiting combination is gotten by taking the maximum of either the bending or shearing strain. By adopting the values of ε_{lim} associated with the various categories of damage given in Table 1.2 and by using Equations 2.9 and 2.10, the building damage interaction diagram is developed showing the relationship between deflection ratio and horizontal strain.

2.6.2.2. Interaction Diagram for Hogging.

The damage interaction diagram for hogging is obtained assuming the neutral axis of the building to be at the bottom edge. The bending strain limit and the shearing strain limit for hogging are given by the formulated Equation 2.11 and Equation 2.12 respectively.

$$\frac{(\Delta/L)}{\varepsilon_{lim}} = \left(0.083 \frac{L}{H} + 1.3 \frac{H}{L} \right) \left(1 - \frac{\varepsilon_h}{\varepsilon_{lim}} \right) \quad (2.11)$$

$$\frac{(\Delta/L)}{\varepsilon_{lim}} = (1 + 0.064 \left(\frac{L}{H} \right)^2) \cdot \sqrt{\left(1 + \frac{v\varepsilon_h}{\varepsilon_{lim}} \right) \left(1 - \frac{\varepsilon_h}{\varepsilon_{lim}} \right)} \quad (2.12)$$

In the same way as in the case of sagging, the damage interaction diagram is also developed using Equations 2.11 and 2.12 to relate deflection ratio and horizontal strain to the categories of damage.

Conclusion.

The objective of this chapter was to present the procedure necessary to carry out the tunnelling superstructure interaction analysis. It started with a site recognition and collection of data. After which the methodology adopted for the 3D FEM simulation of the tunnel in greenfield conditions using MIDAS GTS software was presented. The excavation was carried out using the step by step approach, with the top heading excavated full face and a lining ring installed with a delay step. The numerical model was validated against available field measurements with particular reference to settlements. The model which gave a good agreement with measured data was then used to carry out a coupled soil structure interaction analysis to study the effects of tunnel advancement on the structure. In the end, the criteria used to evaluate the building damage was discuss

CHAPTER 3. RESULTS INTERPRETATION AND DISCUSSIONS.

Introduction.

This chapter presents the project information and the analysis results of the verified three-dimensional finite element model in the greenfield and coupled soil structure interaction cases described in the previous chapter. The results are then further interpreted and discussed. The influence of the superstructure on the tunnel induced settlements and strains are studied by comparing the surface settlement profiles and horizontal strains induced by the tunnel in greenfield conditions with the case of the fully coupled model. Deformations and stresses in the shotcrete lining are also analysed. Additionally, the sensitivity of the building to tunnelling effects is examined by investigating the displacements, internal forces and moments of its structural elements. Finally, based on the results of the deformation and horizontal strains induced on the building in the coupled interaction analysis, the expected level of building damage is evaluated.

3.1. Site Description

The description of the study area shall be done through the geographical location and the geology.

3.1.1. Location

The Steinhaldenfeld tunnel is located in the North eastern part of the city of Stuttgart, Germany. The tunnel construction was started in April 2002, for the extension of the city's subway system. It was finished in late 2004 and formally opened in the beginning of 2005. Figure 3.1 presents a satellite map showing the location of the Steinhaldenfeld tunnel with the route of the tunnel indicated with a red line.



Figure 3.1. Satellite map showing the location and the course route (red line) of the Steinhaldenfeld tunnel.

The construction of this tunnel was carried out between the old station Hauptfriedhof and the new station Steinhaldenfeld, with two cut and cover sections, each 110m long at the tunnel portals, and a section constructed using the New Austrian Tunneling Method(NATM) of 940m long in between(Möller, 2006). The entire length of the tunnel is 1090 m. Figure 3.2 shows a site plan of the Steinhaldenfeld tunnel.

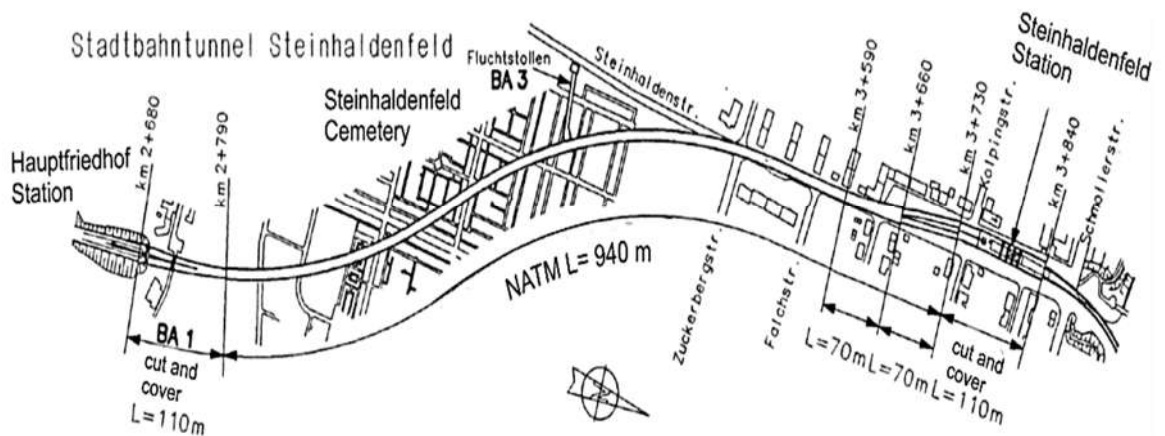


Figure 3.2. Site plan of the Steinhaldenfeld Tunnel(Möller, 2006)

3.1.2. Geological Condition

The longitudinal geological profile of the Steinhaldenfeld tunnel is shown in Figure 3.3.

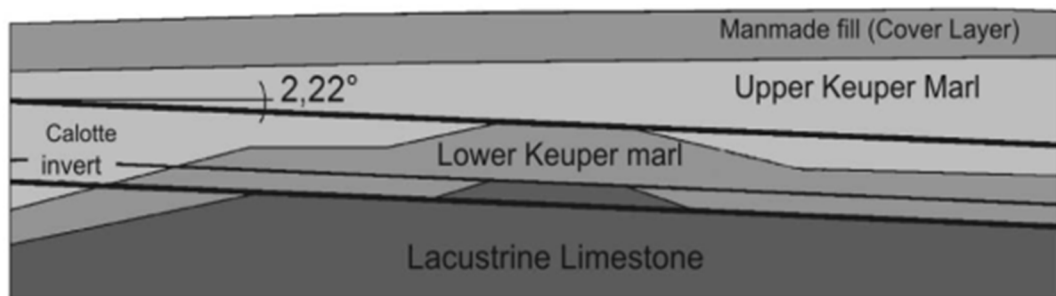


Figure 3.3. Geological longitudinal profile of Steinhaldenfeld tunnel(Moayed et al., 2011).

As can be seen, there are two layers of Keuper marl underneath the top layer of man-made fill, which serves as a cover layer. This layer of Keuper marl, which is composed of extensively weathered soft rock is underlain by strong limestone. Concerning the hydrogeological condition, the construction of the tunnel was carried out above the ground water table.

3.2. Data Presentation

The main data necessary for the project is presented in this subsection.

3.2.1. Geotechnical Characterisation

The Stuttgart Keuper marl can be classified as a residual soil and as a weathered soft rock. Therefore, it is very difficult to perform measurements of initial horizontal stress; both in the case of in situ borehole measurements and laboratory tests on samples. Whereas the data that are currently available for Stuttgart Keuper marl seem to indicate that horizontal stresses are significantly higher than those of a normally consolidated soil, while K_0 near unity is also

significantly lower than those of a heavily over consolidated sedimentary clay(Möller, 2006). The Steinhaldenfeld tunnel site ground parameters of the Mohr-Coulomb model are listed in Table 3.1, while the HS-Small Model parameters are listed in Table 3.2.

Table 3.1. Steinhaldenfeld ground parameters of the MC-Model from site investigation(Möller et al., 2004).

Layer	Unit weight $\gamma [KN/m^3]$	Poisson's ratio ν	Stiffness $E [MPa]$	Cohesion $C' [MPa]$	Friction angle $\varphi' [^\circ]$	At rest coefficient K_0
Fill	20	0.37	15	0.01	25	0.57
Upper Keuper Marl	24	0.2	100	0.025	25	0.9
Lower Keuper Marl	23	0.35	60	0.025	25	0.9
Limestone	23	0.2	750	0.2	35	0.6

Table 3.2. Additional Parameters for the Hardening Soil (Small strains stiffness) Model(Möller, 2006a).

Layer	ν_{ur} [-]	E_{ur}^{ref} [MPa]	E_{Oed}^{ref} [MPa]	E_{50}^{ref} [MPa]	G_o^{ref} [MPa]	$\gamma_{0.7}$ [%]	m [-]
Fill	0.2	30	10	10	75	$2 \cdot 10^{-4}$	0.5
Upper Keuper Marl	0.2	100	33	33	250	$2 \cdot 10^{-4}$	0.4
Lower Keuper Marl	0.2	48	16	16	120	$2 \cdot 10^{-4}$	0.4
Limestone	0.2	575	190	190	1438	$2 \cdot 10^{-4}$	0.3

Where;

E_{ur}^{ref} : triaxial unloading stiffness, E_{50}^{ref} : triaxial loading stiffness, E_{Oed}^{ref} : oedometer loading stiffness, G_o^{ref} : Shear modulus at small strain, $\gamma_{0.7}$: Threshold shear strain, m : Stress level dependency of stiffness

3.2.2. Geometrical Information

The finished inner shell of the double track tunnel has a width of 8.8 m and a height of 7.23 m. In the first driving between August 2002 and May 2003, the upper part of the tunnel cross-section (tunnel heading) was excavated along the entire length of the tunnel. Subsequently, until September 2003, the bench/bottom excavation was carried out. The advance length of the tunnel was 1.2 m, with shotcrete and rock bolts being the main supporting systems. Figure 3.4 shows the cross section of the top heading with subsequent bench and base support.

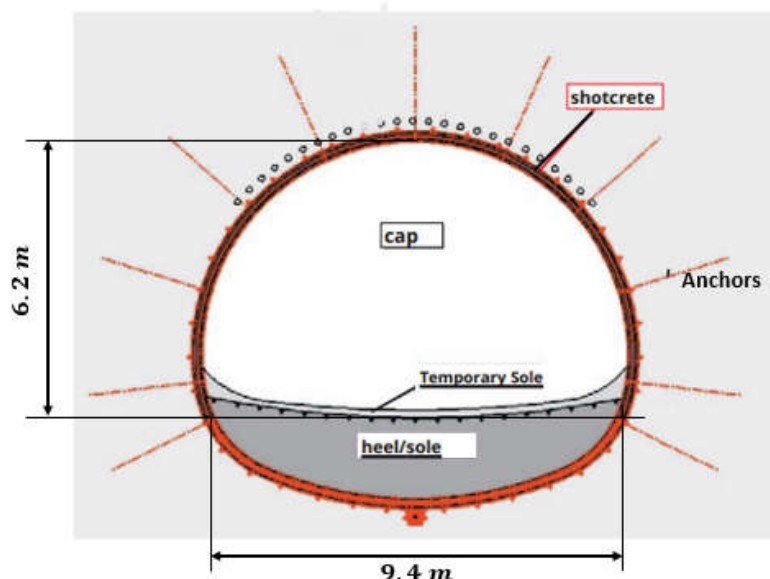


Figure 3.4. Top heading drive with subsequent bench and base support.

The top heading view of the tunnel can be seen in Figure 3.5.



Figure 3.5. Construction of the Steinhaldenfeld Tunnel(Möller et al., 2004).

3.2.3. Tunnel Support Details.

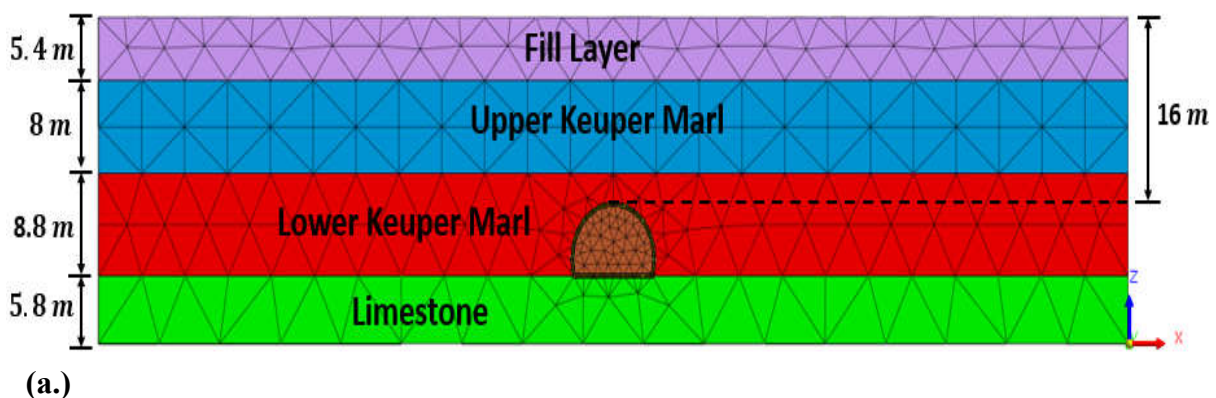
Anchors (rock bolts) were used to enhance the ground immediately surrounding the tunnel. Table 3.3 shows the properties of the rock bolt and concrete lining.

Table 3.3. Properties of shotcrete lining and rock bolts (Moayed et al., 2011; Möller, 2006b).

	Unit weight $\gamma [KN/m^3]$	Youngs Modulus $E [MPa]$	Poisson's ratio $\nu [-]$	Diameter [m]	Length [m]	Thickness [m]
Hard Shotcrete	24	15000	0.25	-	-	0.25
Soft Shotcrete	24	7500	0.25	-	-	0.25
Rock Bolts	78.5	200000	0.3	0.05	5	-

3.3. FE model of the greenfield situation

Numerous numerical models were used, and only the results of the validated numerical model are presented. The 3D mesh block used to carry out the finite element analysis was 90 m long, 120 m wide and 28 m in height. The in-situ stage of the model consists of 79727 elements and 307358 nodes. The finite element model used to simulate the tunnel construction in greenfield is shown in Figure 3.6.



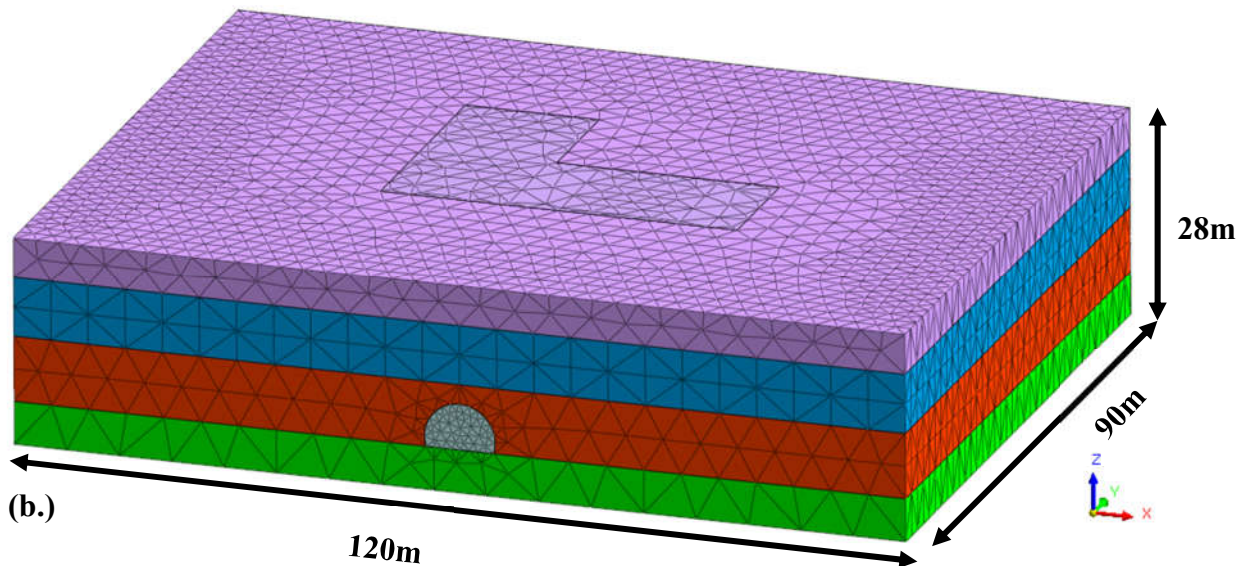


Figure 3.6. Numerical model of greenfield situation: **(a.)** Front view **(b.)** 3D view.

The ground is described using tetrahedral elements with a mesh size of 4 m and a controlled length of 1.2 m in the direction of tunnel excavation. The finite element mesh is not extended into the limestone due to its high stiffness. The Steinhaldenfeld tunnel was built above the groundwater table and therefore pore water pressure was not considered by carrying out the numerical analysis in drained conditions.

The Sprayed concrete lining (shotcrete) modelled by triangular shell elements were meshed with a size of 1.2 m . Rock bolts numerically modelled using linearly elastic embedded truss elements had a mesh size of 1 m . Figure 3.7 below shows a model of a segment shotcrete lining and rock bolts of the top heading of the tunnel.

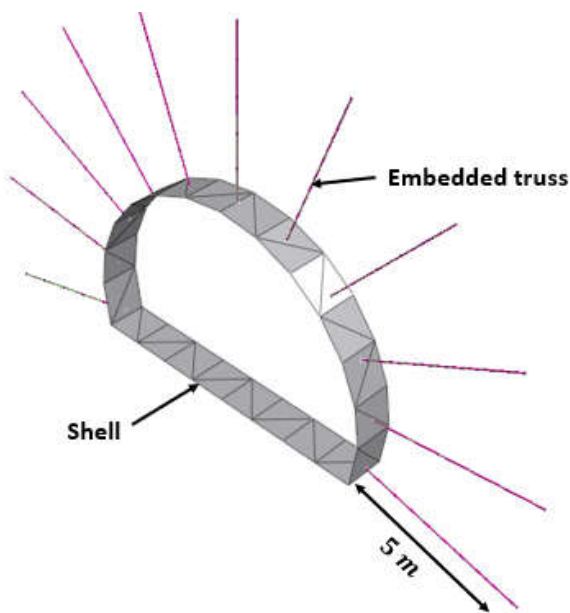


Figure 3.7. Model of a shotcrete lining segment and rock bolts of the top heading section.

3.3.1. Tunnel construction stages

A full-face excavation of the tunnel heading was done. The greenfield simulation of the tunnel construction was carried out with a total of 79 construction stages presented detailly in Appendix C. Figure 3.8 illustrates a view of the sequential excavation sequence.

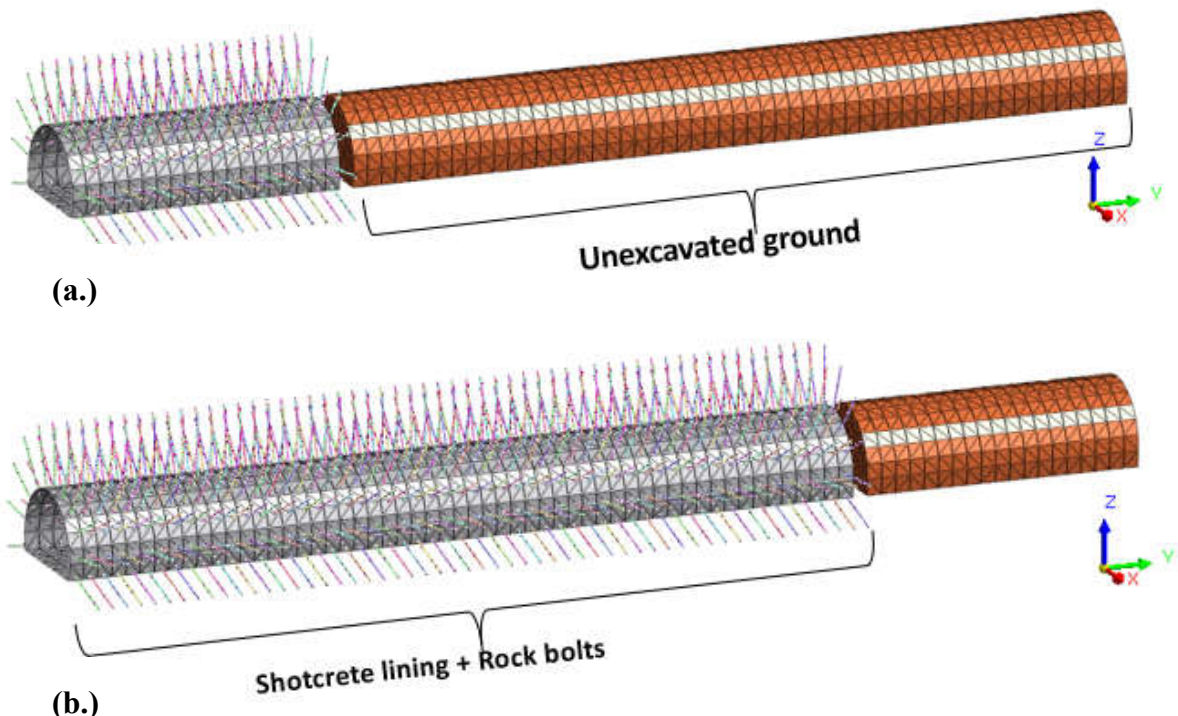


Figure 3.8. Sequential construction stages plus shotcrete and rock bolts installation in the preceding phase: (a.) Construction stage 20 (b.) Construction stage 56.

3.3.2. Finite element model validation

To validate the accuracy of the numerical model, the computed settlements were compared with the available measured data of the Steinhaldenfeld tunnel and with available numerical results obtained by Maraš-Dragojević (2021) and S. Möller (2006) who performed 2D and 3D numerical analyses respectively, numerically accounting for the rock bolts by increasing the cohesion of the zone around the tunnel where anchors were used. These comparisons are illustrated in Figures 3.9 and Figure 3.10 below.

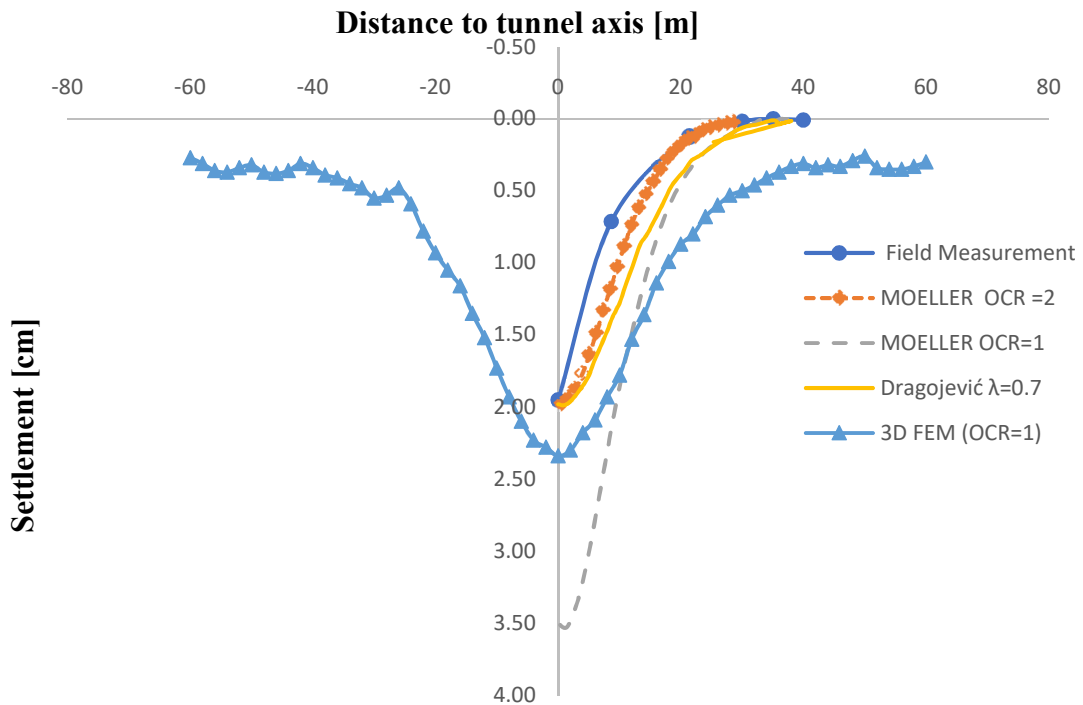


Figure 3.9. Comparison between the transverse settlement trough of normally consolidated ground ($\text{OCR}=1$) in this study with field measurements and other numerical studies.

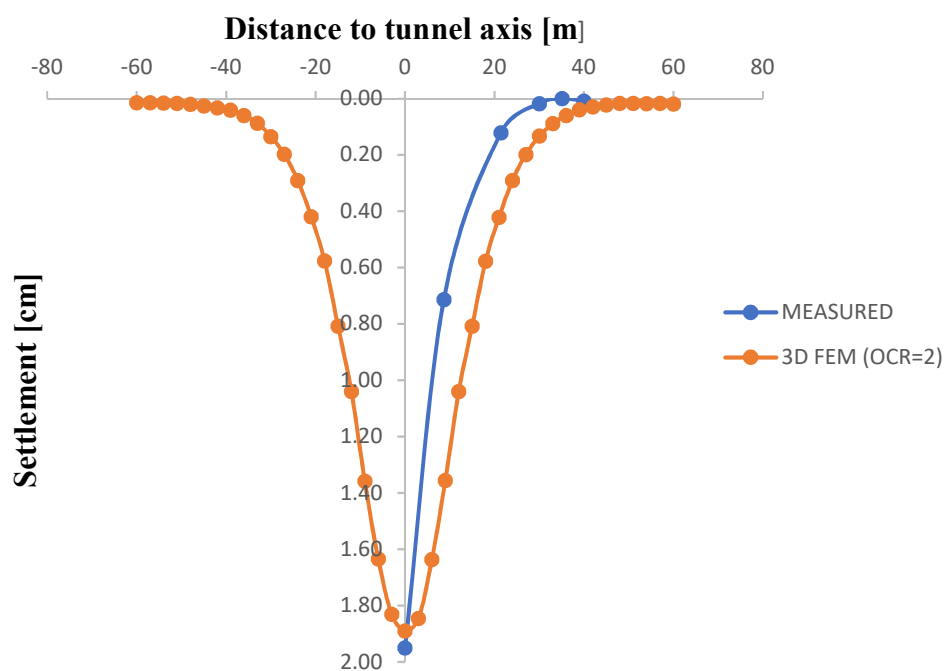


Figure 3.10. Comparison between the transverse settlement profile of an over consolidated ground in this study with field measurements.

It can be seen from these figures that the analysis with normally consolidated ground ($OCR=1$) overestimates the settlements. The results obtained with an over consolidated ground ($OCR=2$) are in good agreement with the measured data. It gives a maximum settlement of 1.90 cm as compared to the measured value of 1.95 cm .

3.4. Numerical model of the coupled soil structure interaction

The well validated numerical model of the greenfield situation is coupled with the model of the superstructure.

3.4.1. Numerical model of superstructure

The superstructure considered is a conceived 10-storey reinforced concrete L-shape building with unequal bays.

3.4.1.1. Material properties

The main characteristics of the concrete used are presented in Table 3.4 below.

Table 3.4. Mechanical properties of the reinforced concrete.

Parameter	Unit	Value
Characteristic compressive strength f_{ck}	MPa	25
Youngs modulus E	MPa	31500
Poisson's ratio ν	-	0.2
Unit weight γ	KN/m ³	25

3.4.1.2. Geometry of structural model

The geometrical properties of the elements are listed in Table 3.5.

Table 3.5. Geometrical properties of the reinforced concrete elements.

Parameter	Unit	Value
Beams cross section $B \times H$	cm ²	40×50
Columns cross section $B \times H$	cm ²	40×40
Shear wall thickness	cm	30
Raft thickness	cm	100

The first floor to the fifth floor has the same structural plan, while the structural plans of the sixth floor to the roof are also identical. The floors are considered to be two-way slabs. These structural floor plans are shown below in Figure 3.11 and Figure 3.12.

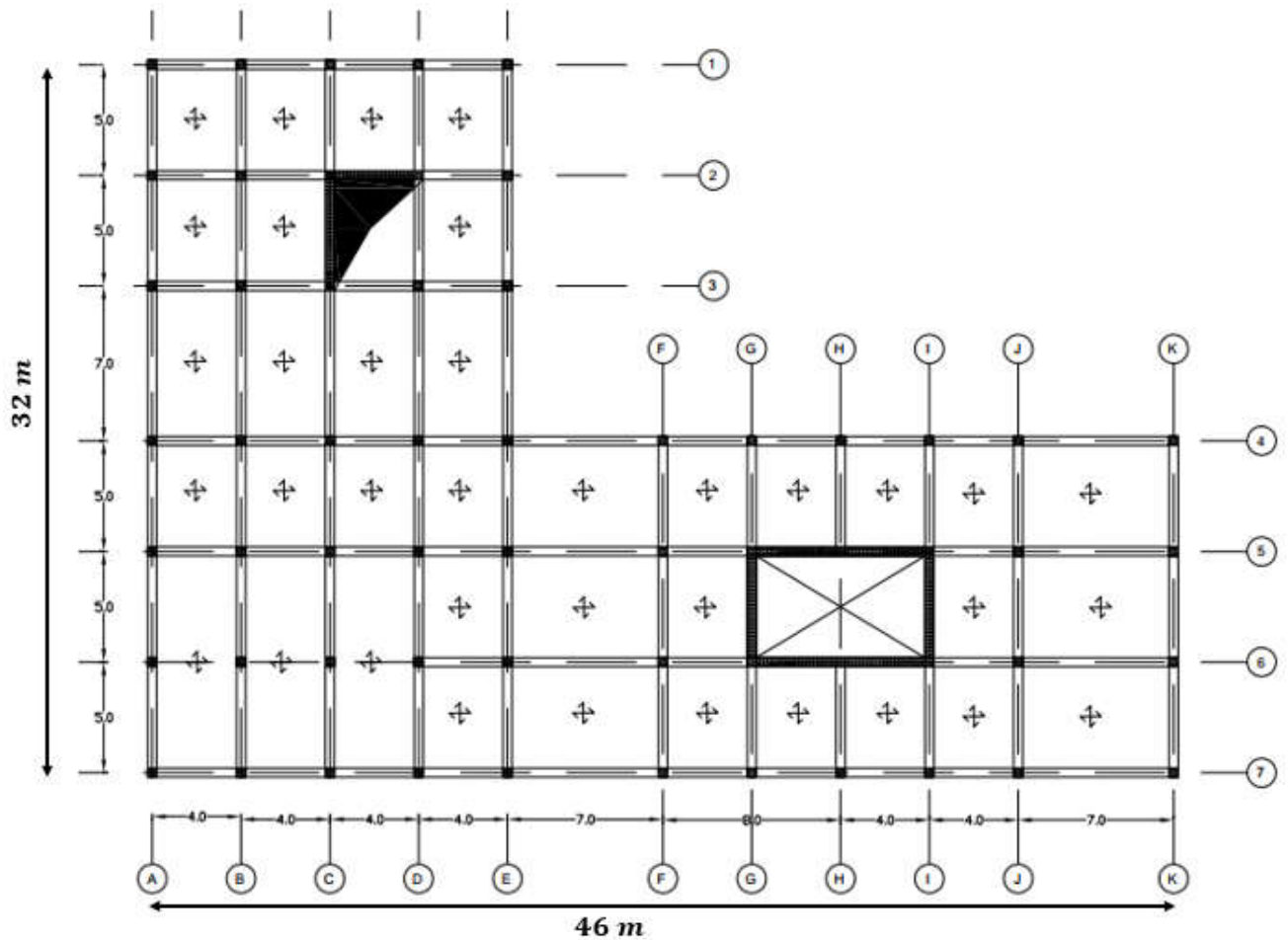


Figure 3.11. Structural plan of first floor to fifth floor.

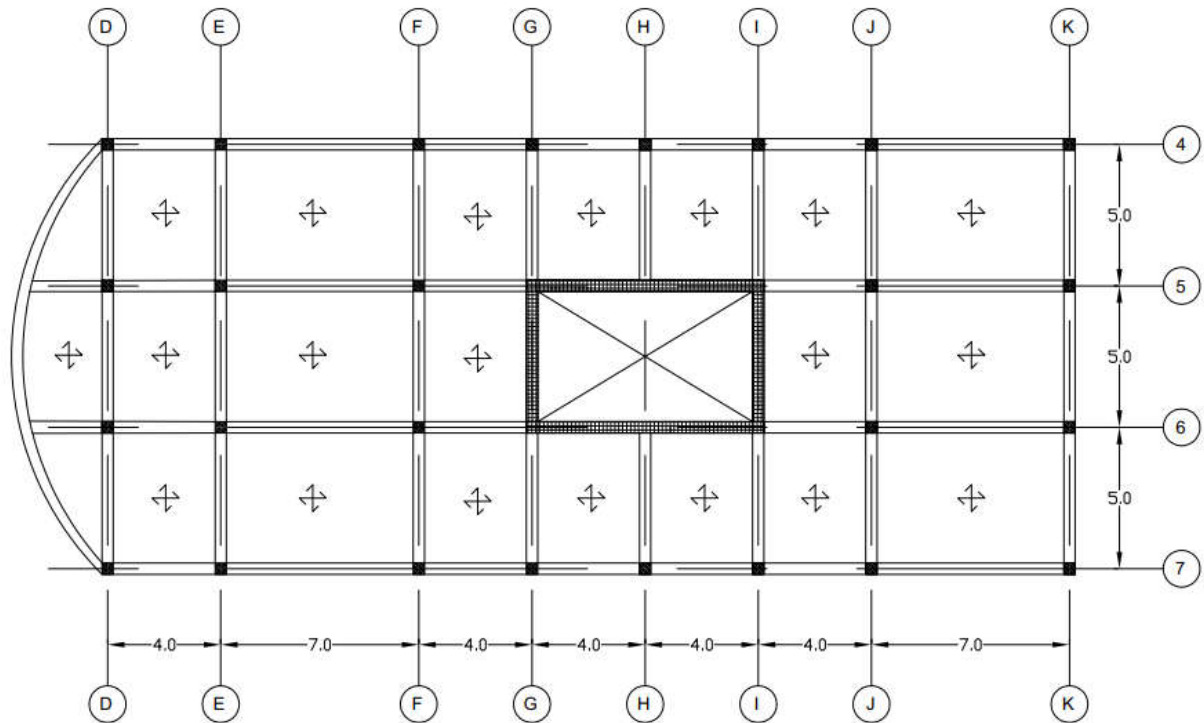


Figure 3.12. Structural plan of sixth floor to the roof.

The building has an inter-storey height of 3.2 m from the ground floor to the 6th floor and an inter-storey height of 3 m from the 6th floor to the roof. Figure 3.13 shows the front elevation of the building.

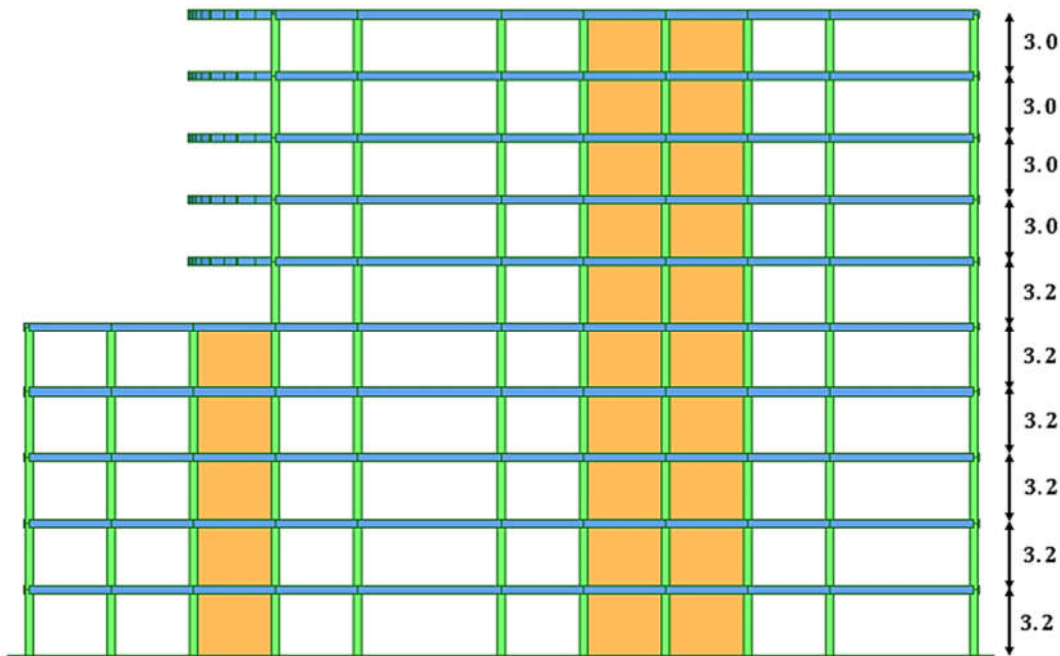


Figure 3.13. Front elevation of building.

Presented in Figure 3.14 is a 3D model of the structure.

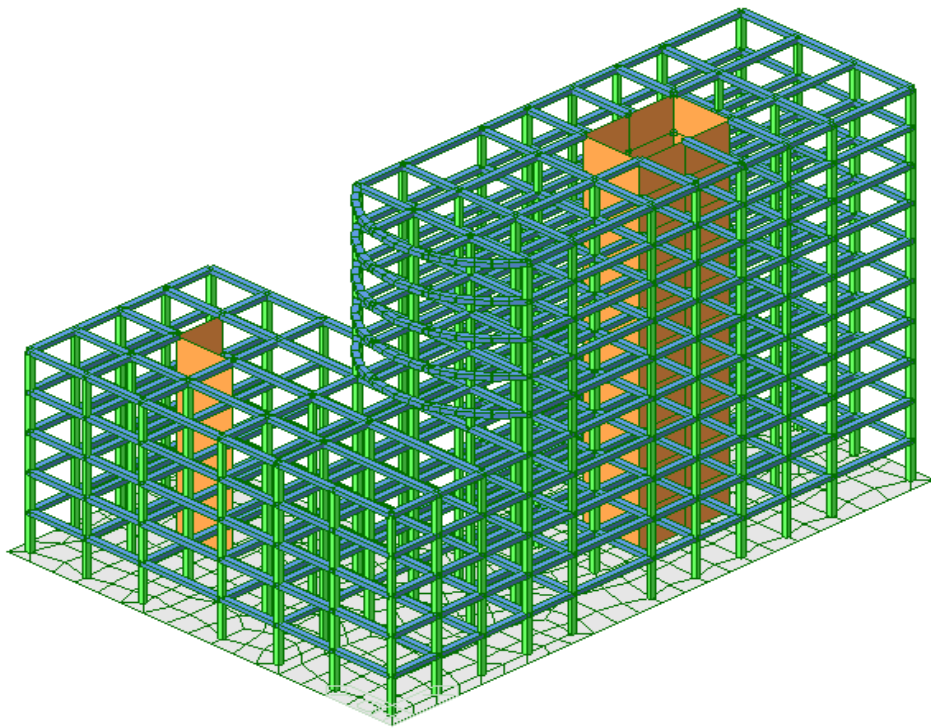


Figure 3.14. Finite element model of 3D structure.

3.4.1.3. Applied loads

The Building is assumed to be a residential building of Category A. Therefore, the imposed floor loads are obtained from Table 6.2 of EN 1991-1-1:2002 (presented in Appendix A). Only area (pressure) loads are considered in this analysis. The imposed load on the roof is obtained from Table 6.10 of EN 1991-1-1:2002. Table 2.5 presents the loads acting on the building.

Table 3.6. Characteristic value of loads acting on building.

Load	Floor	Roof	Balcony
Dead load [KN/m²]	3.75	2.0	3.0
Imposed live load [KN/m²]	2	1	2.5

The dead load value consists of the self-weight of the slab plus non-structural floor finishes.

3.4.2. Fully coupled soil structure model

The model dimensions of the ground are 120 m, 90 m and 28 m respectively in the X, Y and Z direction. The model contains 80917 elements and 309878 nodes. The front view of the coupled structure model is shown in Figure 3.15, while a 3D view is also shown in Figure 3.16.

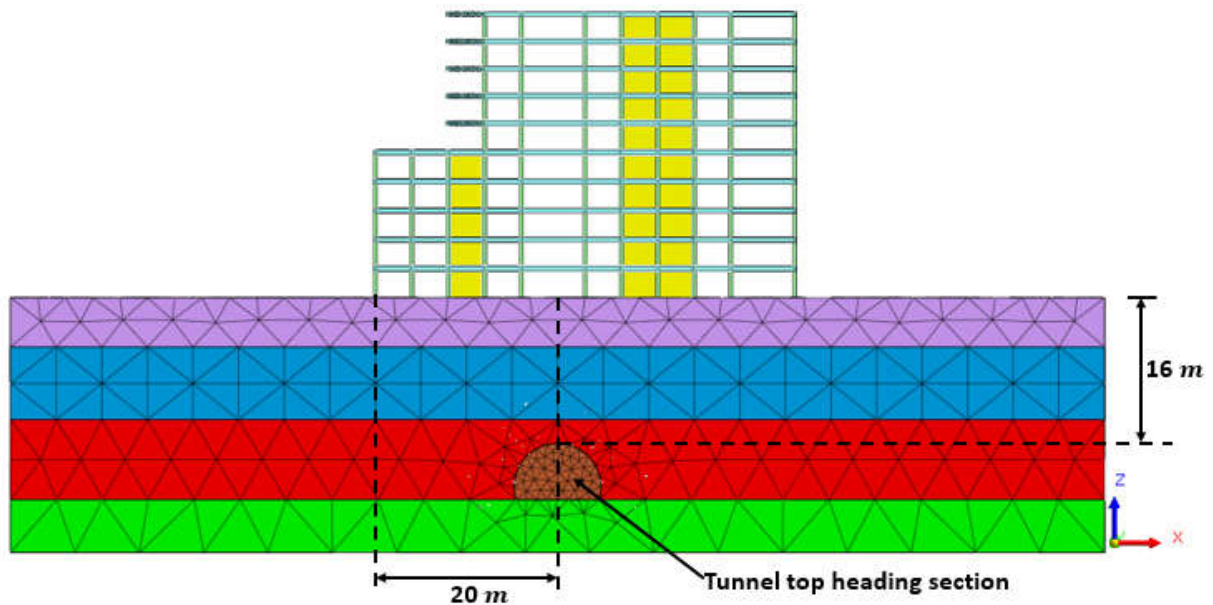


Figure 3.15. Front view of the fully coupled soil structure numerical model.

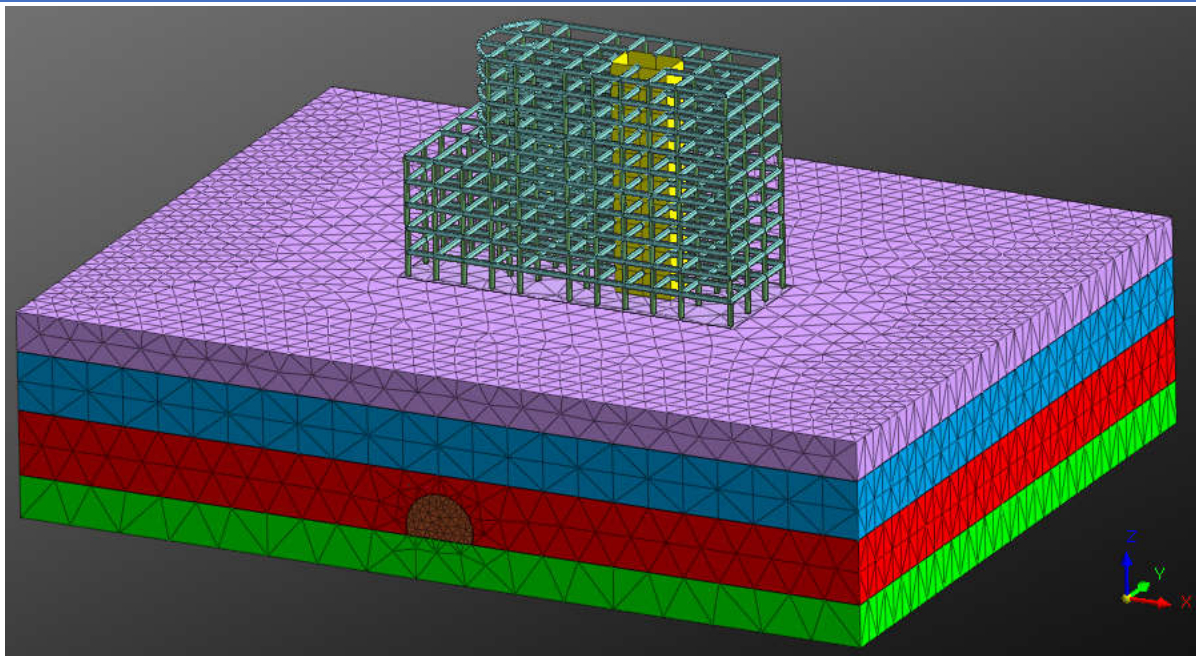


Figure 3.16. FE model of 3D fully coupled structure interaction.

The structure is placed in the model with its centre of mass positioned directly over the tunnel axis line (tunnel axis line parallel to Y-axis) as shown in Figure 3.17.

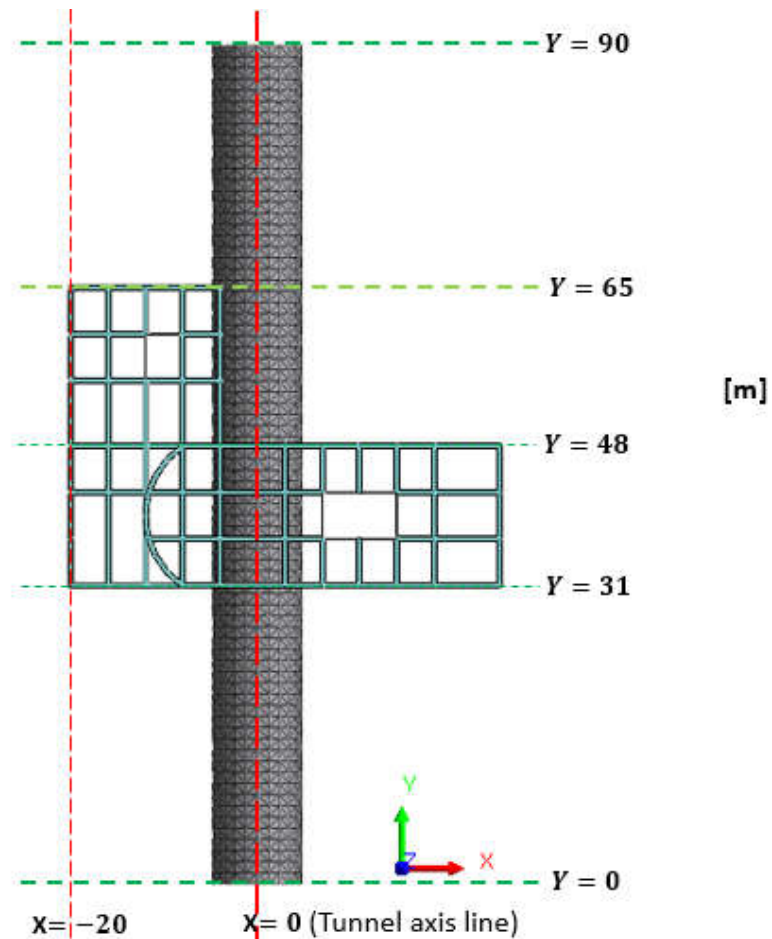


Figure 3.17. Position of the building in top of the tunnel.

3.4.3. Tunnel construction stages

The simulation of the tunnel construction in the coupled soil structure interaction case was performed with a total of 80 construction stages. The construction stages are presented detailly in Appendix D. Figure 3.18 shows a 3D view of the tunnel excavation sequence at construction stage 32, that is, tunnel face located at $Y = 37.2\text{ m}$ from the tunnel opening.

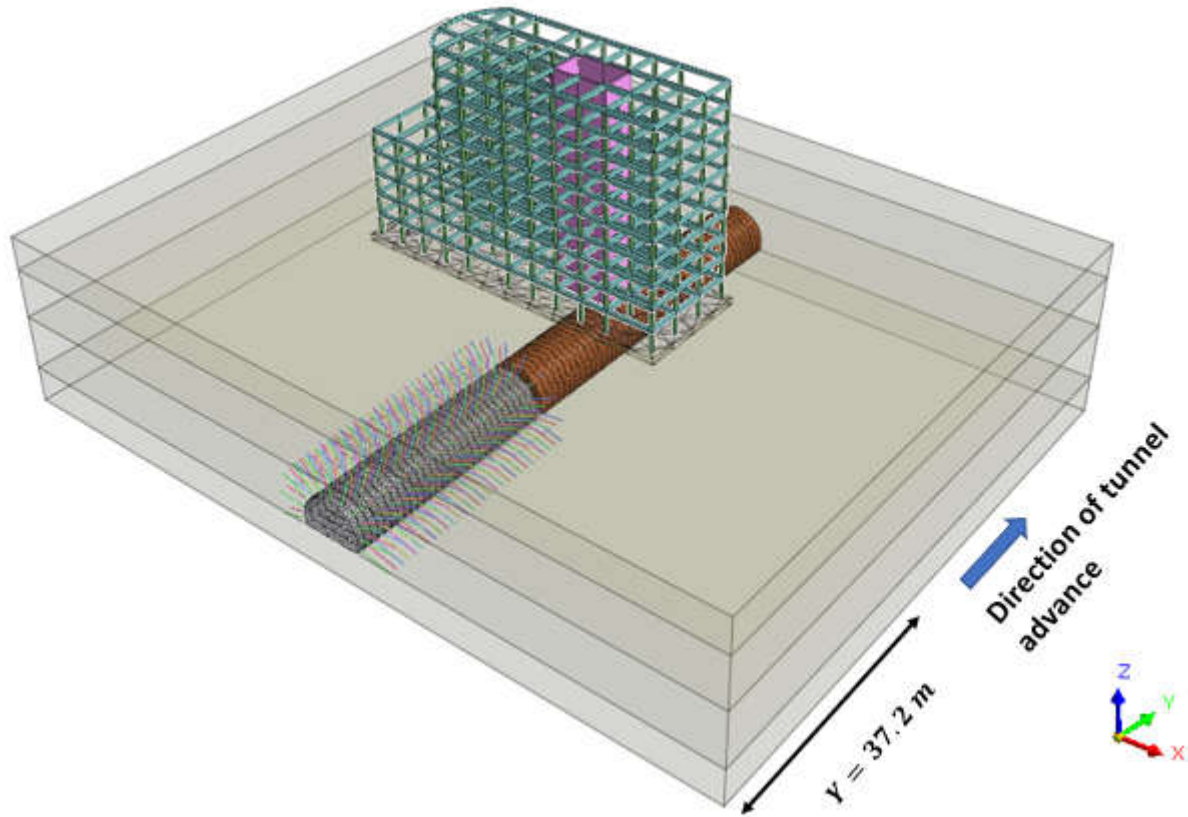


Figure 3.18. Simulation of tunnel excavation sequence at construction stage 32.

3.5. Finite element analysis results

The results obtained from MIDAS GTS NX for the simulation in greenfield situation and for the coupled soil structure interaction are analysed in Microsoft Excel to obtain the different graphs.

3.5.1. Greenfield analysis results

The distribution of surface settlements and strains on the ground surface are as follows.

3.5.1.1. Transverse settlements

The maximum surface settlement for tunnelling in greenfield conditions occurred at the last excavation stage. The maximum value of 1.9 cm obtained from the numerical model was validated against the maximum value of 1.95 cm measured in the field (Section 3.3.2). Figure 3.19 illustrates the settlement trough obtained at the last excavation stage section with the corresponding Gaussian fitted curve. The acronym CS denotes the construction stage.

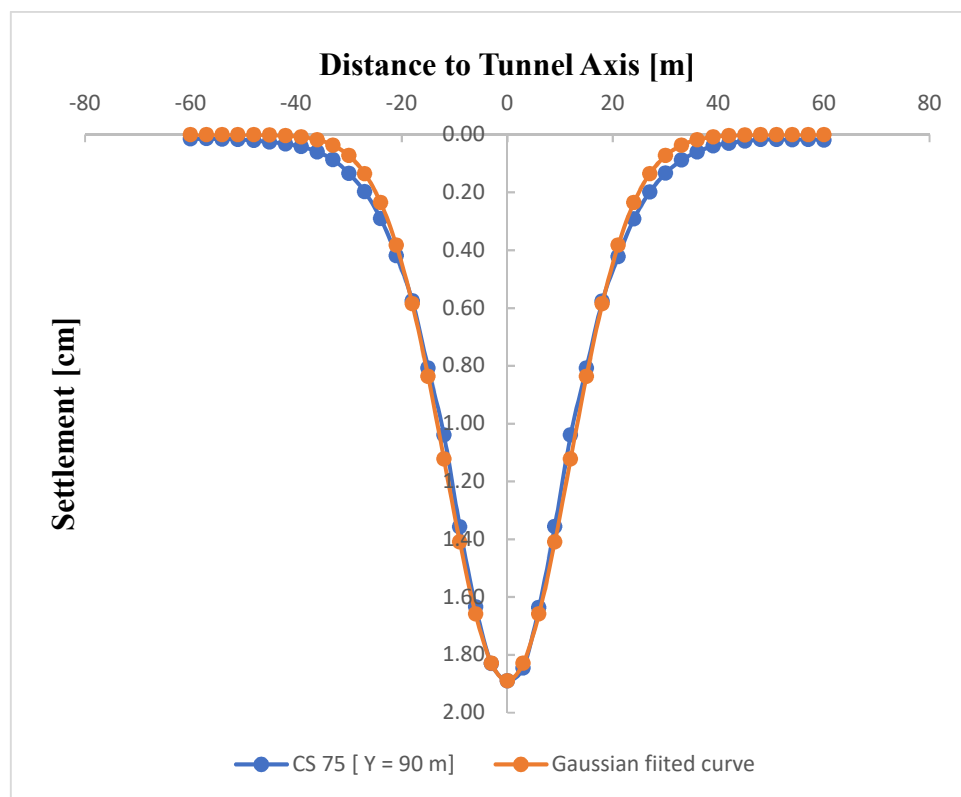


Figure 3.19. Transverse settlement profile at $Y= 90$ m from tunnel opening.

As shown in Figure 3.19, the computed settlement corresponds well to a Gaussian curve with the horizontal distance from the tunnel axis to the point of inflection $i = 12$ m. The compliance of this results with the empirical solution indicates that the adopted numerical model can be used to carry complex soil structure interaction problems.

3.5.1.2. Longitudinal settlements

Figure 3.20 illustrates the greenfield longitudinal settlement profiles above the tunnel centreline at some chosen stages of excavation, with the position of the tunnel face indicated by an arrow for the corresponding phase.

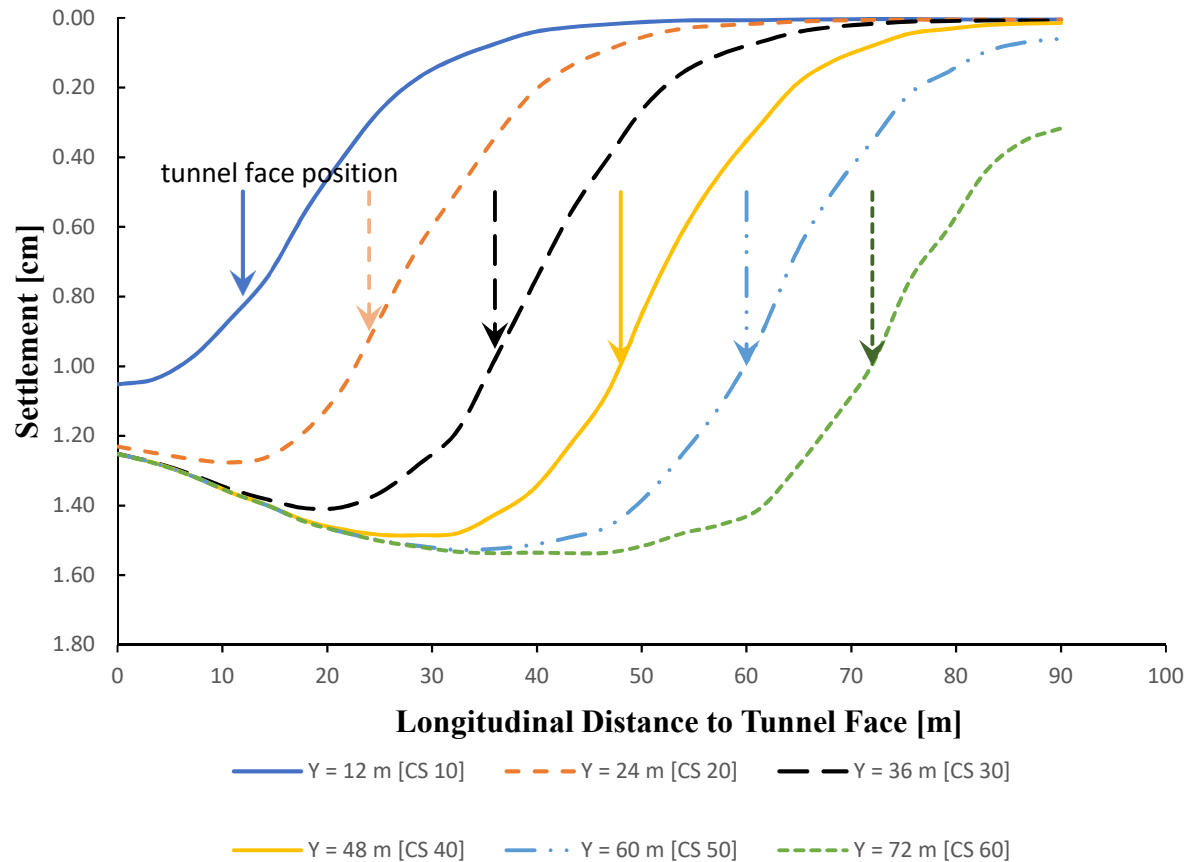


Figure 3.20. Longitudinal tunneling induced settlement profiles at different positions of tunnel face.

It can be seen that as the tunnel face advances, the longitudinal profiles tend to reach a maximum value. The settlements above the position of the tunnel face are approximately 60% of the maximum settlement at that corresponding construction stage. Also shown in Figure 3.21 are the vertical displacement contours for the tunnel face at $Y = 72 \text{ m}$ from the tunnel opening.

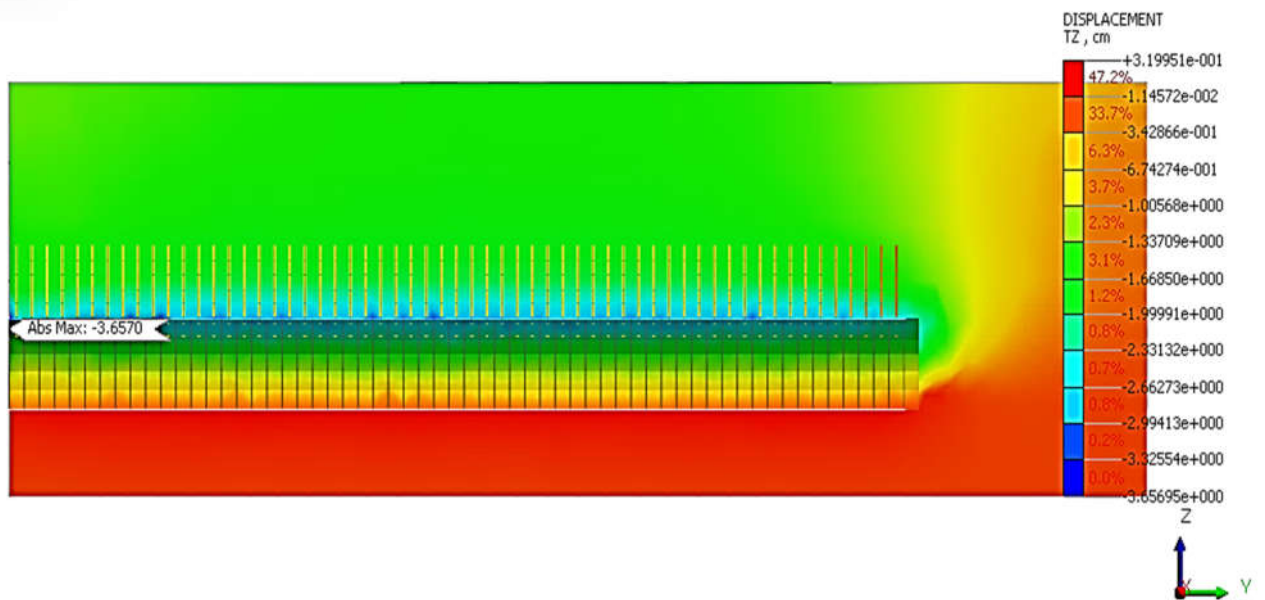


Figure 3.21. Vertical displacement contours at construction stage 60 ($Y=72$ m).

3.5.1.3. Horizontal surface strains

The transverse horizontal surface strains increase gradually as the excavation advances, with the maximum compressive and tensile strains occurring at the last excavation stage (CS 75), are represented in Figure 3.22.

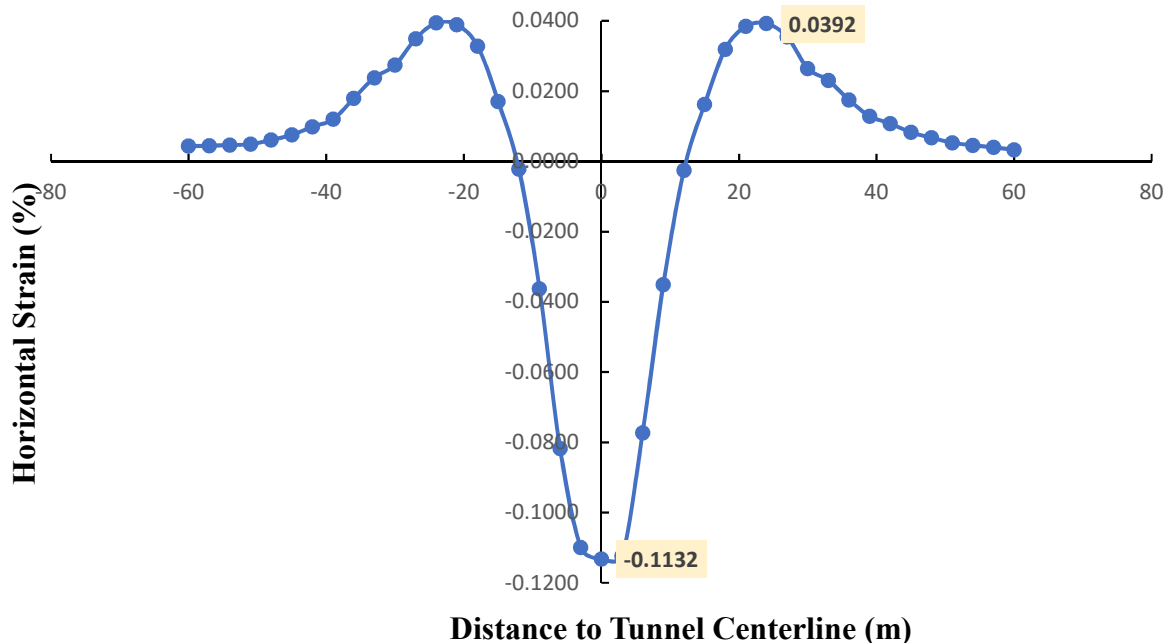


Figure 3.22. Maximum compressive and tensile surface horizontal strains.

It can be seen from the graph that approximately between -12 m to 12 m, all the strains are compressive, confirming $i \cong 12 \text{ m}$ as the point of inflection of the greenfield settlement profile at this stage. The maximum compressive strain of 0.1132% occurs at the point directly above the tunnel centerline while the maximum tensile strain is 0.0392% occurring at horizontal distance of 23 m from the tunnel center line. The empirical relations assume the maximum tensile strain to occur at a horizontal distance of $\sqrt{3}i$, that is, approximately 21 m in this case, which is still too close to the value given by this finite element analysis.

The horizontal strain contours at the last construction stage can be seen in Figure 3.23 below.

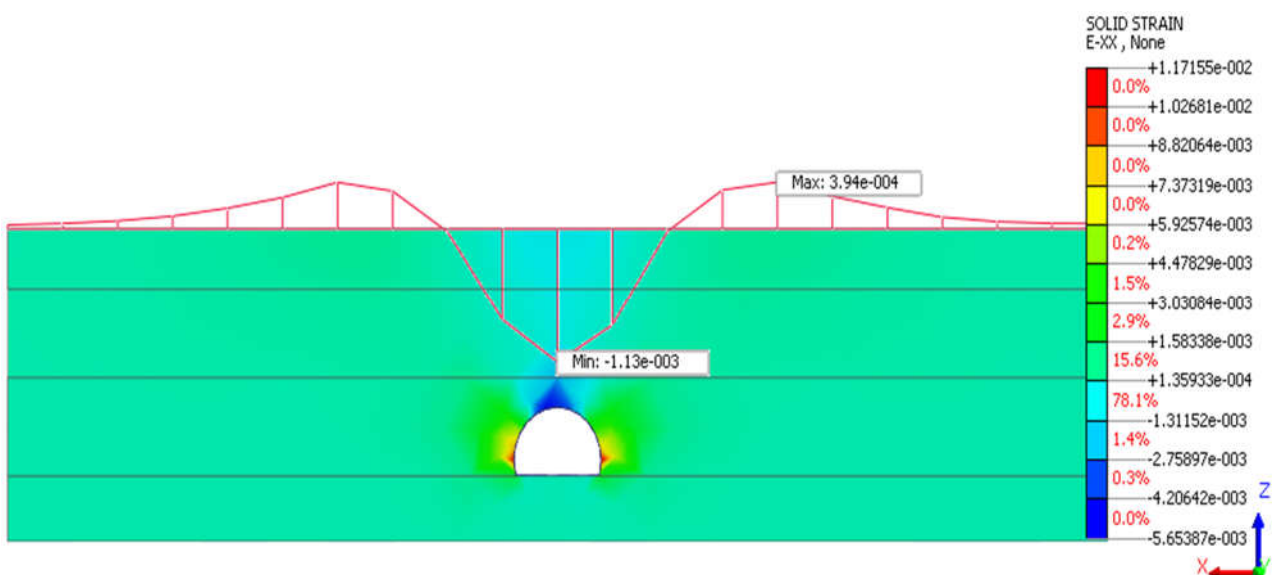


Figure 3.23. Surface horizontal strain contours at last excavation stage (transverse section at $Y = 90 \text{ m}$).

3.5.2. Coupled soil structure interaction analysis results

In Figure 3.24 and Figure 3.25, the evolution of vertical displacements in the global model is presented at an intermediate construction stage (construction stage 50). It can be seen that the displacements of the structural members in the vicinity of the tunnel face are too high. At this stage, the structure undergoes a maximum vertical displacement of 12.18 mm at the raft.

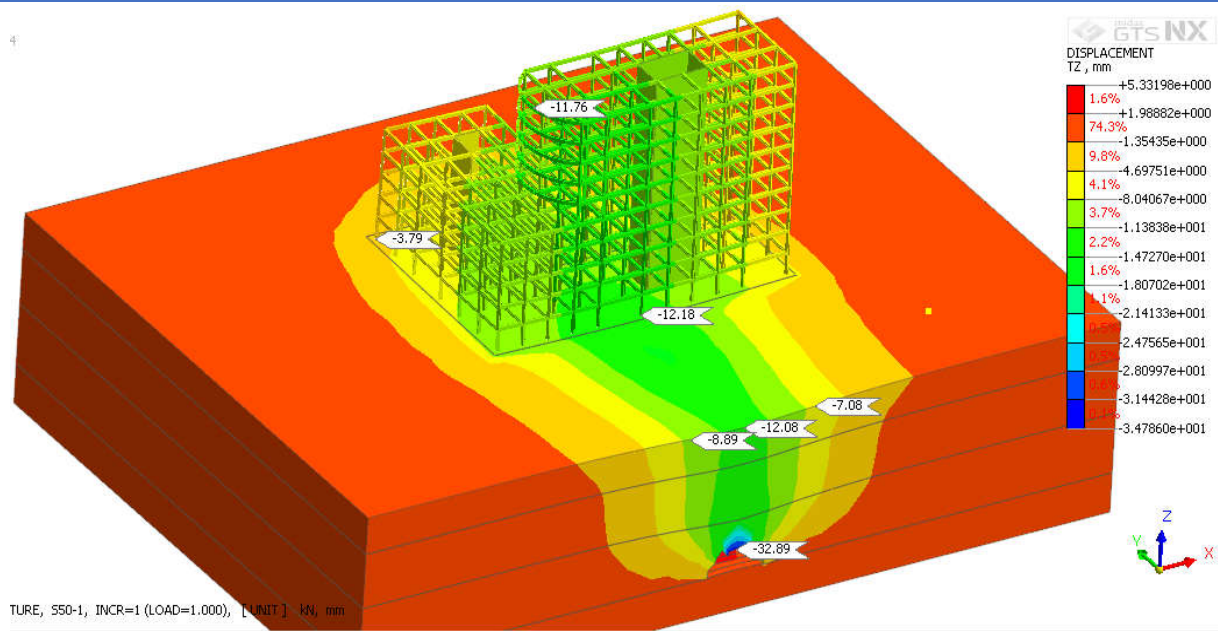


Figure 3.24. 3D view of vertical displacement contours of the global model at construction stage 50.

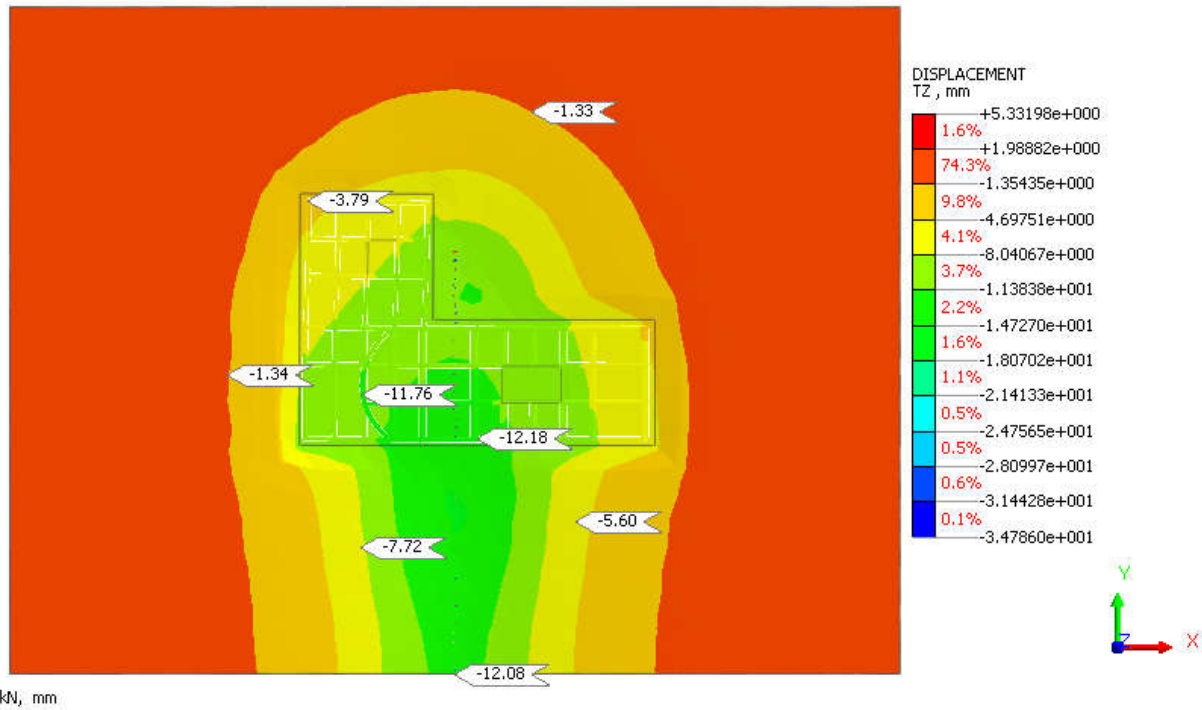


Figure 3.25. Plan view: vertical displacement of the global model.

3.5.2.1. Tunneling and building loads induced surface settlements

The settlements are compared with those obtained from the greenfield condition. The longitudinal ground profile of the settlement for the case of the existence of the superstructure

at various positions of tunnel advancements is shown in Figure 3.26. The acronyms GF and CSSI refer to the Greenfield and Coupled Soil Structure Interaction cases respectively.

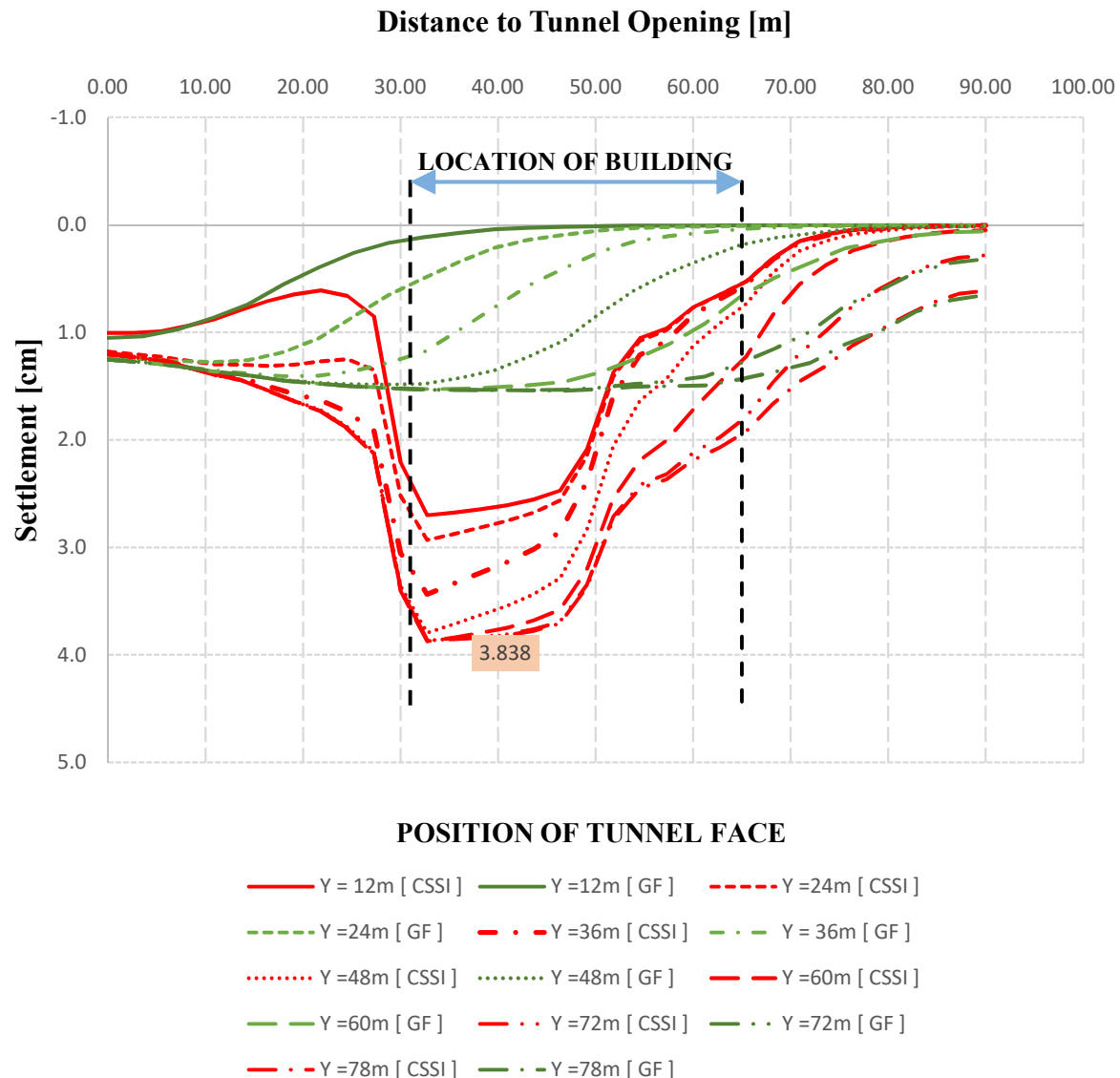


Figure 3.26. Comparison between longitudinal settlement profiles of the greenfield and coupled structure interaction situations with regard to the tunnel advancement.

Differences between greenfield settlements and the coupled soil structure interaction case increase as the tunnel face moves closer to the position of the structure. The highest difference corresponds to the center of mass of the superstructure. These differences occur due to the influence building loads, including its weight have on the displacements caused by the tunnel excavation. Plasticity is induced in the zones closer to the foundation. This behavior is also a result of the adopted soil constitutive model's stiffness dependence on stress levels leading to non-negligible role of the building loads.

Figure 3.27 below also shows the variation of the transverse settlement profile at $Y = 32 m$ from the tunnel opening with the tunnel advancement.

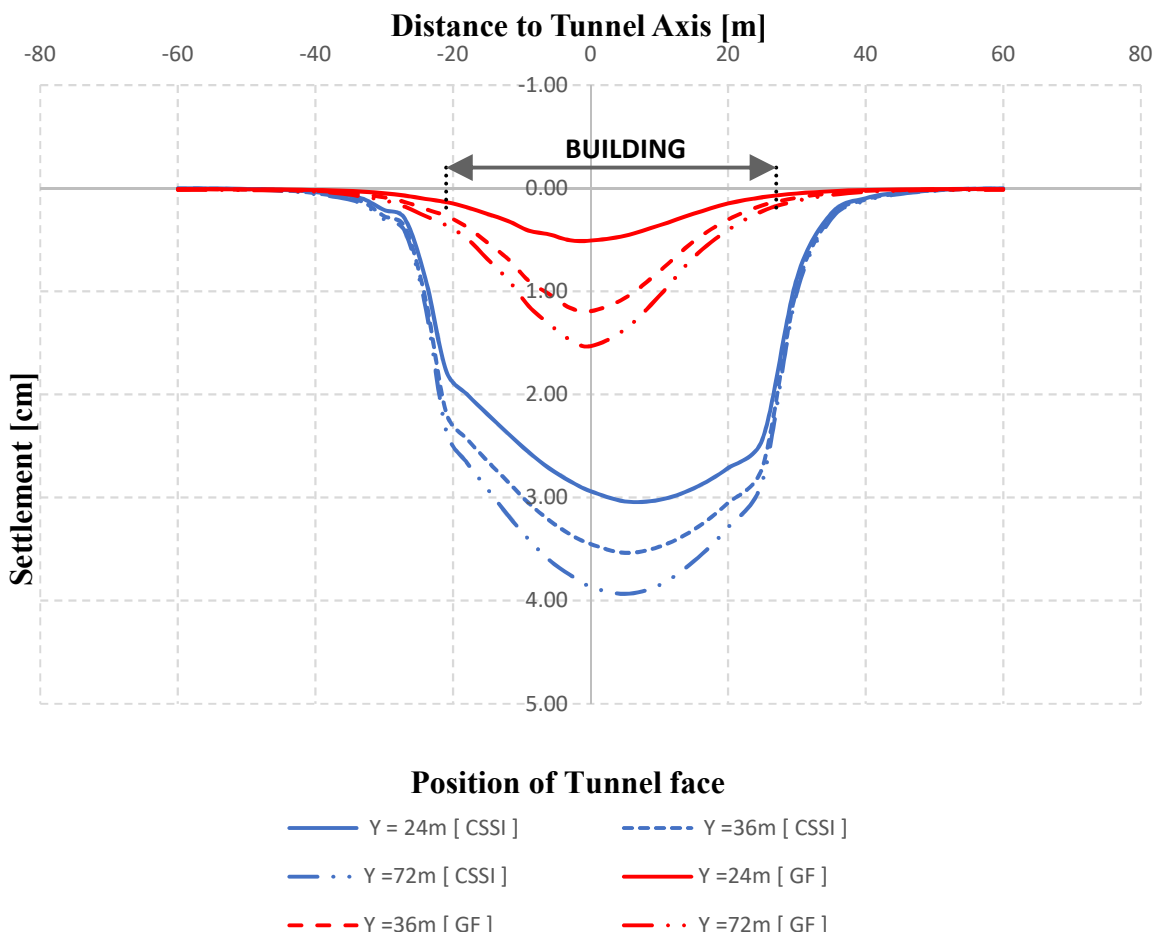


Figure 3.27. Comparison between transverse settlement profiles of the greenfield and coupled structure interaction situations ($Y = 32 m$) with regards to the tunnel advancement.

3.5.2.2. Tunnelling induced building settlement

The maximum computed settlement of the building foundation is illustrated in Figure 3.28. It is obvious that the building responded rigidly. The figure demonstrates that the building's presence reduces the maximum settlement compared to the greenfield situation. Case studies have shown that the building's stiffness interacts with the ground such that deflection ratio and horizontal strains are reduced(Frischmann et al., 1994). The maximum value of 12.45 mm occurs at the foundation point above the tunnel axis line at a distance of $Y = 42 \text{ m}$ from the tunnel opening at construction stage 67.

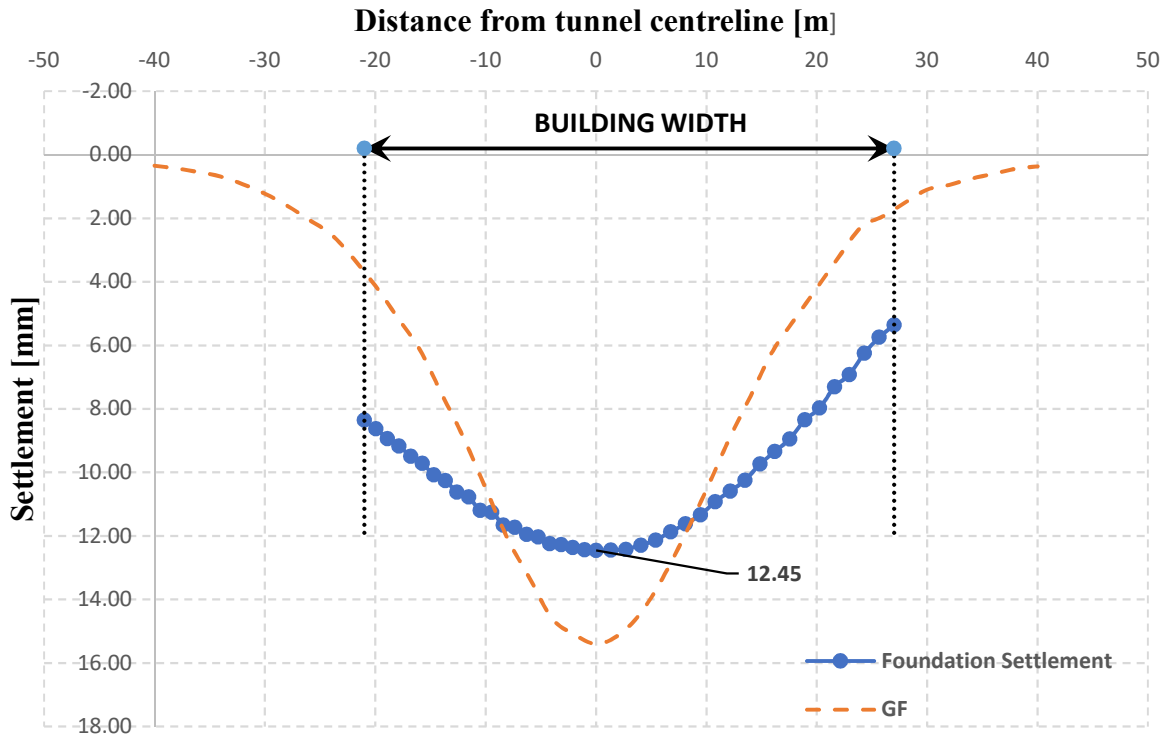


Figure 3.28. Tunnel-induced foundation settlement.

Settlements of building around the trough shoulders are also larger than the greenfield values, indicating that the building embeds into the soil. This likely developed due to the redistribution of the building's loads as the tunnel moved closer to the building.

The polynomial curve $y = -0.0099x^2 - 0.0065x + 12.26$ with a coefficient of determination $R^2 = 0.99$, clearly fitted the settlement profile of the foundation. This curve has no point of inflection as it is always concave up. This indicates that the foundation is completely in sagging. Figure 3.29 shows the settlement contours of the foundation at this construction stage (CS67) together with the transverse section at $Y = 42 m$.

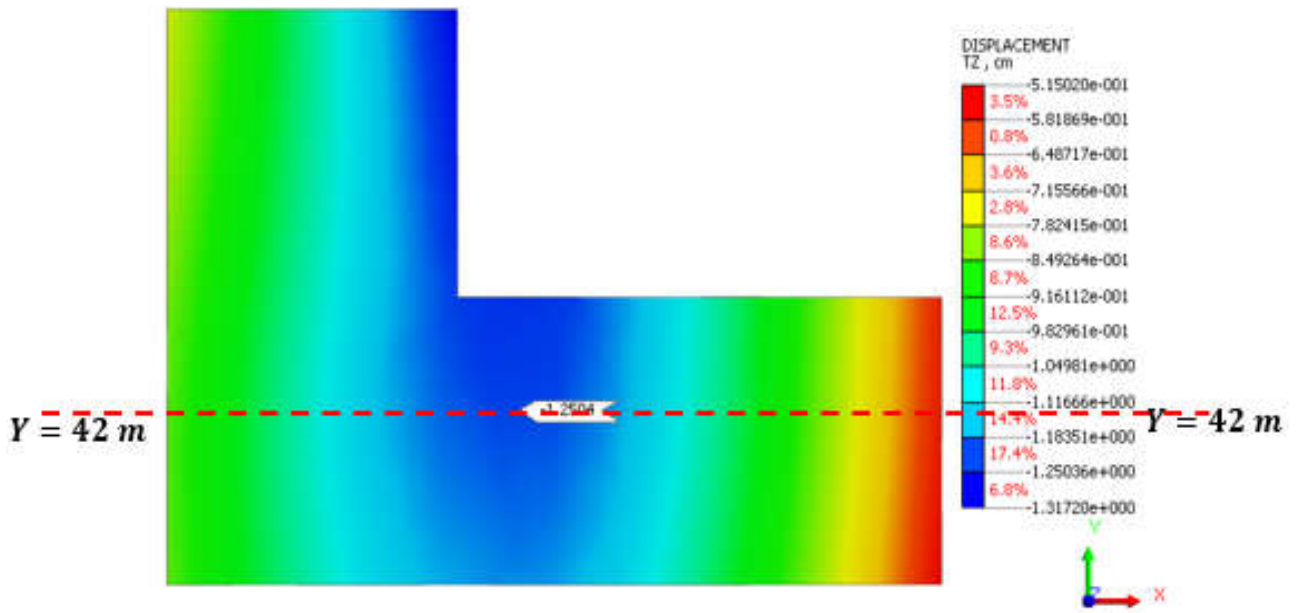


Figure 3.29. Foundation settlement contours with tunnel heading at $Y = 79.2\text{ m}$ (CS67).

3.5.2.3. Tunnel induced foundation strains

The distribution of the horizontal strains on the transverse section of the raft at a distance $Y = 42\text{ m}$ from the tunnel opening where the maximum induced settlement was observed (Section 3.5.2.2 above) is illustrated in Figure 3.30.

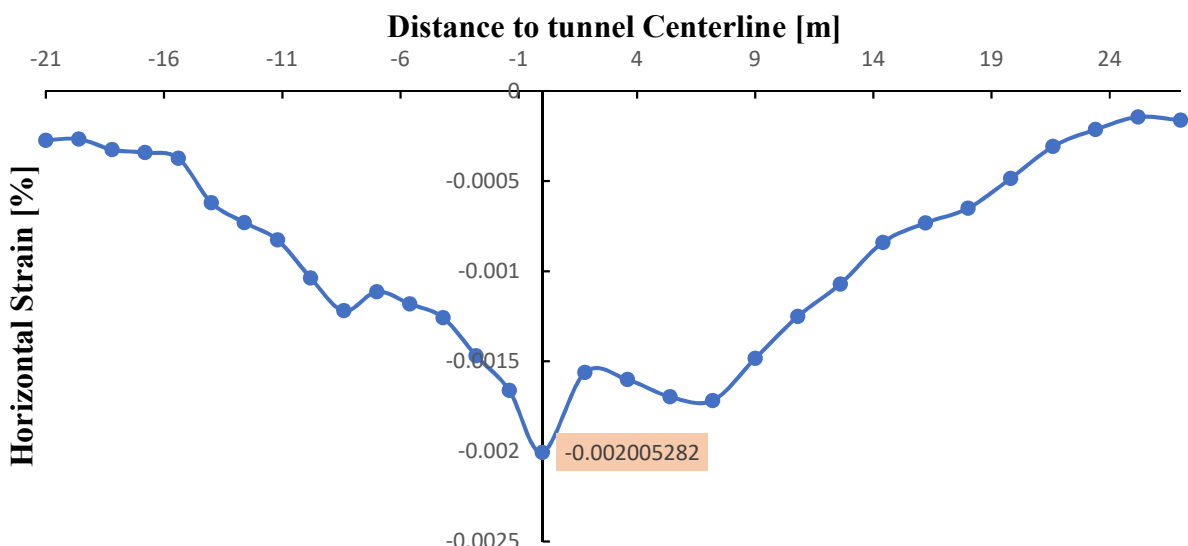


Figure 3.30. Induced Transverse horizontal strains on the foundation.

As can be seen from Figure 3.30 above, only compressive strains are induced on the foundation indicating that the foundation is completely in sagging as was shown in section

3.5.2.2. An absolute maximum compressive strain of **0.002%** is observed at the point directly above the tunnel axis. Comparing this value to the absolute max compressive strain of **0.1132%** obtained for the greenfield situation, we see that the stiffness of the foundation greatly reduces the horizontal strains induced by tunnel excavation, that is, a 98% decrease of strain.

Due to the irregularity of the building in plan, a region of strain concentration is expected. Figure 3.31 shows the horizontal strain contours on the raft at the end of construction.

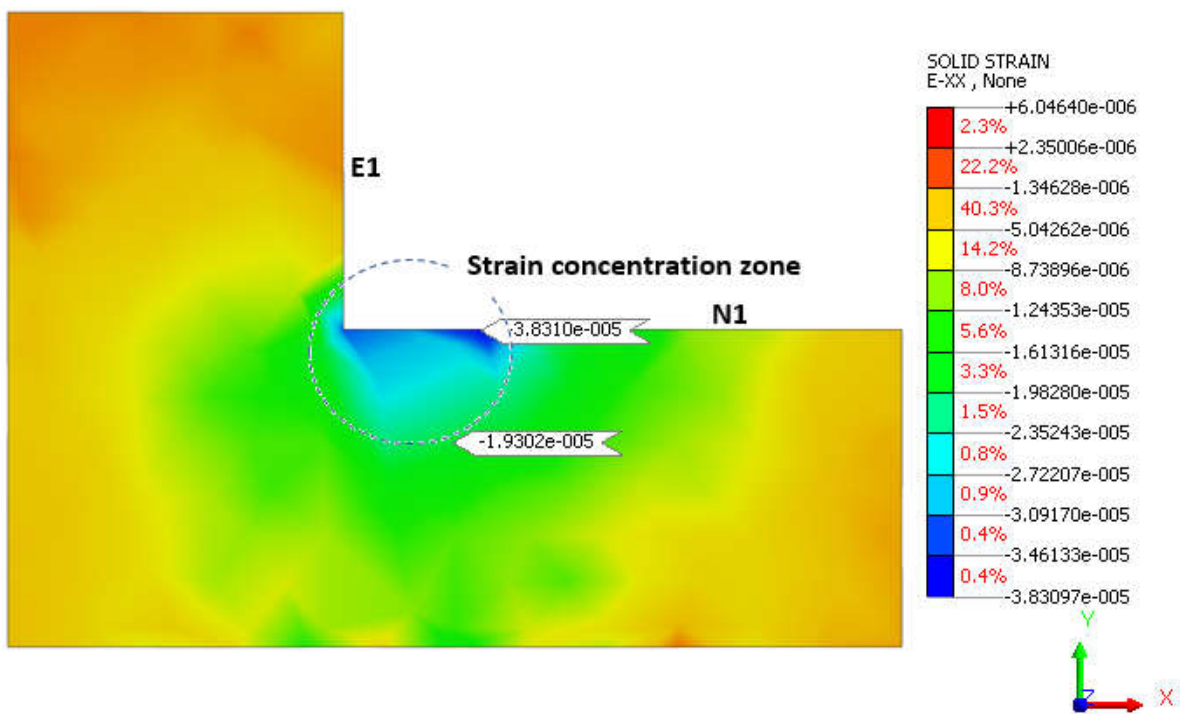


Figure 3.31. horizontal strain contours in the X direction at the end of the excavation sequence.

From the strain contours shown, a strain concentration zone occurs at the intersection between façade E1 and N1 indicated in the figure.

3.5.2.4. Vertical displacement of tunnel crown.

Figure 3.32 shows the vertical displacements of the tunnel crown after 70 excavation steps. It is seen that displacements show zigzagging, with high values occurring at the front of the lining rings than at the back. As expected, the values of vertical displacement increase for the lining rings under the building due to the increase vertical effective stress induced by the building. The high displacement value observed at the entrance of the tunnel is due to fact that arching around the first excavation was hardly possible because the side boundary was free to

displace vertically. A moving average of period 2 indicated in Figure 3.32 gives a maximum displacement of about 3.7 cm in the vicinity of the building.

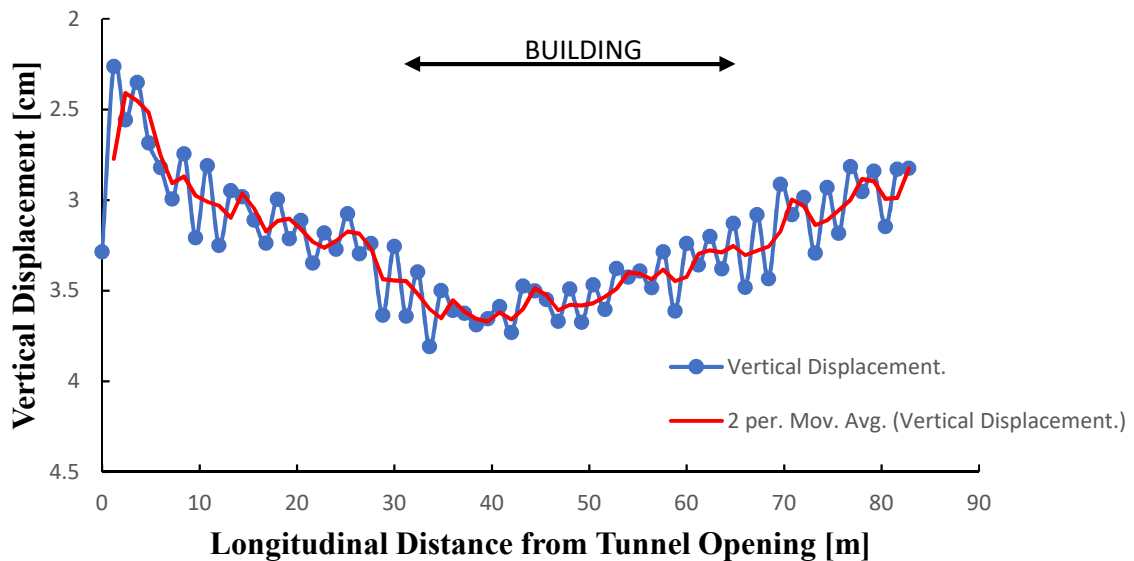


Figure 3.32. Vertical displacements of the tunnel crown.

The vertical displacement contours of the shotcrete lining are shown in Figure 3.33.

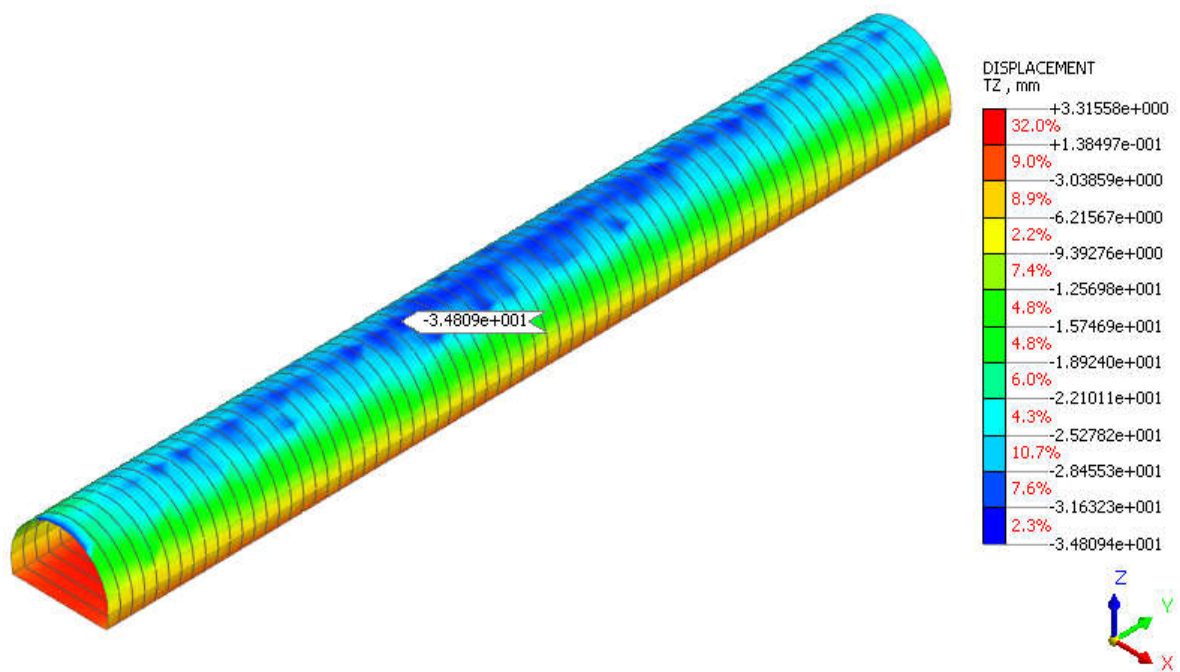


Figure 3.33. Deformations of shotcrete segments after 70 excavations steps.

3.5.2.5. Strains on the shotcrete lining.

The major principal strains on the shotcrete lining segments are indicated by contours in Figure 3.34. The maximum compressive strain that occurs is far less than the ultimate concrete compressive strain of about 0.2%, meaning failure doesn't occur. The tensile strains, though very small in magnitude can be accounted for by introducing steel meshes or steel arches in the shotcrete.

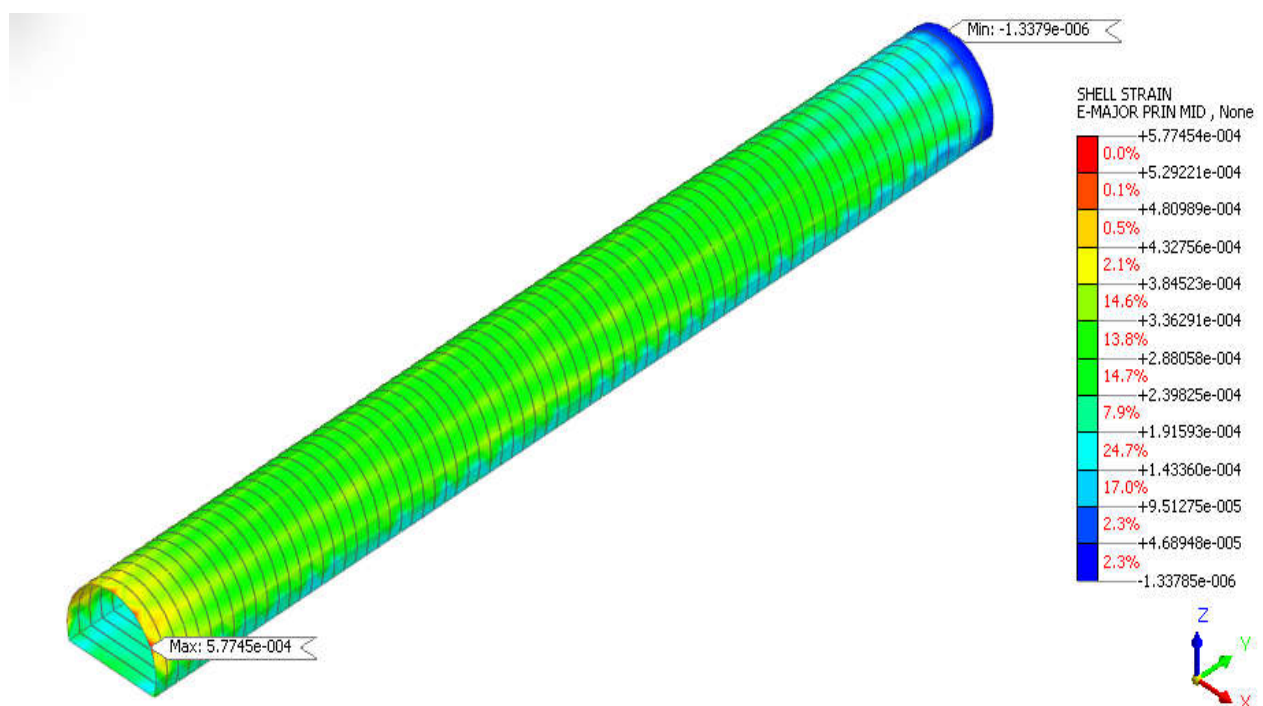


Figure 3.34. Major principal strains on the shotcrete segments at the end of excavation.

3.5.2.6. Axial force on rock bolts

Figure 3.35 shows the axial forces on the rock bolts at the last construction stage. The maximum compressive and tensile axial force are found to be 182 KN and 257 KN respectively. This indicates that rock bolts with a design yield strength greater than or equal 135 MPa would be sufficient for the process.

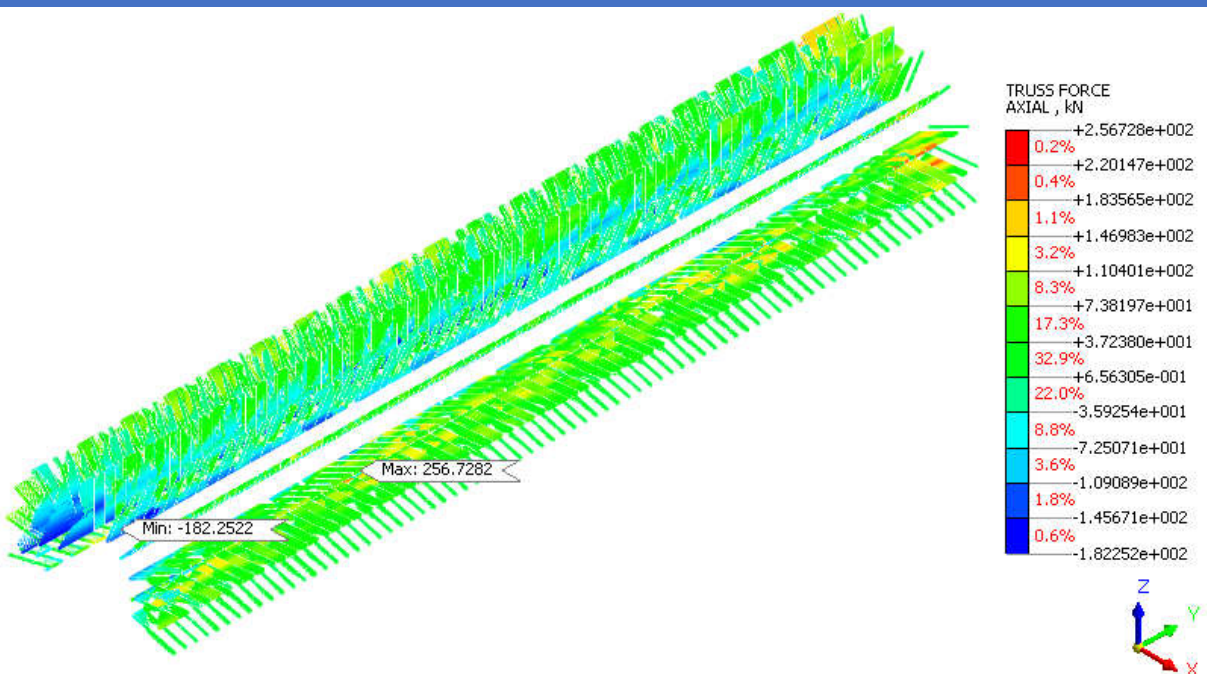


Figure 3.35. Axial forces on rock bolts at the end of excavation.

3.6. Structural response

The response of the structure as the tunnel advances would be investigated both in ordinary conditions (substructure approach of soil structure interaction) and for the fully coupled soil structure interaction case.

3.6.1. Response of the structure under ordinary conditions

The vertical linear springs used to describe the foundation had stiffnesses ranging from 308 KN/m to 49000 KN/m. The solicitations and the deformation of the structure under ordinary conditions are hereby presented.

3.6.1.1. Structure deformation under ordinary conditions

The vertical displacement of the raft foundation under service combination is about 5 cm. The deformation of the structure is illustrated below in Figure 3.36.

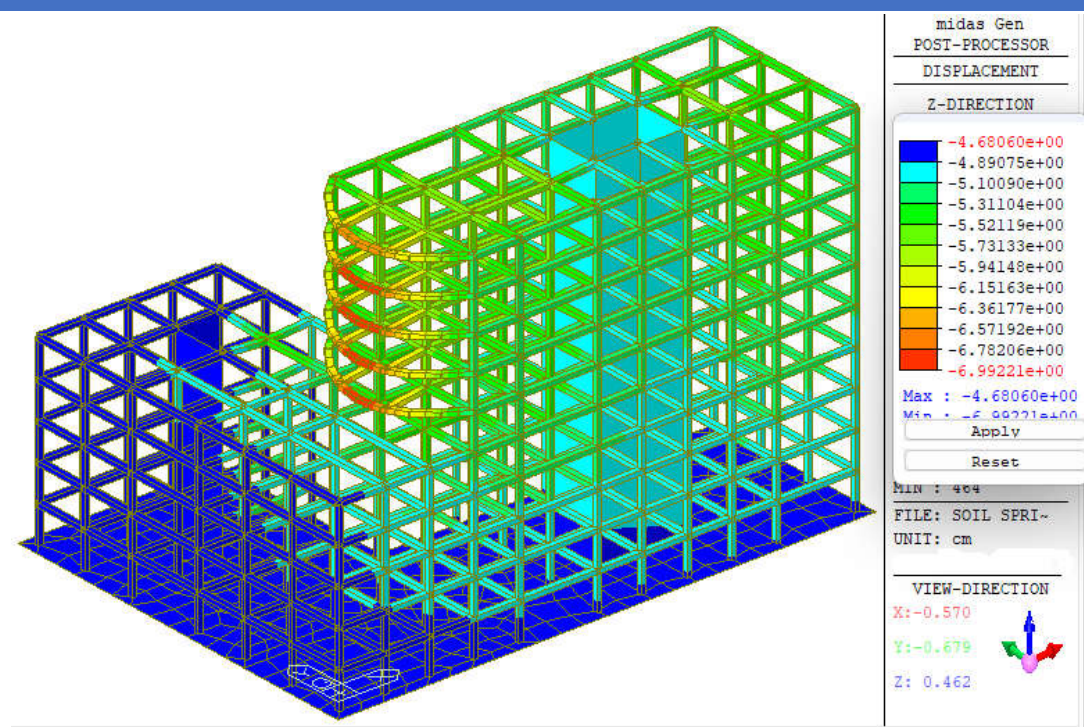


Figure 3.36. Vertical displacement of the structure under normal conditions.

3.6.1.2. Solicitations under ordinary conditions

The axial forces acting on the elements is shown in Figure 3.37. The maximum being 2000 KN.

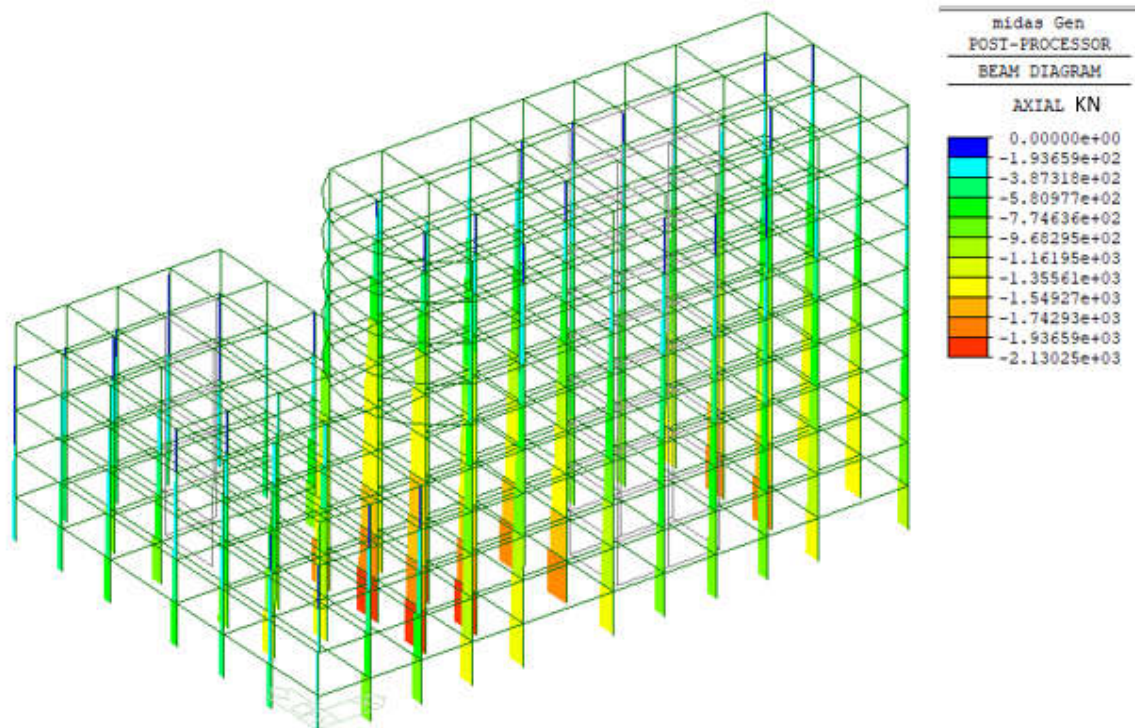


Figure 3.37. Axial forces on structure under normal conditions.

3.6.2. Structural response of the structure due to tunnelling

Indicated in Figure 3.38 are the structural elements which are to be investigated. They are chosen from the ground floor and located at the point above the tunnel axis at a distance of 32 m from the tunnel opening (i.e. $Y = 32$ m).

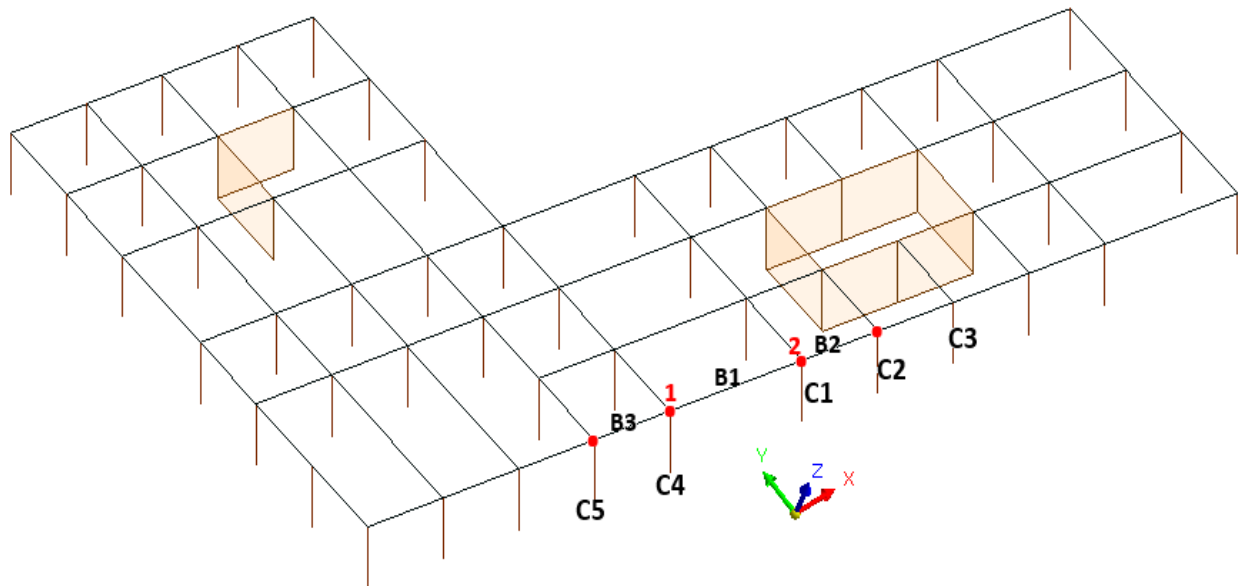


Figure 3.38. location of the examined structural elements on the base floor.

The investigated beams are indicated by B1, B2 and B3 symbols, while the columns are indicated by C1 to C5. The variation of axial forces and vertical displacements of the columns, and also the bending moments (at end nodes) in the beams are then examined.

3.6.2.1. Variation of vertical displacements of columns

Vertical displacements as the tunnel advances of columns C1, C2 and C3 are shown in Figure 3.39, whereas the vertical displacements of C4 and C5 are displayed in Figure 3.40. As the tunnel face advances, the displacements of the columns increase. When the tunnel face arrives at the location of the building, the settlements of the columns increase at a higher rate before eventually coming to an almost steady value. By comparing these figures, it can be seen that the columns that are closer to the tunnel axis settle more than those farther away from it. Comparing the settlements of C1, C2 and C3, it can see that C1 which is the closest to the tunnel axis line has a maximum vertical displacement of 1.22 cm, followed by C2 with 1.16 cm and that of C3 is 1.07 cm.

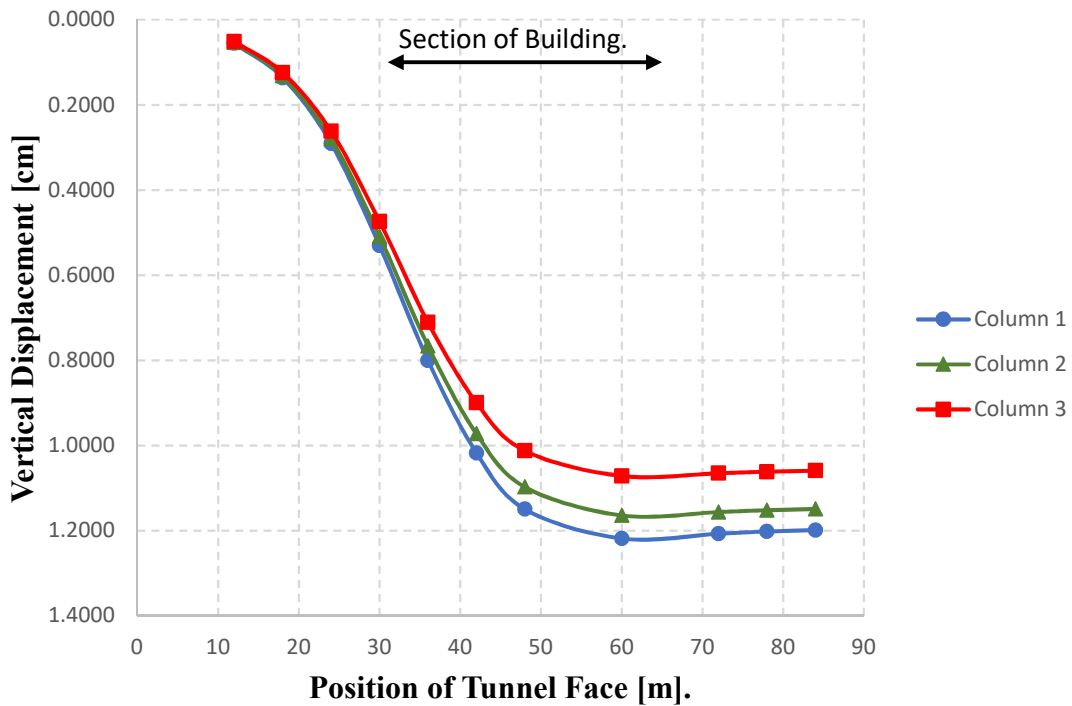


Figure 3.39. Variation of the vertical displacement of columns (C1, C2, C3) with tunnel advancement.

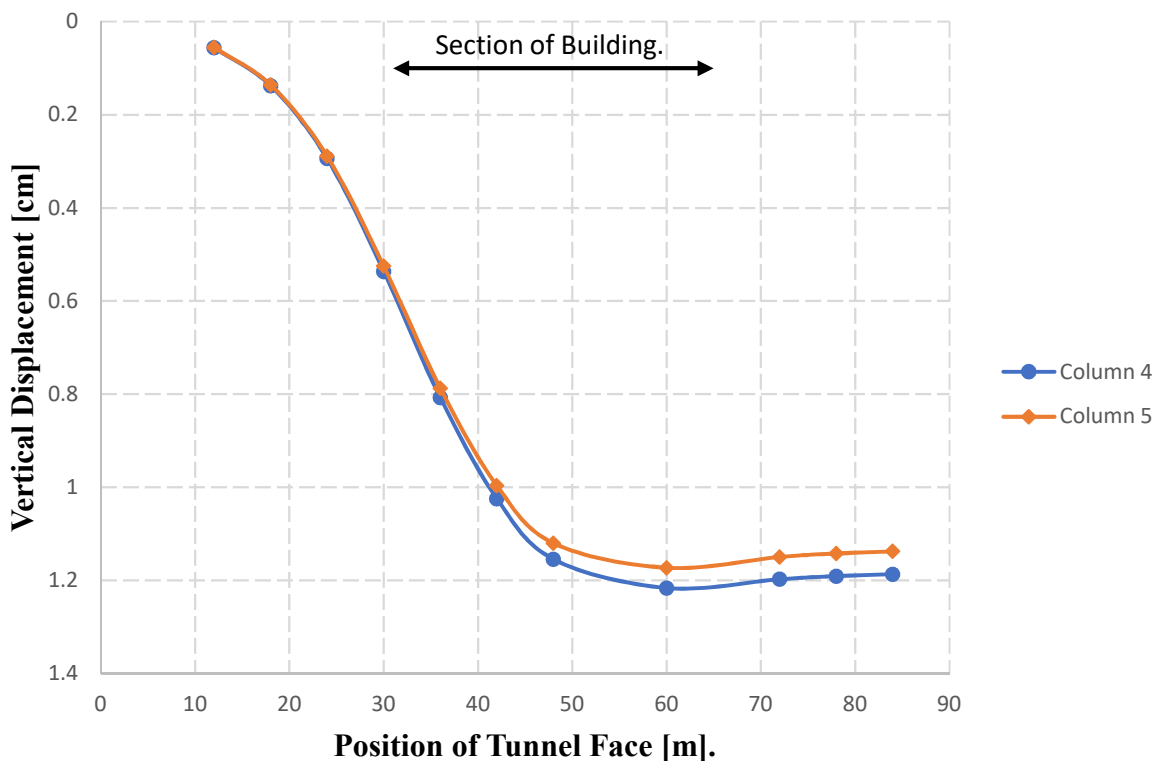


Figure 3.40. Variation of the vertical displacement of columns (C4, C5) with tunnel advancement.

3.6.2.2. Variation of the axial forces of columns

The variation of axial forces of columns 1 to 5 as the tunnel advances is illustrated in Figure 3.41 to Figure 3.45 below.

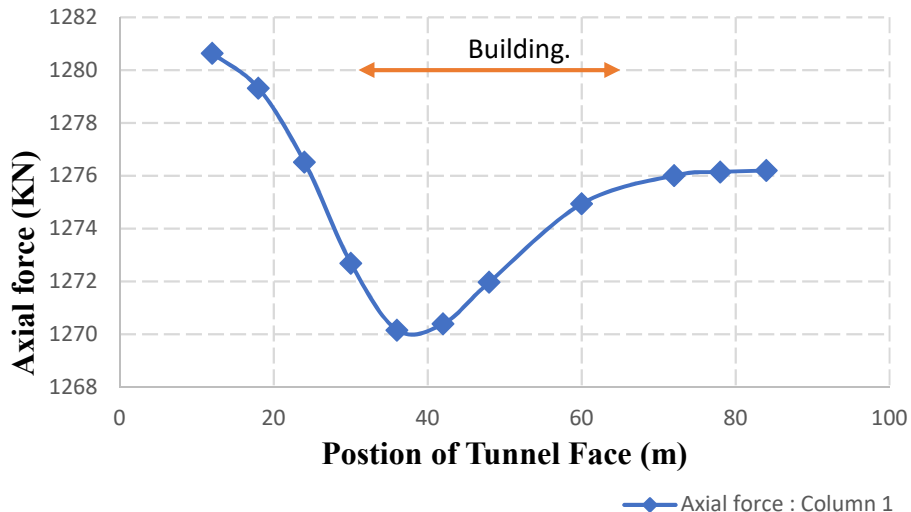


Figure 3.41. Variation of axial force of column 1.

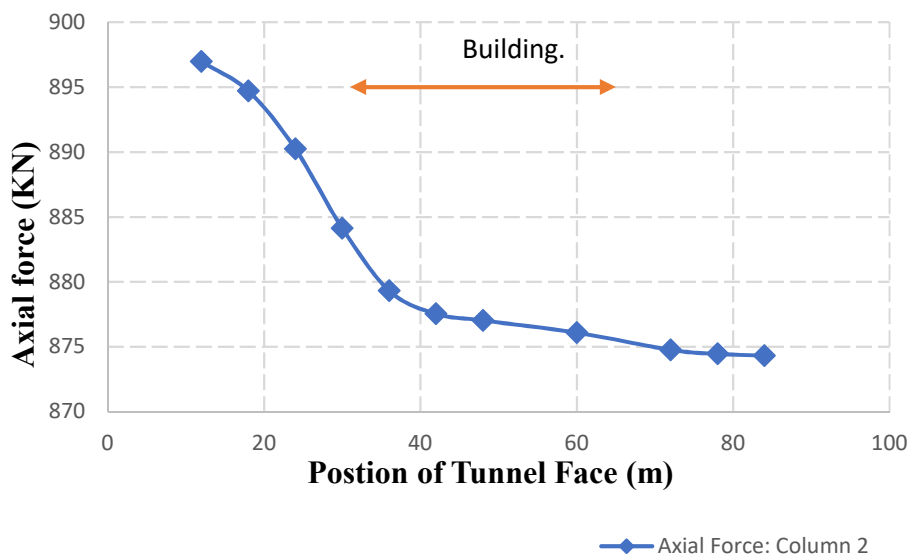
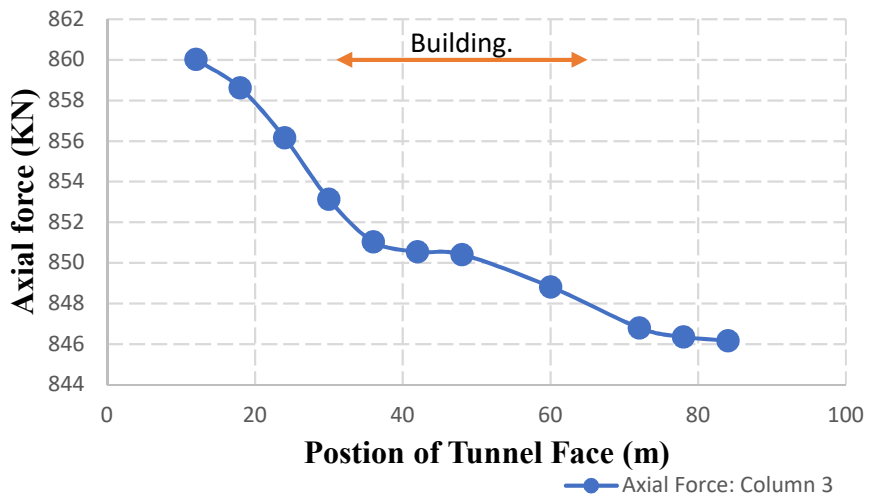
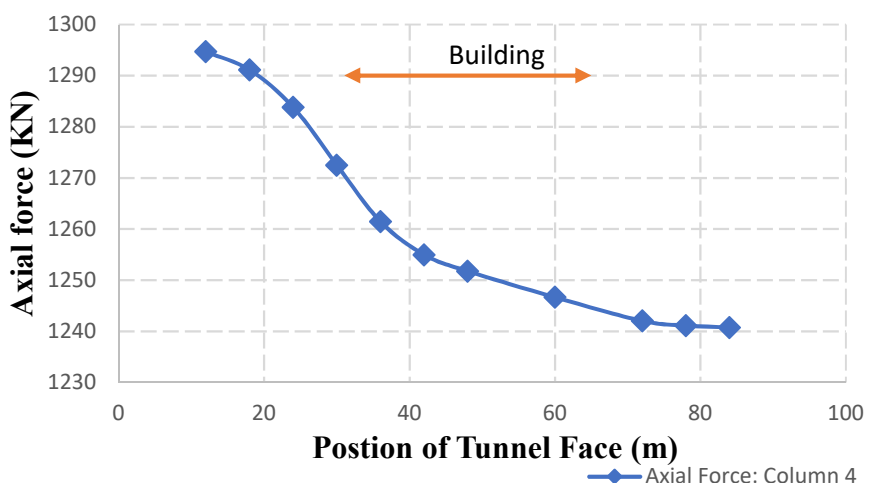
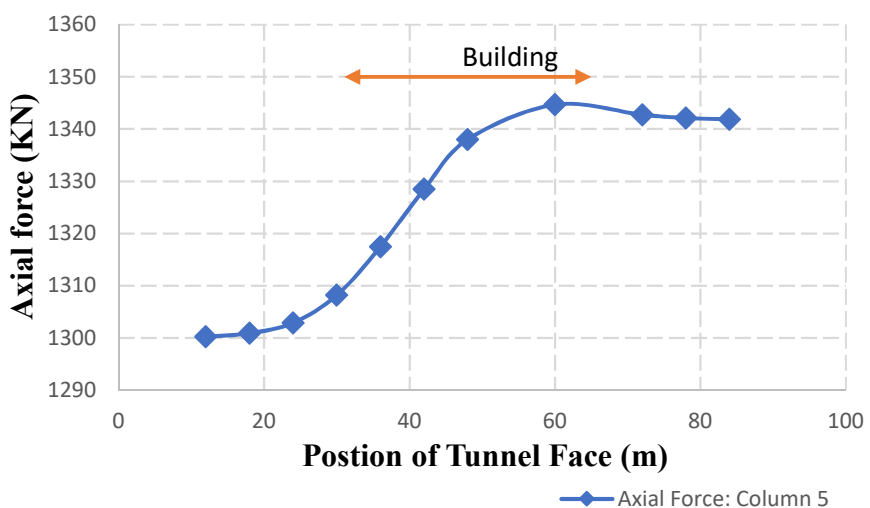


Figure 3.42. Variation of axial force of column 2.

**Figure 3.43.** Variation of axial force of column 3.**Figure 3.44.** Variation of axial force of column 4.**Figure 3.45.** Variation of axial force of column 5.

It can be observed that the settlement of column 2 causes some of its axial force to be released (Figure 3.42). The magnitude of this axial force decreases as the tunnel advances. For column 3 (Figure 3.43), it can also be seen that the axial force decreases as the tunnel face advances. The decreasing trend slows down a bit when the tunnel face is under the first block of the building due to the transfer of axial force from adjacent columns like C2 through beams to this column.

The variation of the axial force of column 4 also shows a decreasing trend as the column settles (Figure 3.44). This axial force is transferred to the adjacent column 5 by the beam causing the magnitude of axial force of this column to increase as the tunnel progresses (Figure 3.45). Although the settlement of this column reduces its axial force, the transfer of axial force from the adjacent columns highly increase its axial force. Column 1 that is represented in Figure 3.41 rather behaves in an abnormal way, which can be due to the unsymmetrical nature of the building and hence loads.

Figure 3.46 below shows the axial forces in the members at the end of construction. The maximum compressive value being 2200 KN.

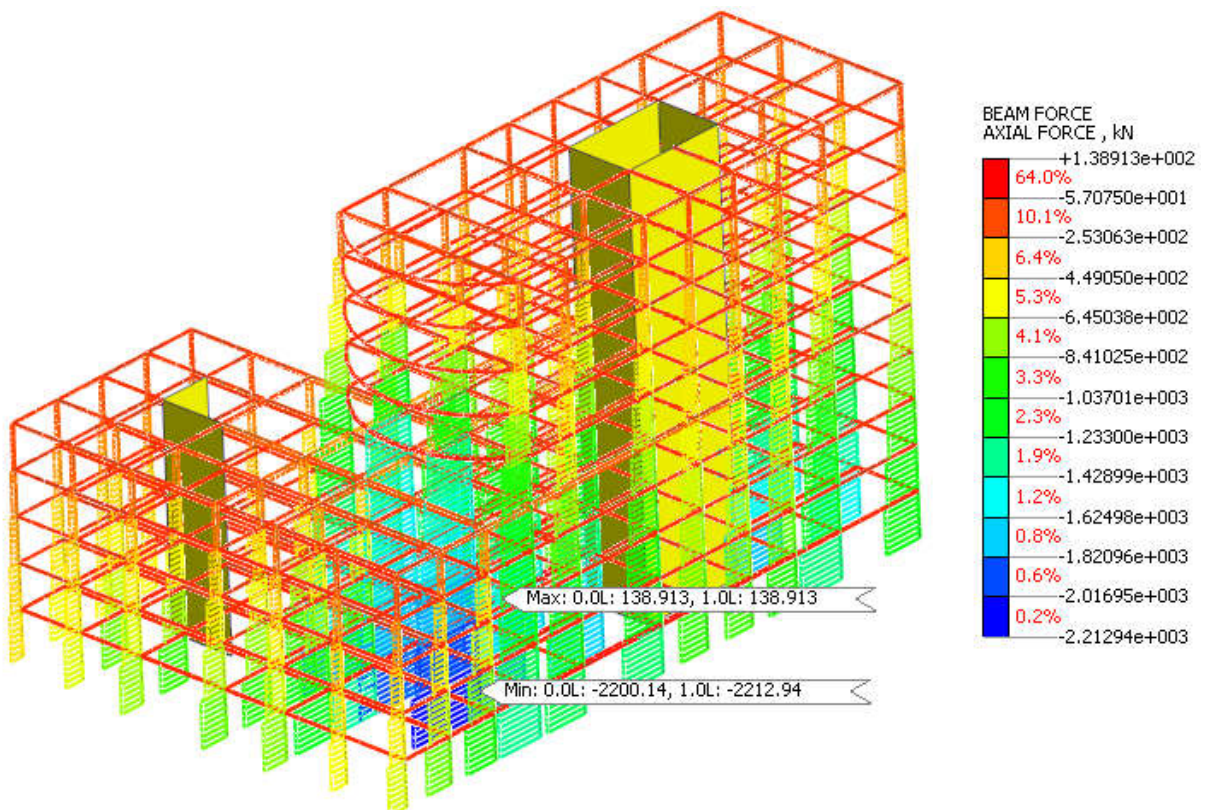


Figure 3.46. Axial forces in members at the end of construction.

3.6.2.3. Variation of the bending moments of beams

The variation of the bending moments at the end nodes of the studied beams (B1, B2 and B3) are illustrated below in Figures 3.47 to 3.49.

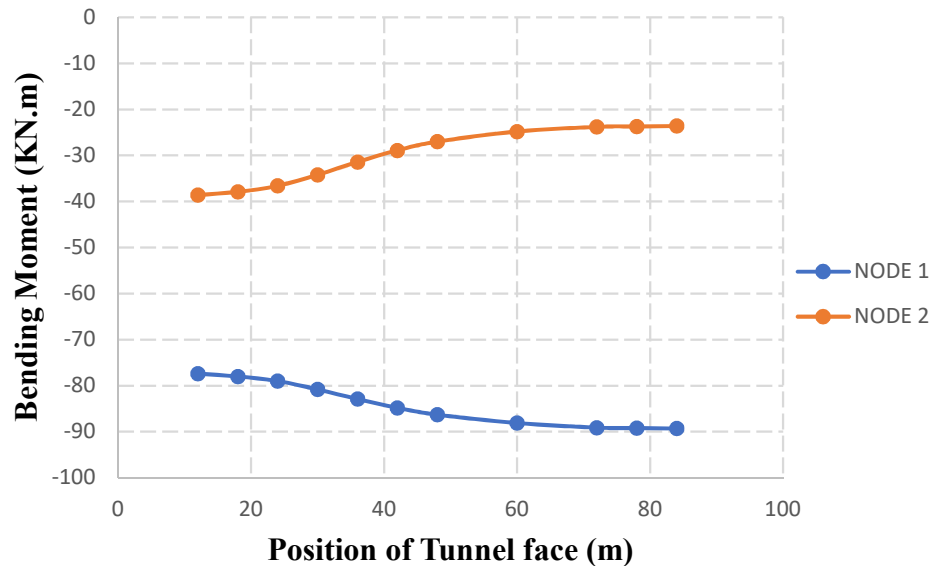


Figure 3.47. Variation of the bending moment of beam B1 as the tunnel advances.

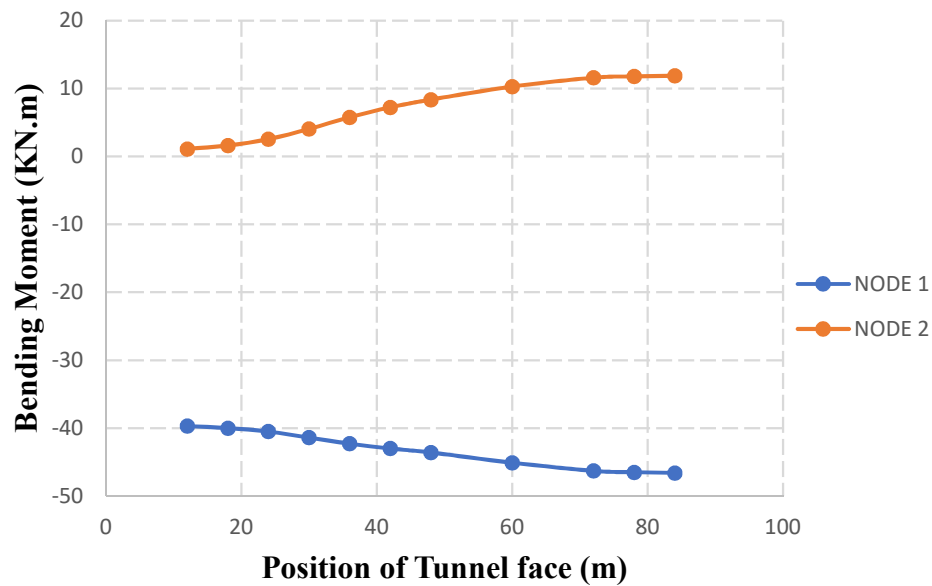


Figure 3.48. Variation of the bending moment of beam B2 as tunnel advances.

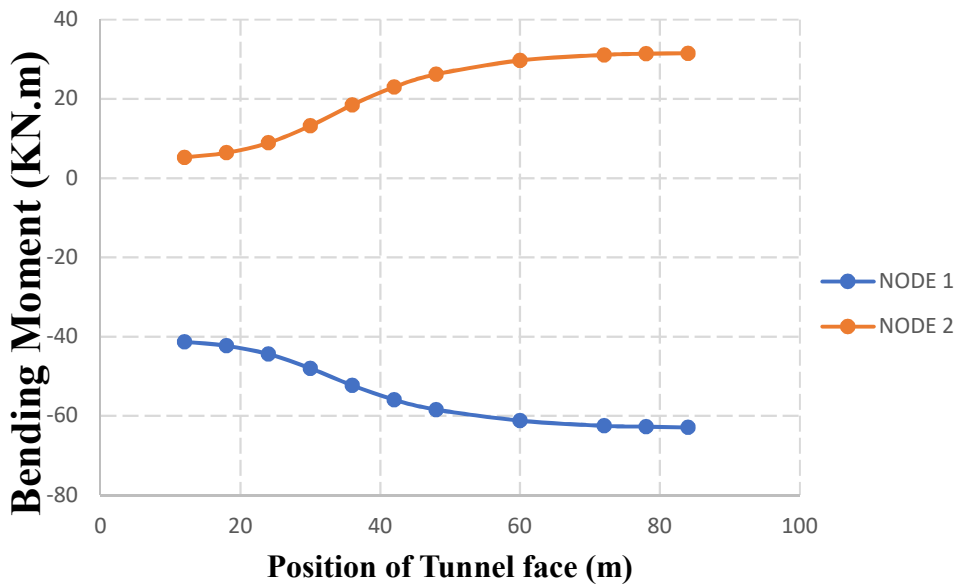


Figure 3.49. Variation of the bending moment of beam B3 as tunnel advances.

As observed from Figure 3.47, because of the axial force transmission, the beams experience an increase in the absolute value of bending moment at node 1 of beam B1 as the tunnel progresses. The absolute values of bending moments of the end nodes of beam 2 and beam 3 (Figure 3.48 and Figure 3.49 respectively) both show an increasing trend of the magnitude of bending moment. This is caused by the transmission of axial forces from the adjacent columns to the others as the tunnel progresses.

3.7. Evaluation of building damage category

In this case study, the potential damage to the building would be evaluated both when soil structure interaction is considered and when it is not considered.

3.7.1. Building damage with soil structure interaction considered

The potential building damage is assessed using the damage criterion proposed by Burland & Wroth, (1974) described in Section 1.4.3. This criterion related deflection ratio DR and horizontal strain ε_h to damage category using interaction diagrams dealing with the parts of the building in the sagging and hogging zone as separate parts.

As was shown in section 3.5.2.2, for the maximum building settlement, the foundation was completely in sagging. The damage interaction diagram is obtained for this building using Equations 2.9 and 2.10. The height of building $H = 31.2 \text{ m}$, and the transverse length of the building in sagging $L_{\text{Sag}} = 48 \text{ m}$. Figure 3.50 shows the damage interaction diagram of the building.

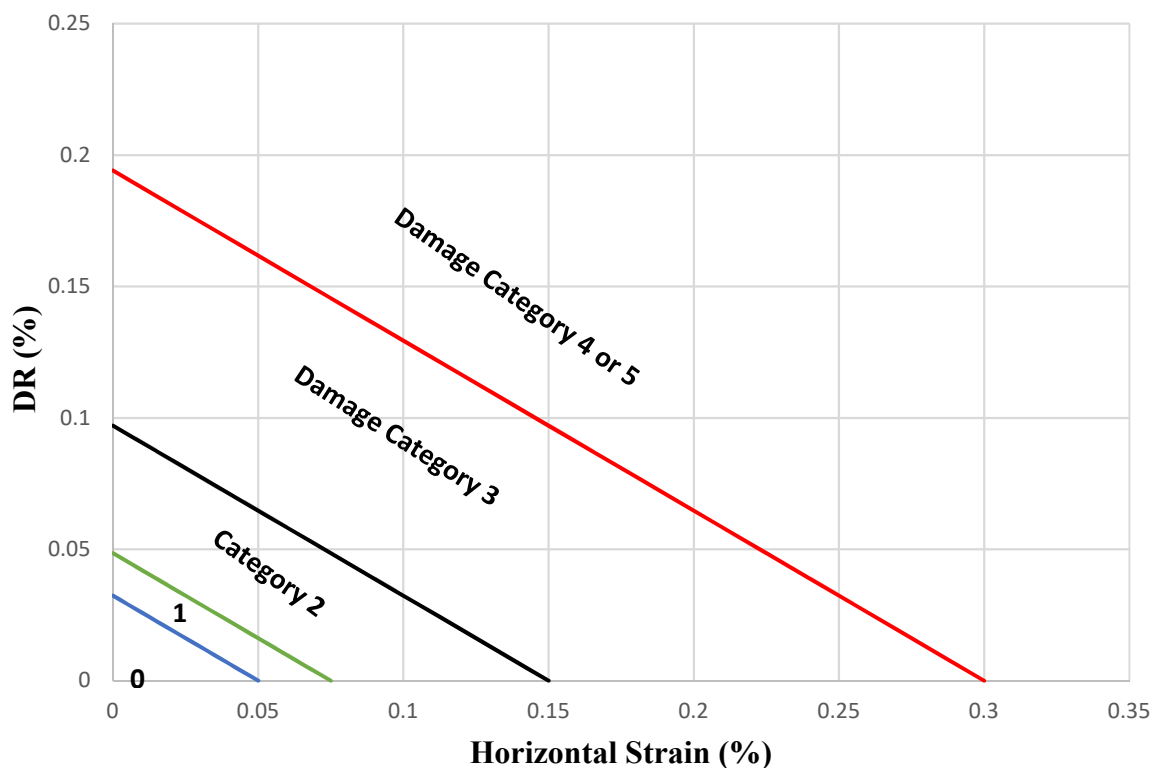


Figure 3.50. Building damage interaction diagram for sagging ($L/H=1.53$).

The deflection ratio DR_{Sag} of the structure is computed graphically from the tunnelling induced foundation settlement trough in Section 3.3.2 as shown in Figure 3.51 below.

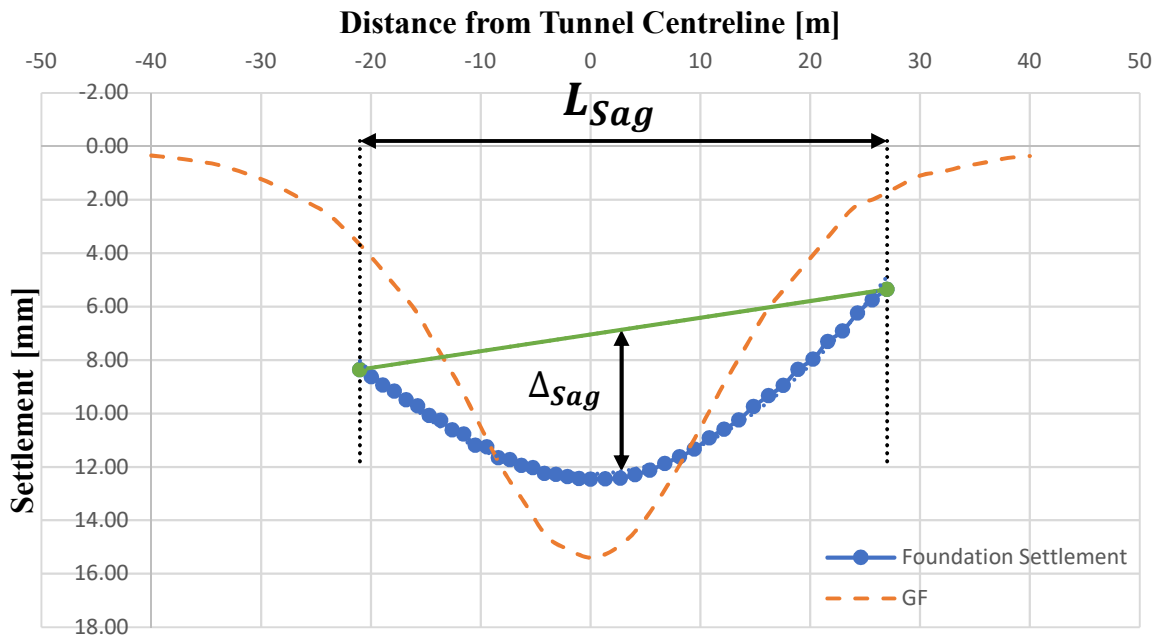


Figure 3.51. Determination of the deflection ratio of the structure.

The deflection ratio of the structure in sagging $DR_{Sag} = \frac{\Delta_{Sag}}{L_{Sag}}$ is obtained as 0.011%.

The maximum horizontal strain ε_h induced on the foundation by the sequential tunnel excavation was 0.002% as seen in Section 3.5.2.3. The point of $DR_{Sag} - \varepsilon_h$ pair is plotted in the damage interaction diagram to determine the category of damage as shown in Figure 3.52.

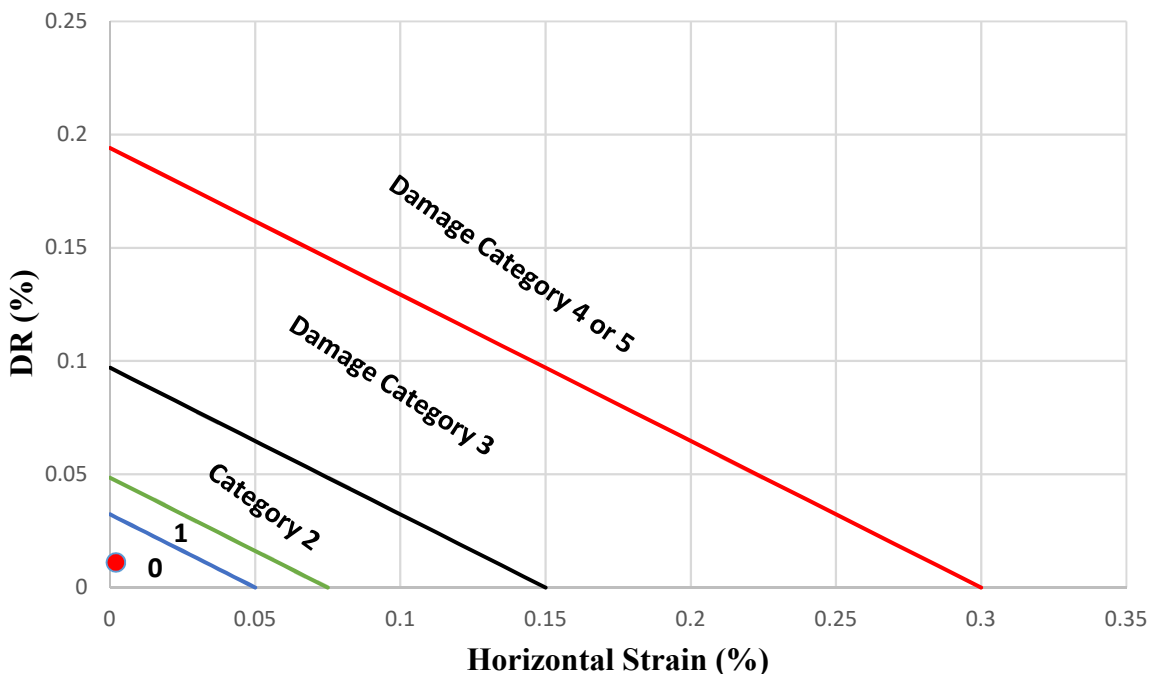


Figure 3.52. Evaluation of the damage along the foundation of the building.

The plotted point in red falls within the area of damage category zero. Hence negligible damage occurs (Table 1.2) with hairline cracks of width $0 - 0.1 \text{ mm}$. This confirms the effectiveness of the design approach (soil structure interaction) in reducing tunnelling induced building effects.

3.7.2. Building damage with soil structure interaction not considered (greenfield case)

The potential building damage is also assessed using the damage criterion proposed by Burland & Wroth, (1974). Here, the results of the greenfield section are considered.

The sagging and hogging sections of the greenfield section of the building are illustrated in Figure 3.53 below. The deflection ratios in both sagging DR_{Sag}^{GF} and hogging DR_{Hog}^{GF} are also computed graphically from Figure 3.53.

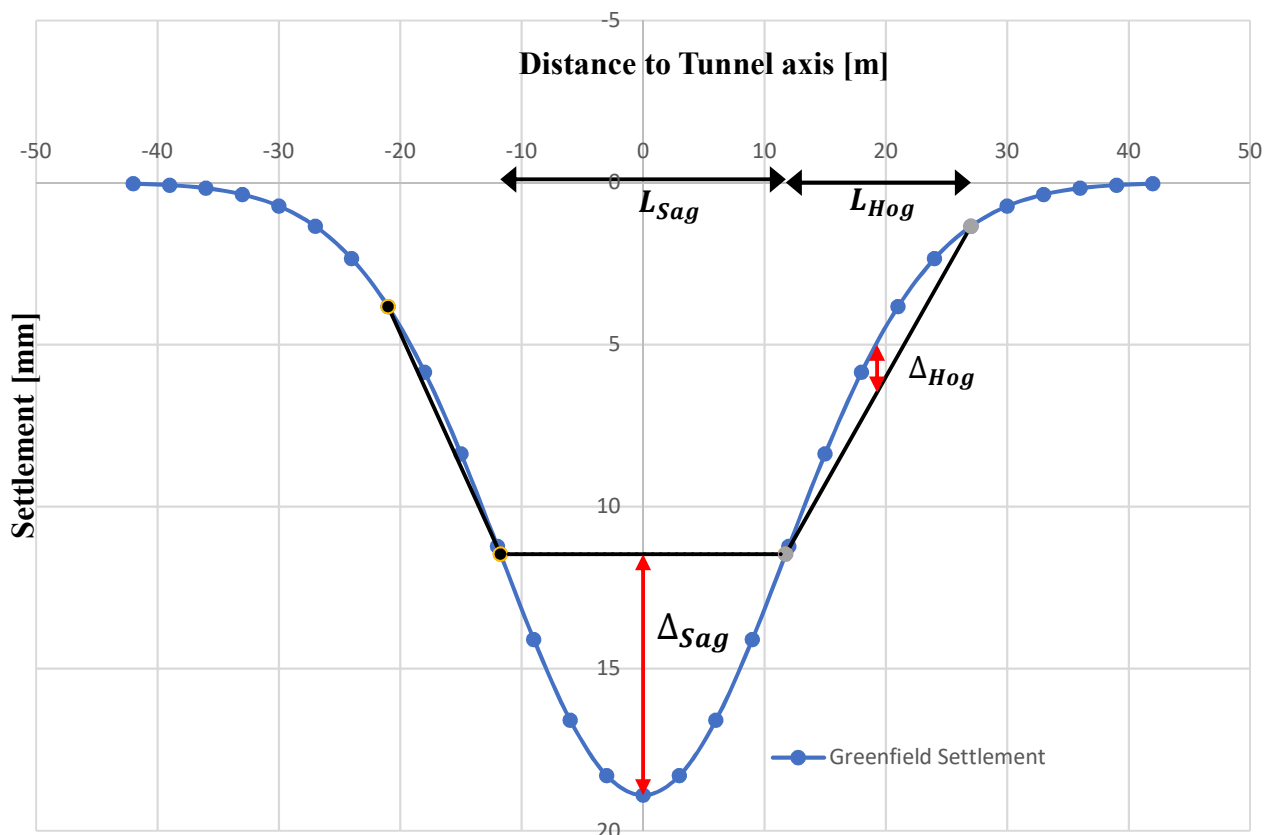


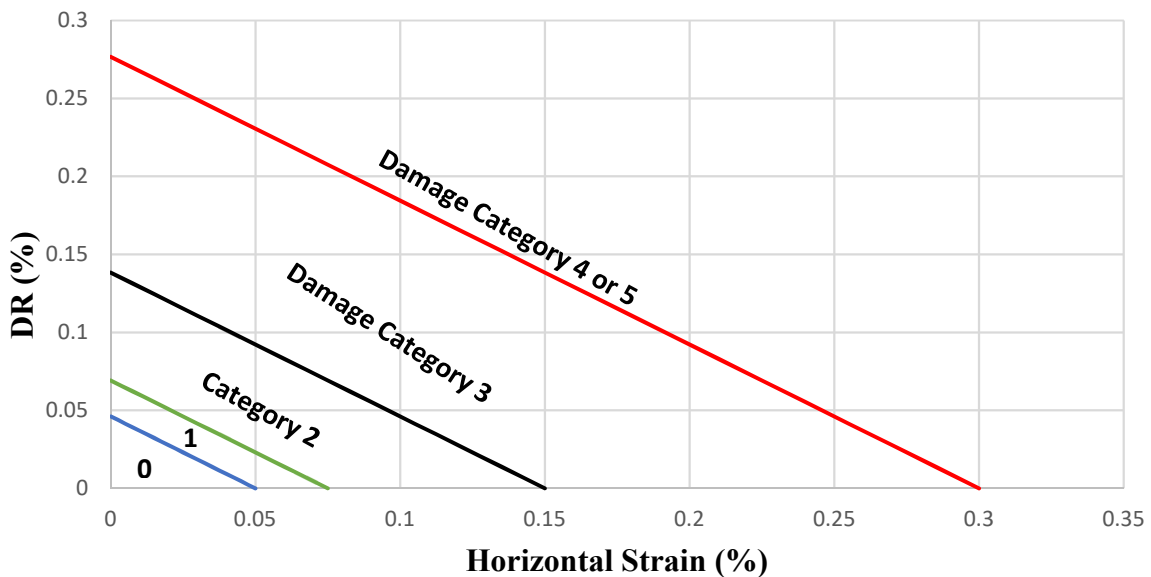
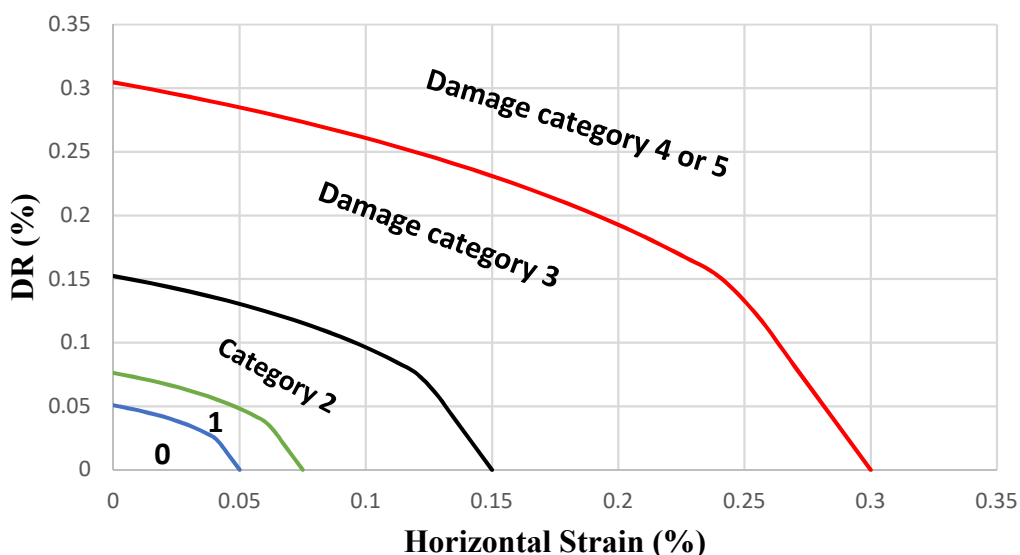
Figure 3.53. Determination of the greenfield deflection ratios.

The computed values of the deformation parameters (relative deflection and deflection ratio) of the greenfield section in sagging and hogging are displayed in Table 3.7.

Table 3.7. Deformation parameters of the greenfield section.

Deformation mode	Building length L (m)	Relative deflection Δ (mm)	Deflection ratio $DR^{GF}(\%)$
Sagging	23.5	7.44	0.032
Hogging	15.25	1.46	0.0096

The damage interaction diagram plotted for the sagging and hogging zones are shown in Figure 3.54 and Figure 3.55 respectively.

**Figure 3.54.** Greenfield damage interaction diagram for sagging ($L/H=0.75$).**Figure 3.55.** Greenfield damage interaction diagram for hogging ($L/H=0.49$).

Using Figure 3.22, the maximum compressive horizontal strain ε_{hc} in the sagging zone is 0.1132%, while the maximum tensile horizontal strain ε_{ht} in the hogging zone is 0.0392%. The point of $DR - \varepsilon_h$ pair for sagging and hogging is plotted in the corresponding damage interaction diagram to determine the category of damage as shown in Figure 3.56 and Figure 3.57 respectively. This point is indicated in red colour.

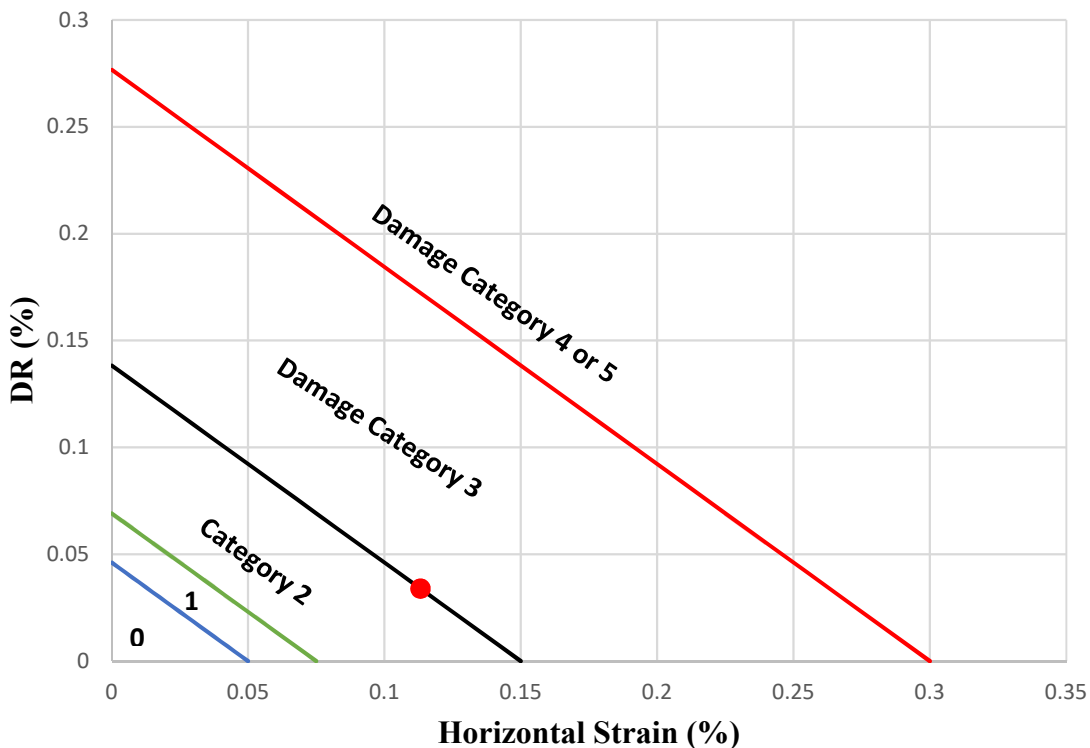


Figure 3.56. Evaluation of building damage in the sagging zone.

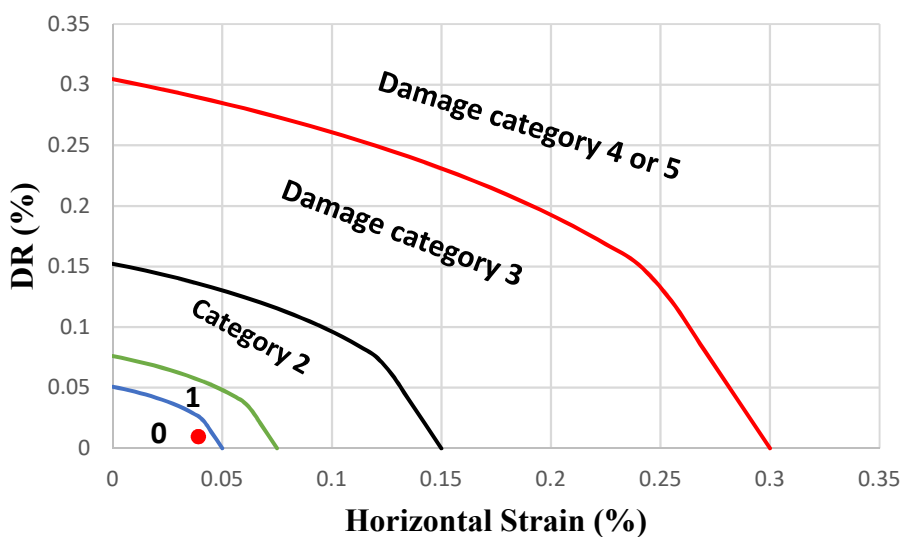


Figure 3.57. Evaluation of building damage in the hogging zone.

A damage category level of category 3 is obtained for the building section in the sagging zone as indicated by the red dot in Figure 3.56 above. For the hogging zone, a lower damage category of 0 is determined (Figure 3.57). Therefore, sagging is determined to be the most critical in this case and the potential level of building damage is Category 3 with a moderate degree of severity. The approximate crack width is 5 – 15 mm (Table 1.1). Damage category 3 affects serviceability of the structure.

When comparing the potential level of damage obtained when the building is assumed to follow the greenfield settlement profile to that for which soil structure interaction is considered, it is seen that a highly conservative result is obtained when the interaction is not considered (Damage category 3). Incorporating the soil structure interaction reduces the damage level from category 3 to category 0 eliminating the need for protective measures thereby reducing cost.

Conclusion.

This chapter's main aim was to present, interpret and discuss the results of soil tunnel structure interaction with the Steinhaldenfeld tunnel as a case study. The analysis results based on the three-dimensional finite element simulation of the tunnel in greenfield and coupled soil structure situations using MIDAS GTS NX were presented in this chapter. The greenfield settlements showed good agreements with field measurements and empirical predictions indicating that the numerical model adopted can be used to simulate complex interaction problems. A study of the tunnelling induced settlements on the foundation of the building showed that the building stiffness interacts with the ground to reduce building's deformation. The variation of axial forces and moments in columns and beams as the tunnel face advances was also evaluated. Based on the results of coupled soil structure interaction, the potential damage to the structure due to the tunnel excavation was also determined using the damage criterion proposed by Burland & Wroth, (1974).

GENERAL CONCLUSION AND RECOMMENDATIONS.

The general objective of this thesis was to study the tunneling superstructure interaction using the Finite Element Method with the Steinhaldenfeld tunnel as a reference case study. The tunnel is a single tube horse shoe shaped tunnel that was constructed using the New Astrain Tunnelling Method (NATM) with an advance length of 1.2m. In order to examine the effects of the sequential tunnel excavation, a 3D finite element model was developed in MIDAS GTS NX software considering the main features of the excavation in greenfield conditions. The soil mechanical behaviour was described by Hardening Soil (small strain stiffness) constitutive model. The tunnel was excavated full face employing the step by step installation procedure of conventional tunnelling. The developed Finite Element Model is then validated against field measurements and available numerical model. The verified 3D model is then used to carry out the fully coupled soil tunnel structure interaction analysis. The structural elements were described using the linear elastic constitutive model. The induced deformations (settlements and horizontal strains) and excess internal forces (axial forces and bending moments) because of the tunnel advancement are investigated. In addition, the expected level of damage on the reinforced concrete building is also evaluated. It is possible to draw the following conclusions from the results:

The greenfield settlement profile obtained from the finite element model used showed good agreement with field measurements and other numerical results.

The transverse settlement profile of the greenfield case can be approximated correctly by a Gaussian fitted curve with a specific trough width parameter and maximum settlements occurring at the point directly above the tunnel axis line.

In the greenfield case, as the tunnel face advances, the longitudinal settlements increase to an almost steady state condition.

In the presence of the building, with advancing the tunnel face towards the location of the building, differences between the greenfield and the coupled soil structure cases increase, with the maximum differences occurring almost near the centre of mass.

The stiffness of the building interacts with the ground to reduce the deformations (settlements and strains) induced on the building by the tunnel excavation process.

Tunnel advancement causes increasing vertical displacement and redistribution of internal forces (axial forces and bending moments) in the beams and columns. The vertical

displacements of the columns as the ground settles cause stresses to be released and the magnitude of the axial force on the columns either increases or reduces. Columns closer to the tunnel centreline experience greater settlement. For example, the analysis results showed that with tunnel advancement, the maximum settlement of column 4 located at distance of 4 m from tunnel axis is 1.22 cm, while column 5 located at a distance of 8 m from the tunnel axis settled to 1.17 cm. Due to the high settlement of columns closer to the tunnel axis, their axial forces decrease, whereas the columns which settled less (columns farther from the tunnel axis) showed an increase in axial force due to redistribution of forces by the beams. For example, the axial force of column 4 reduced by 55 KN and that of column 5 increased by 42 KN. The unsymmetrical nature of the building can also distort this trend as was seen in the case of column 1 whose axial force was decreasing after a few construction stages and then started increasing as the tunnel passed under the structure.

The risk of damage of the building when soil structure interaction is considered was found to be category zero (negligible) implying that only hairline cracks occur. Not considering the interaction problem leads to an over conservative level of damage, that is, category 3 (moderate) damage.

The research provided in this thesis has made it possible to understand the factors that control the tunnel-soil-building interaction problem better. When modelling the interaction problem, there were certain limitations:

- In the modelling, a frictionless interface between the building and foundation preventing relative horizontal movement between the soil and building was adopted. Results that differ from those shown here would surely be obtained by considering a friction interface. The basic conclusions, however, would not differ from those presented here.
- In the finite element modelling of the building, all the columns had the same dimensions in all the building storeys. Considering different dimensions might lead to more general conclusions on the variation of internal forces.
- In the coupled soil structure interaction analysis, the geometry adopted assumed the tunnel axis line passed directly under the centre of mass of the structure which led to the building deforming largely in sagging. Highly eccentric buildings can provide a better representation of how hogging develops when step by step tunnel excavation is simulated.

REFERENCES

- Addenbrooke, T. I. (1996). Numerical analysis of tunnelling in stiff clay, 12-28.
- Addenbrooke, T. I., Potts, D. M., & Puzrin, A. M. (1997). The influence of pre-failure soil stiffness on the numerical analysis of tunnel construction. *Geotechnique*, 47(3), 693–712.
- Attewell, P B; Yeates, J; Selby, A. R. (1986). Soil movements induced by tunnelling and their effects on pipelines and structures, 410–415.
- Attewell, P. B., & Farmer, I. W. (1974). Ground Deformations Resulting from Shield Tunnelling in London Clay. *Canadian Geotechnical Journal*, 11(3), 380–395.
<https://doi.org/10.1139/t74-039>
- Attewell, P. B., & Woodman, J. P. (1982). Predicting the Dynamics of Ground Settlement and Its Derivatives Caused By Tunnelling in Soil. *Ground Engineering*, 15(8).
[https://doi.org/10.1016/0148-9062\(83\)90142-0](https://doi.org/10.1016/0148-9062(83)90142-0)
- Bell, F. G., Cripps, J. C., Culshaw, M. G., & Lovell, M. A. (1988). A review of ground movements due to civil and mining engineering operations. *Geological Society Engineering Geology Special Publication*, 3–32.
<https://doi.org/10.1144/GSL.ENG.1988.005.01.01>
- Benz, T. (2007). Small-Strain Stiffness of Soils and its Numerical Consequences. In University of Stuttgart, 193.
- Bhavikatti, S. S. (2005). Finite Element Analysis (Issue 3). New Age International Limited, New Delhi.
<http://www.embase.com/search/results?subaction=viewrecord&from=export&id=L351657491>
[http://dx.doi.org/10.1016/S14744422\(08\)701030%0A](http://dx.doi.org/10.1016/S14744422(08)701030%0A)
https://books.google.com/books?id=rwC_tUX-GxYC&pgis=1
- Boscardin, B. M. D., & Cording, E. J. (1989). Building response to excavation-induced settlement. 115(1), 1–21.
- Burland, J. (n.d.). The assessment of the risk of damage to buildings due to tunnelling and excavations – AN HISTORICAL PERSPECTIVE Routine guides on limiting distortion and settlement, 1-30.
- Burland, J. B. (1995). Assessment of risk of damage to buildings due to tunnelling and excavation. Invited Special Lecture.1st International Conference on Earthquake

Geotechnical Engineering.

- Burland, J. B. (2008). The assessment of the risk of damage to buildings due to tunnelling and excavation. *Jornada Techica 16-12-08, Movimientos de Edificios Inducidos Por Excavaciones: Criterios de Dano y Gestión Del Riesgo*. Escola Technica Superior d' Enginyers de Camins, Canals I Ports de Barcelona, Universitat Politecnica de Catalunya.
- Burland, J. B., Broms, B. B., & de Mello, V. F. B. (1977). Behaviour of foundations and structures. *9th Int. Conf. Soil Mech. and Found*, 495–546.
- Burland, J. B., & Wroth, C. P. (1974). Settlement of buildings and associated damage. Conference ‘Settlement of Structures,’ 611–654.
- Conditioning, T., Oggeri, C., & Vinai, R. (2022). Soil Conditioning and Ground Monitoring for Shield Tunnelling soil conditioning and ground monitoring. *18(2012)*, 2–14.
- Cording, E. J., & Hansmire, W. H. (1975). methods for geotechnical observations and instrumentation in tunneling national sciencr . e foundation. *1(december)*, 80-101.
- Eberhardt, E. (2014). EOSC 547 : Tunnelling & Underground Design Tunnelling Methods. 1–15.<http://www.eos.ubc.ca/courses/eosc547/lecture-material>
- EN1991-1-1. (2002). Eurocode 1: Actions on structures - Part 1-1: General actions -Densities, selfweight, imposed loads for buildings (Vol. 1, Issue 2005).
- Farrell, R. P., & Mair, R. J. (2012). The response of buildings to tunnelling: A case study. International Society for Soil Mechanics and Geotechnical Engineering (ISSMGE), 877–885. https://doi.org/10.1007/978-3-319-73568-9_174
- Franza, A. (2016). Tunnelling and its effects on piles and piled structures. Ph.D. Thesis, University of Nottingham, November, 256.
- Franzius, J. N. (2003). Behaviour of buildings due to tunnel induced subsidence A thesis submitted to the University of London for the degree of Doctor of Philosophy and for the Diploma of the Imperial College of Science , Technology and Medicine By Jan Niklas Franzius Departmen. October, 360.
- Franzius, J. N., Potts, D. M., & Burland, J. B. (2006). The response of surface structures to tunnel construction. *Proceedings of the Institution of Civil Engineers: Geotechnical Engineering*, *159(1)*, 3–17. <https://doi.org/10.1680/geng.2006.159.1.3>
- Frischmann, W. W., Hellings, J. E., Gittoes, S., & Snowden. (1994). Protection of the Mansion

- House against damage caused by ground movements due to the Docklands Light Railway Extension. Instn. Civ. Engrs. Geotech. Engineering.
- González-Nicieza, C., Álvarez-Vigil, A. E., Menéndez-Díaz, A., & González-Palacio, C. (2008). Influence of the depth and shape of a tunnel in the application of the convergence-confinement method. *Tunnelling and Underground Space Technology*, 23(1), 25–37. <https://doi.org/10.1016/j.tust.2006.12.001>
- Haji, T. K. (2017). Evaluating the Effects of Tunnel Construction on Buildings. November, 25–66.
- Hajjar, M., Nemati Hayati, A., Ahmadi, M. M., & Sadrnejad, S. A. (2015). Longitudinal Settlement Profile in Shallow Tunnels in Drained Conditions. *International Journal of Geomechanics*, 15(6), 04014097. [https://doi.org/10.1061/\(asce\)gm.1943-5622.0000447](https://doi.org/10.1061/(asce)gm.1943-5622.0000447)
- KATZENBACH, R., & Breth, H. (1981). NONLINEAR 3-D ANALYSIS FOR NATM IN FRANKFURT CLAY. Proceedings of the International Conference on Soil Mechanics and Foundation Engineering, 10th., 315–318.
- Leca, E. (2019). Settlements Induced by Tunnelling in Soft Ground, 19.
- Leca, E., New, B., & Reporter, G. (2007). Settlements induced by tunneling in Soft Ground. *Tunnelling and Underground Space Technology*, 22(2), 119–149. <https://doi.org/10.1016/j.tust.2006.11.001>
- Lunardi, P., Cassani, G., Gatti, M., Bellocchio, A., & Zenti, C. L. (2019). Life safety applied in full face excavation. *Tunnels and Underground Cities: Engineering and Innovation Meet Archaeology, Architecture and Art- Proceedings of the WTC 2019 ITA-AITES World Tunnel Congress*, 4921–4931. <https://doi.org/10.1201/9780429424441-522>
- M. Potts, D., & Zdravkovic, L. (1999). Finite Element Analysis in Geotechnical Engineering: Volume One - Theory. In *Finite Element Analysis in Geotechnical Engineering: Volume One - Theory*. <https://doi.org/10.1680/feagiet.27534>
- Mair, R. ., Taylor, R. N., & Burland, J. . (1996). Prediction of ground movements and assessment of risk of building damage due to bored tunnelling. *International Society for Soil Mechanics and Geotechnical Engineering*, 713–718.
- Mair, R. J., & Taylor, R. N. (1993). Subsurface settlement profiles above tunnels in clays. *Geotechnique*, 43(2), 315–320. <https://doi.org/10.1680/geot.1995.45.2.361>

- Mair, R. J., & Taylor, R. N. (1997). Bored tunnelling in the urban environment, 2353-2354.
- Marshall, A. M. (2009). Tunnelling in sand and its effect on pipelines and piles. In Engineering Department: Vol. PhD Thesis (Issue March), 9-26.
- Masosonore, M. C., & Boumediene, T. H. (2019). urban areas on ground surface People ' s Democratic Republic of Algeria Ministry of Higher Education and Scientific Research University of Sciences and Technology Houari Boumediene Faculty of Civil Engineering Domain Sciences and Technology Department of . January, 1. <https://doi.org/10.13140/RG.2.2.18794.57285>
- MIDAS GTS NX User Manual. (2019).
- Moayed, R. Z., Izadi, E., & Mirsepahi, M. (2011). Effect of accounting rockbolts in the numerical analysis on the surface settlements of Steinhaldenfeld tunnel. October, 1–6.
- Möller, S. (2006a). Tunnel induced settlements and structural forces in linings. Universitat Stuttgart, 3-107.
- Möller, S., Rogowski, & Lehmann, T. L. (2004). Dreidimensionale FiniteElement-Berechnung der Setzungsmulde am Beispiel des Steinhaldenfeldtunnels in Stuttgart,, Kolloquium Bauen in Boden Und Fels. Tagungsband4. Ostfildern.
- Mouratidis, A. (2008). The “Cut-and-Cover” and “Cover-and-Cut” techniques in highway engineering. Electronic Journal of Geotechnical Engineering, 13 F.
- New, B. M., & O'Reilly, M. P. (1991). Tunnelling induced ground movements: predicting their magnitude and effects. 4th International Conference on Ground Movements and Structures, 671–697.
- O'REILLY, M. P., & NEW, B. M. (1982a). Settlements above tunnels in the United Kingdom - their magnitude and prediction.pdf (173–181).
- Panet, M., & Guenot, A. (1983). Analysis of convergence behind the face of a tunnel : Tunnelling 82, proceedings of the 3rd international symposium, Brighton. International Journal of Rock Mechanics and Mining Sciences & Geomechanics.
- Pattekar, K. (2020). shape of tunnels. kpstructures. <https://www.kpstructures.in/2020/11/shape-of-tunnels-tunnel-engineering.html>
- Peck, R. B. (1969). Deep excavation and tunnelling in soft ground. Proceed. 7th International Conference on Soil Mechanics and Foundation Engineering, 225–290.

- Rankin, W. J. (1988). Ground movements resulting from urban tunnelling: Predictions and effects. Geological Society Engineering Geology Special Publication, 5(5), 79–92.
<https://doi.org/10.1144/GSL.ENG.1988.005.01.06>
- Rowe, R. K., Lo, K. Y., & Kack, G. J. (1983). Method of Estimating Surface Settlement Above Tunnels Constructed in Soft Ground. Canadian Geotechnical Journal, 20(1), 11–22.
<https://doi.org/10.1139/t83-002>
- Sun, J. (2022). Basic finite element mesh explained. <https://www.midasoft.com/bridge-library/basic-finite-element-mesh-explained>
- Swoboda, G. (1979). Finite element analysis of the new austrian tunnelling method (NATM). 3rd International Conference on Numerical Methods in Geomechanics, Aachen, 581–586.
- Timoshenko, S. (1955). Strength of materials. In part 1: Elementary theory and problems. (3rd ed.).
- Truty, A. (2008). Hardening Soil model with small strain stiffness (Course Notes). Presentation (Course Notes), 0–5.
- Wilton, J. L. (1996). Cut-and-cover tunnel structures. Tunnel Engineering Handbook, 320–359.
https://doi.org/10.1007/978-1-4613-0449-4_17
- Yang Ng, H. (2021). STRUCTURE magazine | avoiding sinkholes during mechanized closed-face tunneling. <https://www.structuremag.org/?p=19276>
- Zhang, X., & Zhan, Z. (2021). Evaluation of risk of building damage due to deep excavations via numerical modelling. Advances in Civil Engineering, 2021.
<https://doi.org/10.1155/2021/6646094>

APPENDIX.

APPENDIX A: Characteristic values of imposed loads(EN1991-1-1, 2002)

Table A.0.1. Imposed loads on floors, balconies and stairs in buildings.

Categories of loaded areas	q_k [kN/m ²]	ϱ_k [kN]
Category A		
- Floors	1,5 to <u>2,0</u>	<u>2,0</u> to 3,0
- Stairs	<u>2,0</u> to 4,0	<u>2,0</u> to 4,0
- Balconies	<u>2,5</u> to 4,0	<u>2,0</u> to 3,0
Category B	2,0 to <u>3,0</u>	1,5 to <u>4,5</u>
Category C		
- C1	2,0 to <u>3,0</u>	3,0 to <u>4,0</u>
- C2	3,0 to <u>4,0</u>	2,5 to 7,0 (<u>4,0</u>)
- C3	3,0 to <u>5,0</u>	<u>4,0</u> to 7,0
- C4	4,5 to <u>5,0</u>	3,5 to <u>7,0</u>
- C5	<u>5,0</u> to 7,5	3,5 to <u>4,5</u>
category D		
- D1	<u>4,0</u> to 5,0	3,5 to 7,0 (<u>4,0</u>)
- D2	4,0 to <u>5,0</u>	3,5 to <u>7,0</u>

APPENDIX B: SOIL CONSTITUTIVE MODEL.

APPENDIX B.1: The Hardening Soil Model

The original HS model was developed by Schanz(1998) and Schanz et al(1999) on the basis of the Double Hardening model by Vermeer(1978). Thus, the HS model also comprises ideas by Konner (1936), Duncan & Chang (1970), and Rowe (1962). Standard lab tests, such as triaxial and oedometer tests provide the model's basic characteristics. In drained triaxial primary loading, the experimentally observed relation between axial strain and deviatoric stress in soils can be well approximated by a hyperbolic function. Kondner & Zelasko (1963) described the hyperbolic stress strain relation for drained triaxial loading as follows:

$$\varepsilon_1 = \varepsilon_{50} \frac{q}{q_a - q} \quad \text{with} \quad q_a = \frac{2 \sin \varphi}{1 - \sin \varphi} (\sigma_3 + c \cot \varphi) \quad \text{and} \quad \varepsilon_{50} = \frac{q_{50}}{E_{50}} = \frac{q_a}{2E_{50}} \quad | \text{(B. 1)}$$

Where q_a is an asymptotic stress, q is the deviatoric stress and ε_1 is the axial strain.

Assuming that under primary loading the behaviour is clearly nonlinear and hyperbolic up to a Mohr-Coulomb failure stress q_f , Figure depicts the usual curve of a drained triaxial test with constant lateral pressure σ_3 .

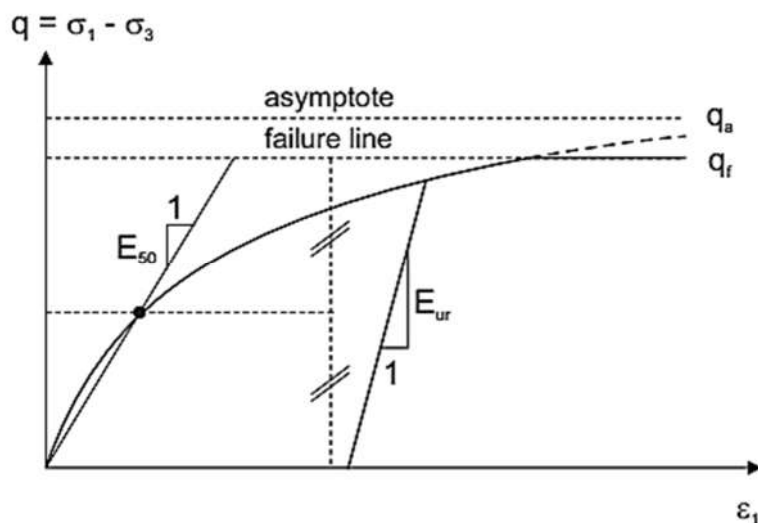


Figure B. 1. Drained triaxial test: hyperbolic relationship for primary loading between deviatoric stress and axial strain.

the hyperbolic part of the curve can be defined using a single secant modulus as additional input parameter. In the HS Model this is the stress dependent modulus E_{50} , as used in equation B.1 which is defined as:

$$E_{50} = E_{50}^{ref} \cdot \left(\frac{c' \cdot \cot \varphi' + \sigma'_3}{c' \cdot \cot \varphi' + p^{ref}} \right)^m \quad (\text{B. 2})$$

where E_{50}^{ref} is a reference stiffness modulus, corresponding to the reference confining pressure p^{ref} . The exponent m indicates the amount of stress dependency.

E_{ur} is a real elasticity modulus, as opposed to E_{50} , which indicates the magnitude of both the elastic and plastic strains. It establishes the ground behaviour while unloading and reloading in conjunction with a Poisson's ratio ν_{ur} : the indices ur denote unloading/reloading. Unloading modulus E_{ur} is depending on stress level, similar to the average primary loading modulus E_{50} . For the HS Model it is given as:

$$E_{ur} = E_{ur}^{ref} \cdot \left(\frac{c' \cdot \cot \varphi' + \sigma'_3}{c' \cdot \cot \varphi' + p^{ref}} \right)^m \quad (\text{B. 3})$$

where E_{ur}^{ref} is the reference Young's modulus

In the hardening soil model, a distinction is made between two types of hardening, namely shear hardening and compression hardening. For the shear hardening law a yield function f^s is introduced, which is a function of the triaxial loading stiffness E_{50} and for the compression hardening a yield function f^c is formulated, being governed by the oedometer loading stiffness E_{oed} .

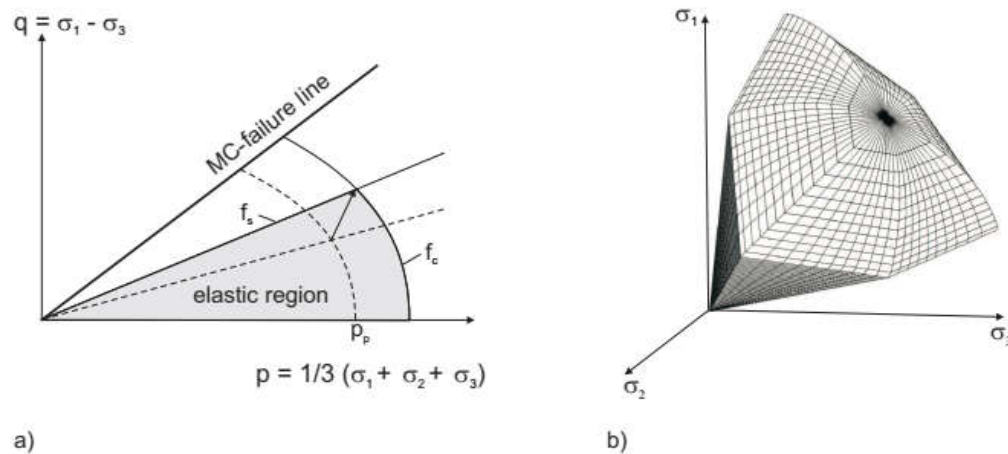


Figure B. 2. Yield surface of the HS Model for $c = 0$: a) successive yield loci for shear hardening and compression hardening in p-q-space b) total yield contour in principal stress space.

As shown in Figure B.2a for unloading-reloading elastic soil behaviour is assumed, adopting Hook's law with Young's modulus E_{ur} .

The yield function f^s adopted in the HS-Model has the formulation:

$$f^s = \bar{f} - \gamma^p, \quad (\text{B. 4})$$

Where,

$$\bar{f} = \frac{1}{E_{50}^{ref}} \cdot \left(\frac{c' \cdot \cot \varphi' + \sigma'_3}{c' \cdot \cot \varphi' + p^{ref}} \right)^m \cdot \frac{q}{1 - q/q_a} - \frac{2q}{E_{ur}^{ref}} \cdot \left(\frac{c' \cdot \cot \varphi' + \sigma'_3}{c' \cdot \cot \varphi' + p^{ref}} \right)^m \quad (\text{B. 5})$$

is a function of stress and the hardening parameter k^s (function of plastic strains)

$$\kappa^s = \gamma^p = \varepsilon_1^p - \varepsilon_2^p - \varepsilon_3^p = 2 \cdot \varepsilon_1^p - \varepsilon_v^p \approx 2 \cdot \varepsilon_1^p \quad (\text{B. 6})$$

HS-Model adopts non-associated plasticity to determine the rates of plastic strain with the plastic potential

$$g^s = (3 - \sin \psi_m) \cdot q - 6 \cdot \sin \psi_m \cdot p, \quad (\text{B. 7})$$

With $p = 1/3 \cdot (\sigma_1 + \sigma_2 + \sigma_3)$.

The so-called stress-dilatancy equation of ROWE (1962) is used to compute the mobilised angle of dilatancy ψ_m

$$\sin \psi_m = \frac{\sin \varphi_m - \sin \varphi_{cv}}{1 - \sin \varphi_m \cdot \sin \varphi_{cv}} \quad (\text{B. 8})$$

Where the mobilized friction angle is expressed as:

$$\sin \varphi_m = \frac{\sigma_1 - \sigma_3}{\sigma_1 + \sigma_3 + 2 \cdot c \cdot \tan \varphi} \quad (\text{B. 9})$$

and the constant-volume angle φ_{cv} is given by:

$$\sin \varphi_{cv} = \frac{\sin \varphi - \sin \psi}{1 - \sin \varphi \cdot \sin \psi}. \quad (\text{B. 10})$$

For the yield function f^c , the compression hardening is formulated means of cap-type yield surfaces, which makes the model both suitable for hard soils as well as very soft clays. The cap-type yield function has the formulation:

$$f^c = \frac{q^2}{M^2} + (p + c \cdot \tan \varphi)^2 - (p_p + c \cdot \tan \varphi)^2 \quad (\text{B. 11})$$

With

$$M = \frac{6 \cdot \sin \varphi}{3 - \sin \varphi}. \quad (\text{B. 12})$$

The position and shape of the cap in stress space is governed by the isotropic pre-consolidation pressure p_p indicated in Figure B.2. The hardening law in Equation B.13 below,

$$\kappa^c = \varepsilon_v^{pc} = \frac{\beta}{1-m} \left(\frac{p_p}{p^{ref}} \right)^{1-m} \quad (\text{B. 13})$$

formulates the relation between the plastic volumetric cap-strain ε_v^{pc} and the preconsolidation stress p_p . p^{ref} is an isotropic reference pressure. The cap parameter β is not used as a direct input parameter. Instead the odometer stiffness E_{oed} is used as an input parameter which is linked to β . Figure B.3 shows the typical characteristic curve of an oedometer test. In the HS Model the oedometer stiffness obeys a stress dependency according to the formula in Equation B.14:

$$E_{oed} = E_{oed}^{ref} \cdot \left(\frac{c' \cdot \cot \varphi' + \sigma'_1}{c' \cdot \cot \varphi' + p^{ref}} \right)^m \quad (\text{B. 14})$$

where E_{oed}^{ref} is the reference Oedometer Modulus for the axial reference pressure p^{ref} .

In the special case of $m = 1$, one obtains a linear stress-dependency as usual for a clay. In addition to the moduli E_{50} and E_{ur} , the oedometer modulus E_{oed} is also an input modulus for the HS Model. Together with the parameters m , ν_{ur} , c' , φ' and the dilatancy angle ψ , there are a total of eight input parameters. To determine the rates of plastic volumetric strains associated plasticity, $g^c = f^c$ is adopted.

APPENDIX B.2: The HS-Small Model.

The HS-Small Model constitutes an extension of the HS-Model. All model features described for the HS Model also hold true for the HS-Small Model. In addition to the HS Model, the HS-Small Model incorporates a formulation of the small strain stiffness. A significantly greater elasticity modulus E_0 is produced by small unloading-reloading stress-strain paths as shown in Figure B.3. In actuality, the highest soil stiffness is seen at extremely low strain levels. This effect is referred to as small strain stiffness.

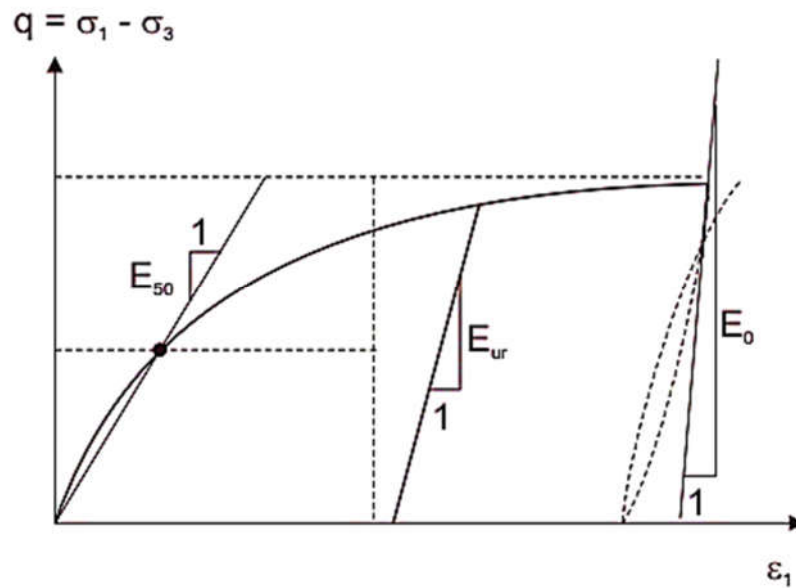


Figure B. 3. HS-Small Model: extension of the HS Model incorporating small strain stiffness

The formulation of small strain stiffness in the HS-Small Model assumes that the decay of small strain stiffness is primarily related to either break up of bonding forces between soil particles or frictional forces exceeding their elastic limit.

As shown in Figure B.4, for strains higher than 10^{-5} a rapid drop of small strain ground stiffness is measured, considering shear modulus G .

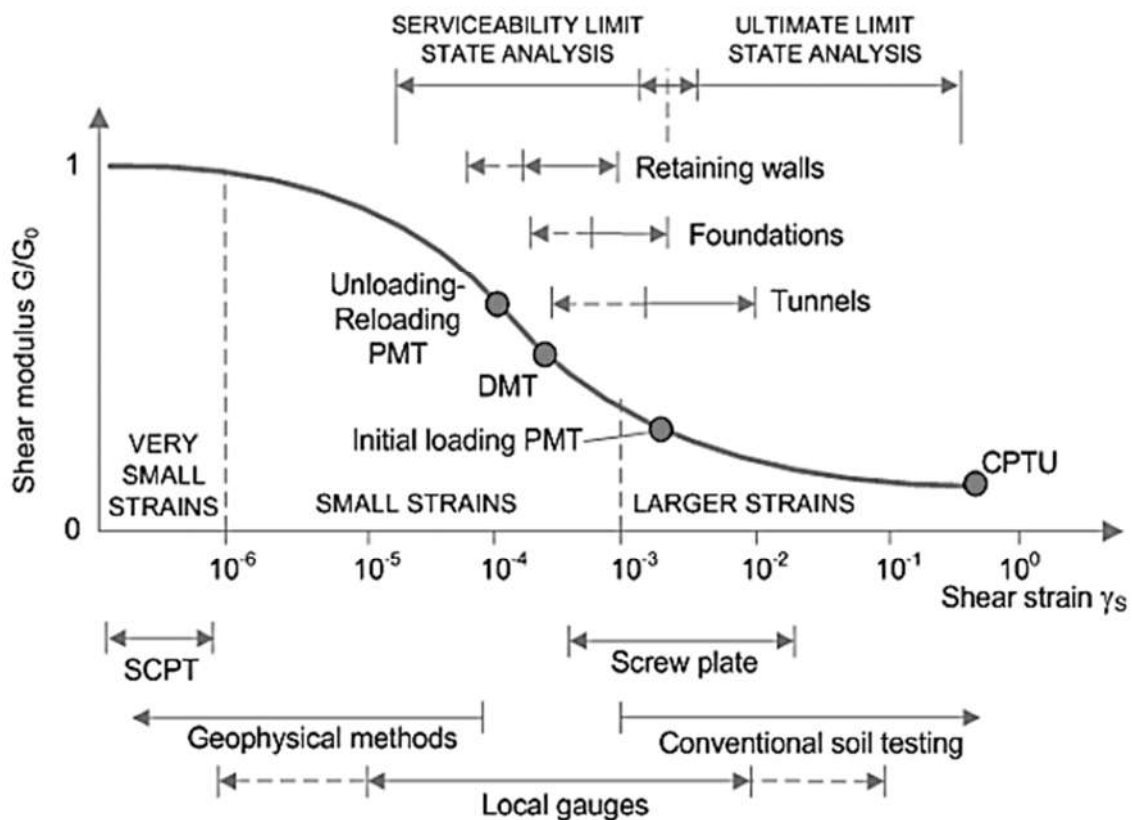


Figure B. 4. Characteristic stiffness-strain curve for soils(Trutty, 2008).

To incorporate small strain stiffness effects into the HS Model a relatively simple expression for the small strain stiffness decay of the shear modulus is adopted as shown in Equation B.15:

$$G = \frac{G_0}{1 + 0.43 \cdot \frac{\gamma}{\gamma_{0.7}}} \quad (\text{B. 15})$$

where, G is the actual shear modulus at shear strain γ , G_0 is the initial shear modulus and $\gamma_{0.7}$ is the shear strain at which the initial shear modulus has reduced to $0.7 \cdot G_0$, as shown in Figure B.4. For general states of stress, the shear strain is expressed using the strain invariant γ by Equation B.16.

$$\gamma = \frac{1}{\sqrt{2}} \cdot \sqrt{(\varepsilon_1 - \varepsilon_2)^2 + (\varepsilon_2 - \varepsilon_3)^2 + (\varepsilon_3 - \varepsilon_1)^2} \quad (\text{B. 16})$$

According to the HS Model's formulation of stiffnesses and OHDE's (1951) theories, the initial shear modulus G_0 is pressure dependant according to Equation B.17;

$$G_0 = G_0^{ref} \cdot \left(\frac{c' \cdot \cot \varphi' + \sigma'_3}{c' \cdot \cot \varphi' + p_{ref}} \right)^m \quad (\text{B. 17})$$

The magnitude of G_0^{ref} is strongly correlated to the porosity of the soil. A typical correlation being used is $G_0^{ref} = 450 \cdot \sqrt{P_{ref}}$ by BIAREZ and HICHER (1994). According to the formulation of the HS Model, stiffness degradation due to plastic straining is modelled by involving material hardening. Therefore, before reaching plastic material behaviour, the formulation of the small strain stiffness curve is cut off at the unloading-reloading shear modulus G_{ur} , defined by Equation B.18.

$$G_{ur} = \frac{E_{ur}}{2 \cdot (1 + \nu_{ur})} \quad (\text{B. 18})$$

In the equation above G_{ur} is the shear modulus in complete deviatoric unloading as illustrated in Figure B.3.

In addition to the input parameters introduced for the HS Model, there are a set of two additional input parameters for the HS-Small Model: the elastic small strain shear modulus G_0^{ref} at reference pressure P_{ref} and the threshold value $\gamma_{0.7}$ in primary loading. For more explanations of the Hardening soil model and hardening soil with small strains model, the reader is referred to (Benz, 2007).

APPENDIX C: Construction Stages for Greenfield Analysis.

Set Type	Set Name Prefix	I.S.	S1	S2	S3	S4	S5	S6	S7	S8	S9	S10	S11	S12	S13	S14	S15	S16	S17	S18	S19	S20	S21	S22	S23	S24	S25	S26	S:				
Boundary Set	BC Set-																																
Load Set	Dead load																																
Mesh set	FILL	A: -																															
Mesh set	LIMESTONE	A: -																															
Load Set	Live load																																
Mesh set	LOWER KEUPER MARL	A: -																															
Boundary Set	RAFT																																
Mesh set	RAFT SOIL	A: -																															
Mesh set	RC STRUCTURE-																																
Mesh set	ROCKBOLT-					A: 1	A: 2	A: 3	A: 4	A: 5	A: 6	A: 7	A: 8	A: 9	A: 10	A: 11	A: 12	A: 13	A: 14	A: 15	A: 16	A: 17	A: 18	A: 19	A: 20	A: 21	A: 22	A: 23	A: 24	A: 25	A: -		
Load Set	Self weight	A: -																															
Mesh set	SHOTCRETE-					A: 1	A: 2	A: 3	A: 4	A: 5	A: 6	A: 7	A: 8	A: 9	A: 10	A: 11	A: 12	A: 13	A: 14	A: 15	A: 16	A: 17	A: 18	A: 19	A: 20	A: 21	A: 22	A: 23	A: 24	A: 25	A: -		
Boundary Set	SHOTCRETE-								A: 1	A: 2	A: 3	A: 4	A: 5	A: 6	A: 7	A: 8	A: 9	A: 10	A: 11	A: 12	A: 13	A: 14	A: 15	A: 16	A: 17	A: 18	A: 19	A: 20	A: 21	A: 22	A: 23	A: 24	A: -
Boundary Set	SOIL CONSTRAINT	A: -																															
Mesh set	TUNNEL-	A: 1to75	R: 1	R: 2	R: 3	R: 4	R: 5	R: 6	R: 7	R: 8	R: 9	R: 10	R: 11	R: 12	R: 13	R: 14	R: 15	R: 16	R: 17	R: 18	R: 19	R: 20	R: 21	R: 22	R: 23	R: 24	R: 25	R: 26	R: -				
Mesh set	UPPER KEUPER MARL	A: -																															

S29	S30	S31	S32	S33	S34	S35	S36	S37	S38	S39	S40	S41	S42	S43	S44	S45	S46	S47	S48	S49	S50	S51	S52	S53	S54	S55	S56	S57	S58	S59	S60	S61	S62	S63	S64	S65	S66	S67
A: 2	A: 2	A: 3	A: 31	A: 3	A: 33	A: 3	A: 35	A: 36	A: 3	A: 38	A: 39	A: 40	A: 41	A: 42	A: 43	A: 44	A: 45	A: 46	A: 47	A: 48	A: 49	A: 50	A: 51	A: 52	A: 53	A: 54	A: 5	A: 56	A: 57	A: 58	A: 59	A: 6	A: 61	A: 62	A: 63	A: 64	A: 65	A: 66
A: 2	A: 2	A: 3	A: 31	A: 3	A: 33	A: 3	A: 35	A: 36	A: 3	A: 38	A: 39	A: 40	A: 41	A: 42	A: 43	A: 44	A: 45	A: 46	A: 47	A: 48	A: 49	A: 50	A: 51	A: 52	A: 53	A: 54	A: 5	A: 56	A: 57	A: 58	A: 59	A: 6	A: 61	A: 62	A: 63	A: 64	A: 65	A: 66
A: 2	A: 2	A: 2	A: 28	A: 2	A: 30	A: 3	A: 32	A: 33	A: 3	A: 35	A: 36	A: 37	A: 38	A: 39	A: 40	A: 41	A: 42	A: 43	A: 44	A: 45	A: 46	A: 47	A: 48	A: 49	A: 50	A: 51	A: 5	A: 53	A: 54	A: 55	A: 56	A: 5	A: 58	A: 59	A: 60	A: 61	A: 62	A: 63
R: 29	R: 30	R: 3	R: 32	R: 3	R: 34	R: 35	R: 36	R: 37	R: 38	R: 39	R: 40	R: 41	R: 42	R: 43	R: 44	R: 45	R: 46	R: 47	R: 48	R: 49	R: 50	R: 51	R: 52	R: 53	R: 54	R: 55	R: 5	R: 57	R: 58	R: 59	R: 60	R: 61	R: 62	R: 63	R: 64	R: 65	R: 66	R: 67

	S65	S66	S67	S68	S69	S70	S71	S72	S73	S74	S75	S76	S77	S78	S79	
	A: 64	A: 65	A: 66	A: 67	A: 68	A: 69	A: 70	A: 71	A: 72	A: 73	A: 74	A: 75				
	A: 64	A: 65	A: 66	A: 67	A: 68	A: 69	A: 70	A: 71	A: 72	A: 73	A: 74	A: 75				
	A: 61	A: 62	A: 63	A: 64	A: 65	A: 66	A: 67	A: 68	A: 69	A: 70	A: 71	A: 72	A: 73	A: 74	A: 75	
	R: 65	R: 66	R: 67	R: 68	R: 69	R: 70	R: 71	R: 72	R: 73	R: 74	R: 75					

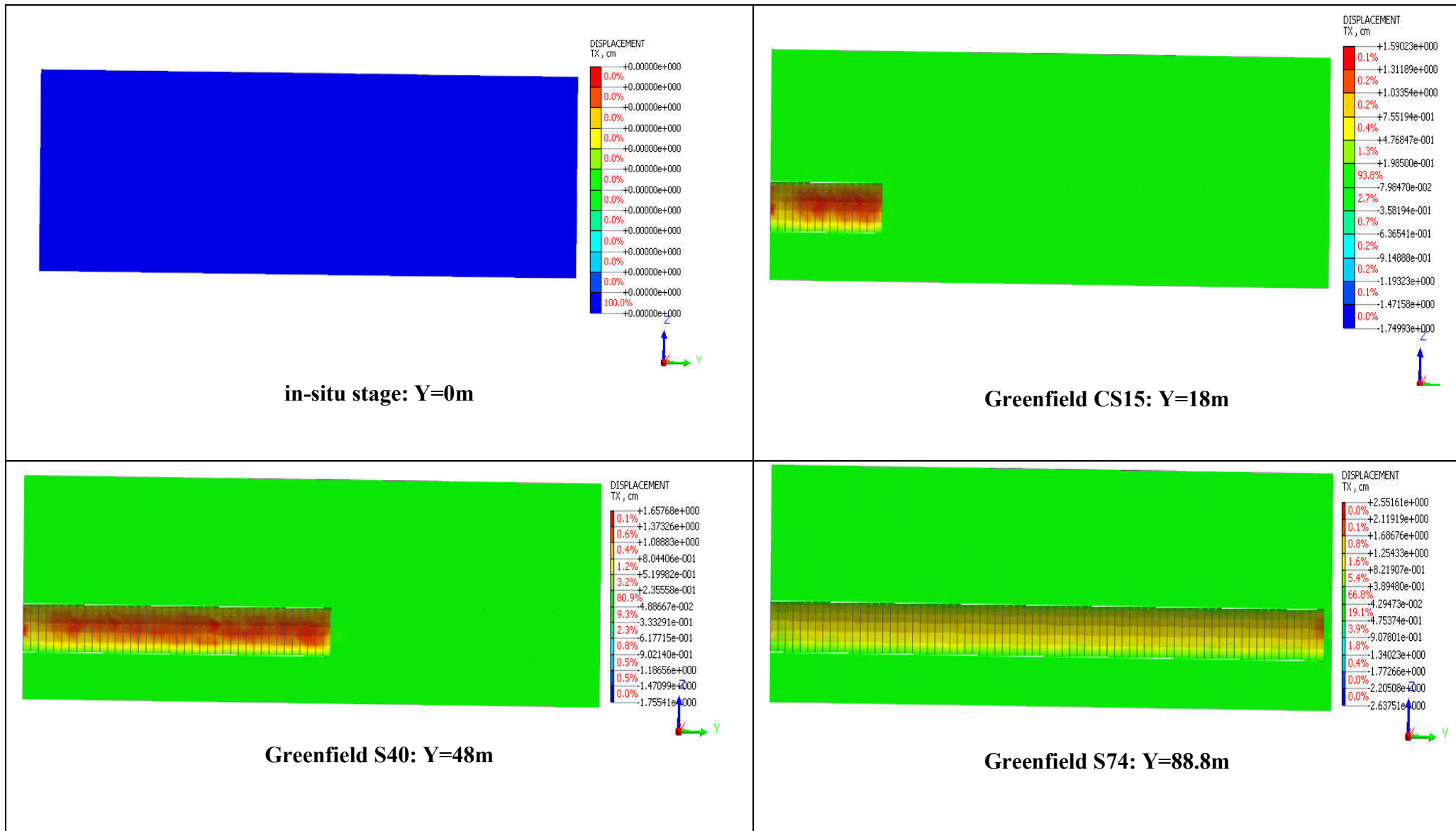
LEGEND:

R: Mesh Set Removal

A: Mesh Set Activation

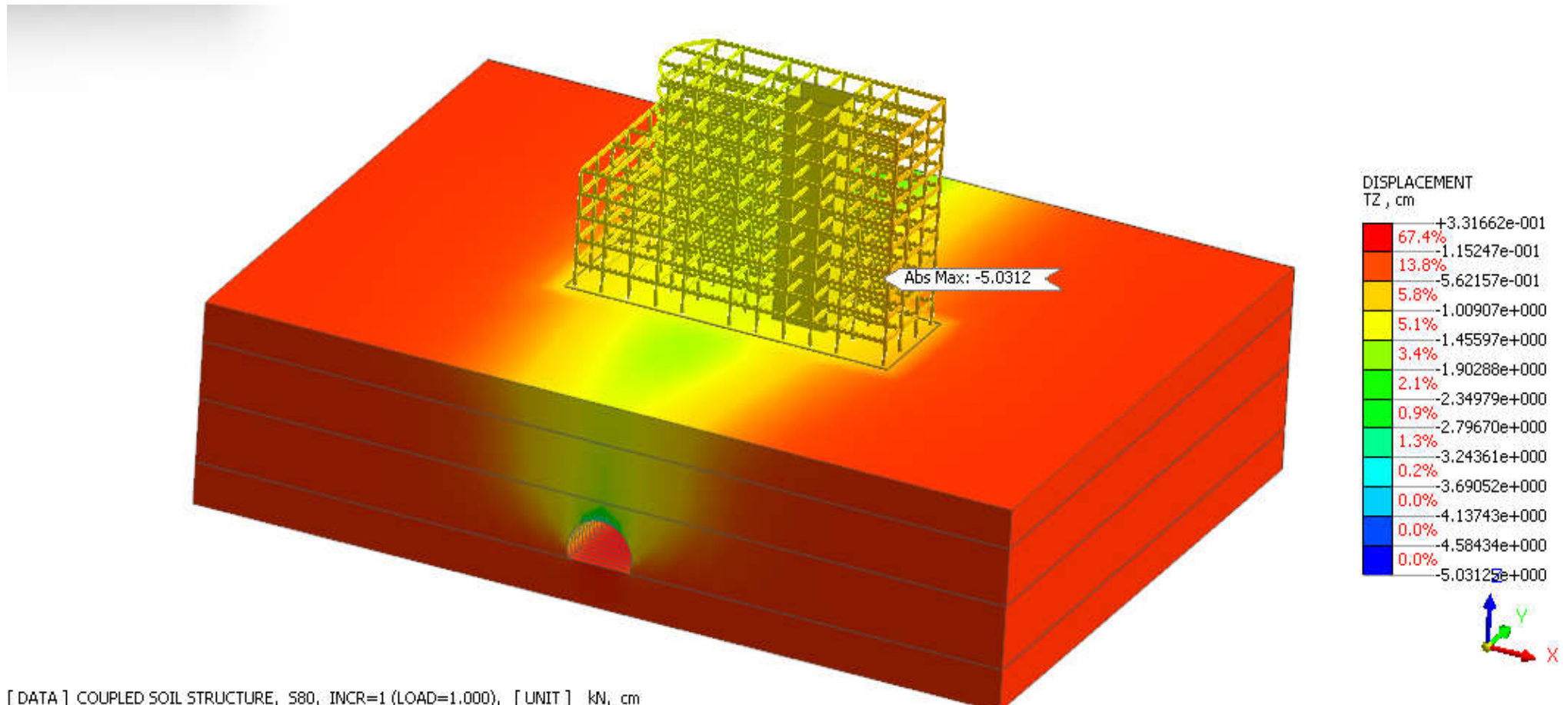
S: Construction Stage

APPENDIX D: Construction Stages for Fully Coupled Soil Structure Interaction Analysis.

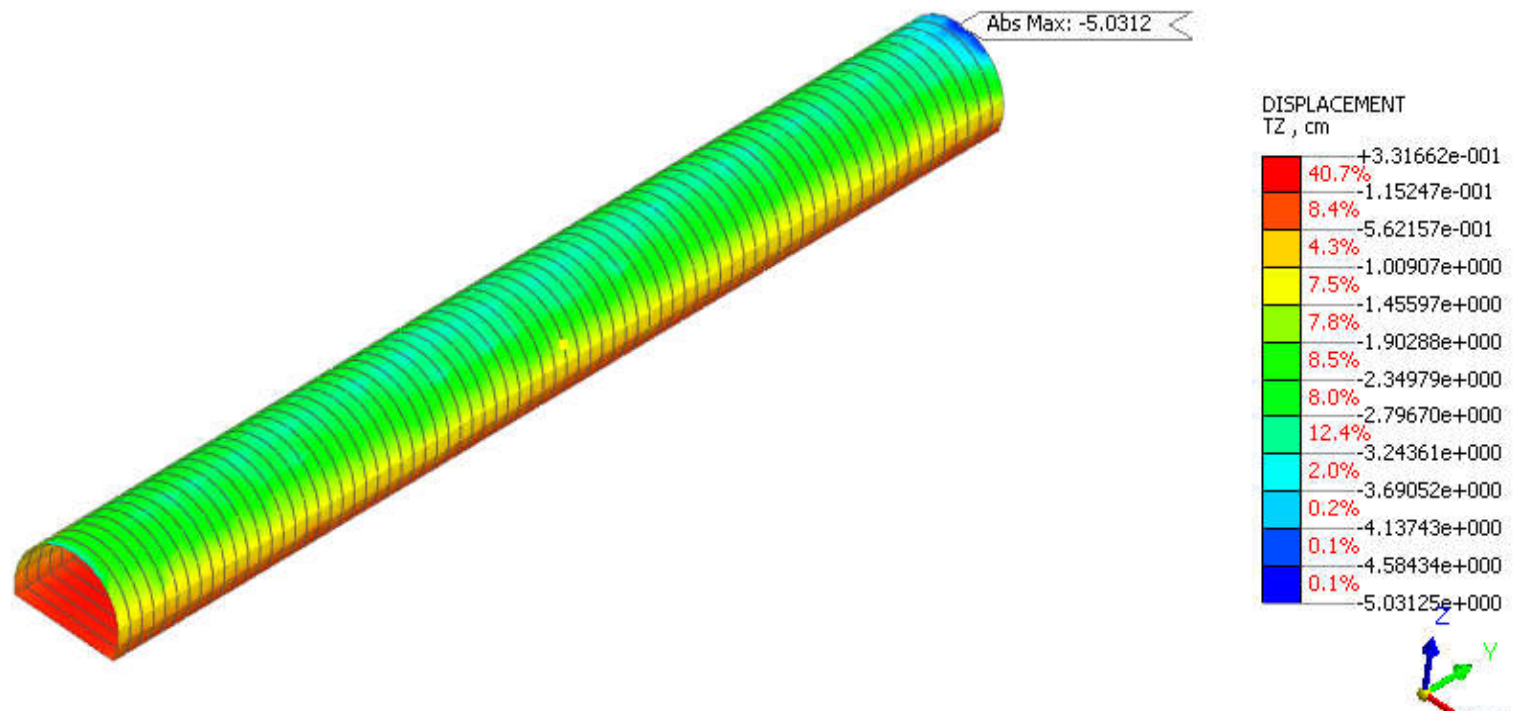


Key:

Y = Position of Tunnel Face.



COUPLED SOIL STRUCTURE INTERACTION: Vertical Displacement; Last Construction Stage



COUPLED SOIL STRUCTURE INTERACTION: Shotcrete Lining Deformation at End of Construction.

